Gas Distribution in Industrial Flotation Machines: A Proposed Measurement Method

Rodrigo Araya Ledezma

Department of Mining and Materials Engineering

McGill University

Montreal, Canada

August 2009

A thesis submitted to the office of graduate studies and research

in partial fulfillment of the requirements for the degree of master

of engineering

Dedicated to my beloved

Katherine

ABSTRACT

Flotation is a multivariable process that can be considered the output of at least four interacting factors: chemical (frother, collector), physical (particle size, percent solids), machine and circuit arrangement. These factors combine with the aim of producing the best conditions for particle collection.

Gas dispersion defines the characteristics of a bubble population generated from a continuous stream of air. Gas Dispersion parameters include superficial gas velocity, gas holdup, bubble size and bubble surface-area flux. Gas distribution defines the spread of the air bubbles throughout the cell volume. It is intuitive that best metallurgical results are likely associated with uniform distribution of gas. The measurement of gas distribution is the focus of this thesis, achieved by simultaneous measurements of gas velocity at several radial distances at a common depth in flotation cells. A distribution deviation index (DDI) is proposed to quantify the distribution.

RÉSUMÉ

La flottation est un processus multivariable que l'on peut considérer le résultat d'au moins quatre facteurs : le produit chimique (moussant, collecteur), les aspects physiques (taille des particules, proportion de solides), l'équipement disponible et le circuit de flottation. Ces facteurs se réunissent pour produire les meilleures conditions pour la séparation de particules.

La dispersion du gaz définit les caractéristiques d'une population de bulles produites dans un courant continu d'air. Parmi les paramètres de dispersion, il y a la vitesse superficielle du gaz, la charge gazeuse, la taille des bulles et le flux de superficie des bulles. La distribution du gaz définit la diffusion des bulles d'air partout dans le volume d'une cellule de flottation. Il est intuitif de croire que les meilleurs résultats métallurgiques seraient associés à une distribution uniforme du gaz. La mesure de la distribution du gaz est le sujet de cette thèse, réalisée par mesures simultanées de vitesse du gaz à plusieurs distances radiales à une profondeur commune dans une cellule de flottation. On propose un indice de déviation de distribution (DDI) pour évaluer quantitativement la distribution du gaz.

ACKNOWLEDGEMENTS

I could never express adequately through written words the thanks I owe to my wife, Katherine. She has had to make many sacrifices during the past two years in order to support me in the work I have been doing. I am certain that had it not been for her encouragement at all the times and continuous support, I would never have accomplished my goals.

I wish to express my sincerest appreciation and gratitude to my supervisor, Prof. James A. Finch for his experience, guidance, ideas, continuous encouragement, valuable technical assistance and discussions provided throughout this work.

I would also like to express my heartfelt thanks to Dr. Cesar O. Gomez for his friendship and for sharing with me part of his incredible knowledge and experience that represent a priceless contribution to the work presented in this thesis.

Thanks must also go to the Jim Finch group members for providing support and encouragement during the smooth and rough rides of my work. Particular thanks to my friends Mayeli Alvarez, Azin Zangooi, Rebecca Payant, Yaneth Aguilar, Paula Proa, Daniela Muñoz, Luis Calzado, Mustafa Tarkan and Patrick Blonde.

I would also like to acknowledge financial support given by the Chair in Mineral Processing co-sponsored by Vale Inco, Teck Cominco, Xstrata Process Support, Agnico-Eagle, Shell Canada, Barrick Gold, SGS Lakefield Research, COREM and Flottec under

the Collaborative Research and Development (CRD) program of NSERC (Natural Sciences and Engineering Research Council of Canada) and through AMIRA International P9O project also under the NSERC-CRD program.

Least but not last, I would like to thank to my parents that have been a source of inspiration all throughout my life and the true reason behind my achievements. They taught me the importance of a strong education and have always encouraged me to pursue my education to the highest levels. For that, I am eternally grateful.

TABLE OF CONTENTS

LIST OF FIGURES

LIST OF TABLES

NOMENCLATURE

A	Cross-sectional area, cm^2
A_{cs}	Machine cross sectional area, cm^2
A_t	Cross-sectional area sampling tube, cm^2
a	Empirical constants orifice
b	Empirical constant orifice
CCC	Critical coalescence concentration, ppm
Db	Bubble size, mm
D_{10}	Arithmetic mean diameter, mm
D_{32}	Sauter mean diameter, mm
d_i	Diameter of the ith bubble, mm
DDI	Distribution deviation index, dimensionless
dP / dt	Slope of pressure vs. time curve, cm/s
ε_g	Gas holdup, %
g	Gravity acceleration, cm/s^2
H_L	Total length of the J_g sensor, cm
H_0	Distance from the top of J_g sensor to the lip of the flotation cell, cm
H_{BD}	Distance between the tips of the “sensor” and the “bubbler” tubes, cm
J_g	Superficial gas velocity, cm/s
J_{gc}	Corrected superficial gas velocity, cm/s
m_s	Mass of solids, g

m_w	Mass of water, g
n	Number of bubbles
P_{atm}	Atmospheric pressure, cmH_2O
P	Pressure, cmH2O
P_L	Pressure at the tip of the J_g sensor, cmH2O
ΔP	Pressure drop between orifice and tube in continuous mode
Q_g	Volumetric flow rate, cm^3/s
$Q_{g(fraction)}$	Fractional volumetric flow rate, dimensionless
q_{in}	Air mass flow rate entering the J_g sensor, g/s
q_{out}	Air mass flow rate leaving the J_g sensor, g/s
R	Radius of the cell, cm
r	Radius of the cell, cm
S_b	Bubble surface area flux, 1/s
t	Time, s
V_a	Volume of air, cm^3
V_T	Total volume (i.e., water, air and solids), cm^3

Greek letters

α	Empiric factor (parabolic profile), dimensionless
β	Empiric factor (parabolic profile), dimensionless
γ	Fraction of solids inside the J_g sensor, dimensionless
η	Solids/liquid ratio, dimensionless
ρ_a	Density of air, g/cm^3

ρ_b	Density of aerated slurry, g/cm^3
ρ_t	Density of aerated slurry inside J_g sensor, g/cm^3
ρ_w	Density of aerated water, g/cm^3
φ	Dimensionless radial distance
λ	Cross-sectional area fraction, dimensionless
Δ_A	Area under the curve $Q_{g(fraction)}$ as a function of area
Δ_R	Area under the curve $Q_{g(fraction)}$ as a function of radius

CHAPTER 1

INTRODUCTION

1.1 - Background

Mineral processing is a branch of engineering which concerns the separation of valuable minerals from waste rock. It consists in several unit operations to obtain the upgraded product or concentrate. The two principal operations are comminution (size reduction) to achieve mineral liberation followed by physical separation. Several separation technologies exist, including flotation, magnetic separation, gravity concentration and electrostatic separation, among others (Wills, 1997).

Flotation is the most widely used technique for concentrating minerals and exploits natural and induced hydrophobicity to collect selected mineral particles on the surface of bubbles (Shergold, 1984). Flotation is conducted in machines (cells) that contain the solid-liquid dispersion (slurry or pulp) with some chemical reagents added to modify particle hydrophobicity (collectors) and promote small bubble formation (frothers) (Claridge, 1989). Due to bubble buoyancy, particles are transported from the pulp to the top of the flotation machine where they accumulate as froth and overflow to form the float product (often the valuable mineral product or concentrate). Flotation cells are arranged in series to form a bank and banks are arranged to form a stage. Flotation is rarely successful in one stage, and multiple stages to form a circuit are used (Wills, 1997).

Flotation is a multivariable process that can be considered the output of at least four interacting factors: chemical (frother, collector), physical (particle size, percent solids), machine and circuit arrangement (Harris, 1976). This thesis focuses on measurements of the "quality" of the air delivered to the machine. For this reason it is necessary to introduce two definitions with respect to air delivery, gas dispersion and gas distribution.

1.2 – Gas dispersion

In the present context, gas dispersion refers to the characteristics of a bubble population generated from a continuous stream of air (Gomez and Finch, 2002). Gas dispersion parameters include superficial gas velocity, gas holdup, bubble size and bubble surface area flux (Finch et al., 2000; Grau and Heikanen, 2003; Schwarz and Alexander, 2006).

1.2.1 – Superficial gas velocity

Gas flow rate is commonly reported as superficial gas velocity, J_g, i.e., the volumetric gas flow rate (Q_g) through an area A. It is usually just referred to as gas (air) velocity, and is given by,

$$J_g = \frac{Q_g}{A} \tag{1. 1}$$

The use of gas velocity instead of volumetric flow rate makes comparison easier between machines of different sizes; for example, the typical range is $0.5 < J_g < 2.5$ cm/s from laboratory to industrial scale (Finch and Dobby, 1990). Gas injection affects

flotation in several ways; for example, higher J_g implies increased probability of collision between bubble and particle and therefore increased recovery. Gas velocity also is associated with entrainment (non selective particle collection due to water recovery). As a result, gas velocity is a key parameter in flotation bank optimization (Cooper et al., 2004).

1.2.2 – Gas holdup

Gas holdup, ε_g, is defined as the volumetric fraction of air contained in the slurry (Nagata, 1975). It has a proportional relationship with J_g over a certain range defining the so-called bubbly flow regime that represents bubbles of fairly uniform size rising at a fairly uniform rate. Figure 1. 1 shows an illustration of the different regimes in flotation columns (Finch and Dobby, 1990) but the same relationship holds in mechanical cells (Dahlke et al., 2005). Gas holdup is governed by bubble rise velocity, for example slow rising small bubbles promote higher gas holdup because they have higher residence time in the slurry than faster rising larger bubbles (Finch and Dobby, 1990).

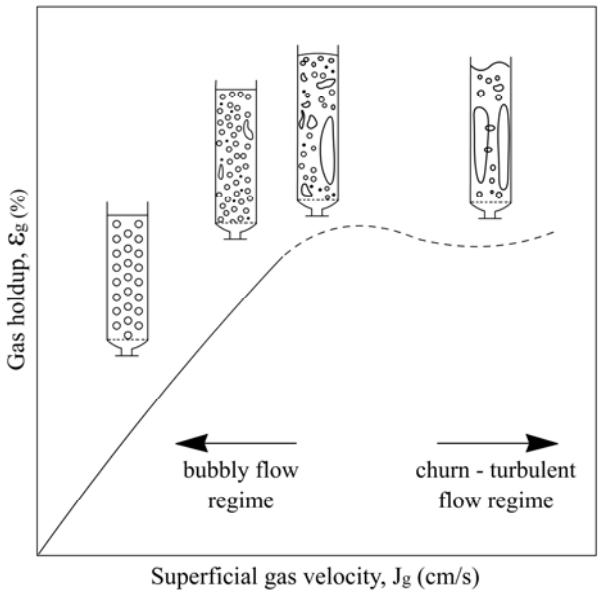

Figure 1. 1 Gas holdup as a function of gas velocity (Finch and Dobby, 1990)

1.2.3 – Bubble size

Bubbles are produced by different mechanisms including cavity action behind turbine blades in mechanical cells (Jameson, 1984; Tatterson, 1991); shear action of a high velocity liquid over a stationary metallic surface (in-line mixers) (Finch, 1995); forcing air through multiple small holes in a porous material; high velocity air jet through a single orifice (Dobby and Finch, 1991); plunging a liquid stream through a liquid surface (Clayton et al., 1991).

Bubbles are responsible for collection and transport of particles from the pulp zone to the concentrate (Wills, 1997). They are produced in a distribution of sizes. In flotation studies there are two common averages used to represent a bubble size distribution, the arithmetic mean diameter (D_{10}) and the Sauter mean diameter (D_{32}) (Grau and Heiskanen, 2005; Nesset et al., 2006; Kracht et al., 2008). The D_{10} is defined as the summation of the bubble diameters divided by the number of bubble diameters,

$$D_{10} = \frac{\sum_{i}^{n} d_i}{n} \tag{1. 2}$$

and the D_{32} is defined as the sum of bubble diameters cubed divided by sum of bubble diameters squared,

$$D_{32} = \frac{\sum_{i}^{n} d_i^3}{\sum_{i}^{n} d_i^2} \tag{1. 3}$$

The D_{32} is commonly considered the more relevant metric in flotation, which is a process driven by bubble surface area.

1.2.4 – Bubble surface area flux

Bubble surface area flux (S_b) is the surface area of bubbles per unit time per unit cross-sectional area (Finch and Dobby, 1990). This term is a calculated parameter (Equation 1.4) that provides a measure of the amount of bubble surface area generated to promote bubble-particle collisions, and is given by,

$$S_b = 6\frac{J_g}{D_{32}} \tag{1.4}$$

The usual unit is s^{-1} (e.g. with J_g in cm/s and D_{32} in cm) and regardless of machine type or size, the range in S_b is typically 10-80 s^{-1} (Gorain et al., 1997). It is sometimes considered the main machine factor (Gorain et al., 1997, Finch et al., 1999, Hernandez et al., 2003).

1.3 – Gas distribution

Gas distribution is the spreading of the air bubbles throughout the cell volume. The ideal distribution is presumably air in the same proportion throughout the cell cross-section. This variable can be determined by taking radial measurements of one of the gas dispersion properties previously introduced: gas velocity, gas holdup or bubble size (Xu et al., 1992; Sanwani et al., 2006). In this work, gas distribution is determined by taking radial measurements of J_g because multiple simultaneous measurements can be made at relatively low cost. A new variable to characterize gas distributions is introduced, the distribution deviation index (DDI).

1.4 – Objectives

The general objective of the thesis is the characterization of gas distribution in industrial flotation machines by measuring (mapping) superficial gas velocity at different distances from the machine center at a constant depth as a function of air flow rate, frother type and concentration. Knowledge of gas distribution is of importance to cell designers and manufacturers and to operations where control over gas distribution may represent a methodology to improve flotation (metallurgical) performance.

1.5 – Structure of the thesis

Chapter 1 - Introduces the thesis presenting a brief general background to flotation, gas dispersion, gas distribution and the objectives of the thesis.

Chapter 2 - Describes different types of flotation machines used in the mineral processing industry.

Chapter 3 - Reviews techniques for measuring superficial gas velocity and discusses theoretical issues regarding the two techniques developed by the Mineral Processing Group at McGill University.

Chapter 4 - Gives theoretical framework concerning gas distribution in flotation cells and derives the distribution deviation index.

Chapter 5 - Presents and discusses experimental data from laboratory and industrial flotation machines with respect to the two techniques for measuring J_g.

Chapter 6 - Presents and discusses experimental data of gas distribution measurements in industrial machines at two concentrators.

Chapter 7 - Draws conclusions from the experiences. Suggestions for future research are also outlined.

CHAPTER 2

FLOTATION MACHINES

2.1 - Introduction

Several designs of flotation machines are currently in wide use (Fallenius, 1976; Degner and Treweek, 1976; Finch and Dobby, 1990; Clayton et al., 1991, Finch, 1995). The machine must suspend solids and generate the bubbles to collect the target mineral (Claridge, 1989). Flotation machines can be divided in two main groups, mechanical cells and pneumatic cells (Wills, 1997). According to Harris (1976), each of these designs promotes particular hydrodynamic characteristics, offering more than one alternative to process minerals of different mineralogy and particle size. This chapter presents a selection of some of the most common flotation machines.

2.2 – Mechanical flotation cells

2.2.1 - General features

A mechanical flotation cell agitates the slurry and disperses the air into small bubbles using a mechanically driven impeller (Claridge, 1989). The design takes into account several variables, including: tank diameter; impeller type, size and geometry; distance between impeller and tank bottom; liquid level; and location of baffles. Impellers are classified depending on the mixing regime, laminar or turbulent; the case of flotation corresponds to the turbulent regime. The distance between the impeller and the tank bottom, the clearance, influences the flow pattern in the cell. Baffles avoid the

rotational movement of slurry created by the impeller. Stator rings are the preferred baffle system (Tatterson, 1991).

When there are no baffles, one characteristic of mechanically stirred tanks is the presence of a vortex (Figure 2. 1) in the central area. This central vortex can aspirate air under certain conditions of impeller rotational speed, impeller submergence, impeller diameter, baffle geometry and liquid height (Nagata, 1975; Tatterson, 1991). This feature makes a sub-clasification of mechanical flotation cells namely, forced air and self-aspirated cells (MacNamara et al., 2007). Forced-air machines receive air from a blower and self-aspirated machines rely on gas entrainment produced by the central vortex.

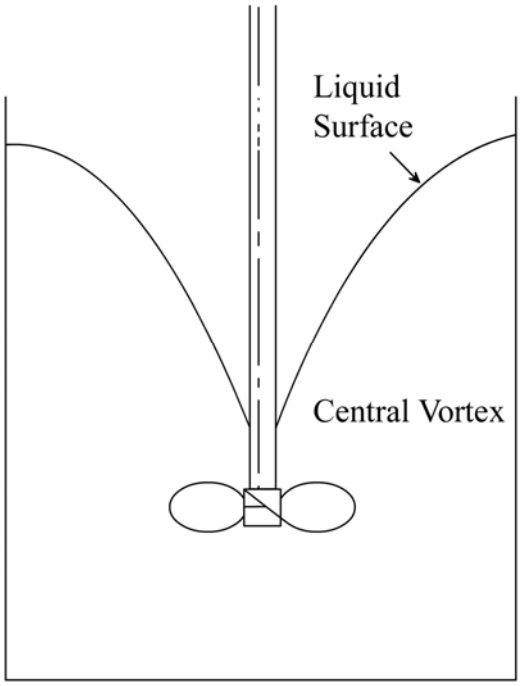

Figure 2. 1 Illustration of a central vortex in a mechanically stirred tank (Tatterson, 1991)

Currently, there are several choices of mechanical cell. Each provides a characteristic hydrodynamic condition. These characteristics should be understood when selecting a machine for a particular application (Harris, 1976). Two common mechanical cells are described below.

2.2.2 – Outotec

Outotec tank cells are forced-air mechanical machines. These cells use a rotor-stator configuration that is available in three choices; FreeFlow, MultiMix and FloatForce® selected depending on the particle size and power requirements. The rotor acts as a pump, drawing pulp upward and discharging outwards (Figure 2. 2). The stator breaks the rotational motion of the pulp, promoting efficient mixing. The air is introduced through a hollow shaft by an external blower and forced into the slurry through specially designed channels at the rotor (Fallenius, 1976; Jonaitis, 1999; Outotec, 2009). Some of these features are seen in Figure 2. 3.

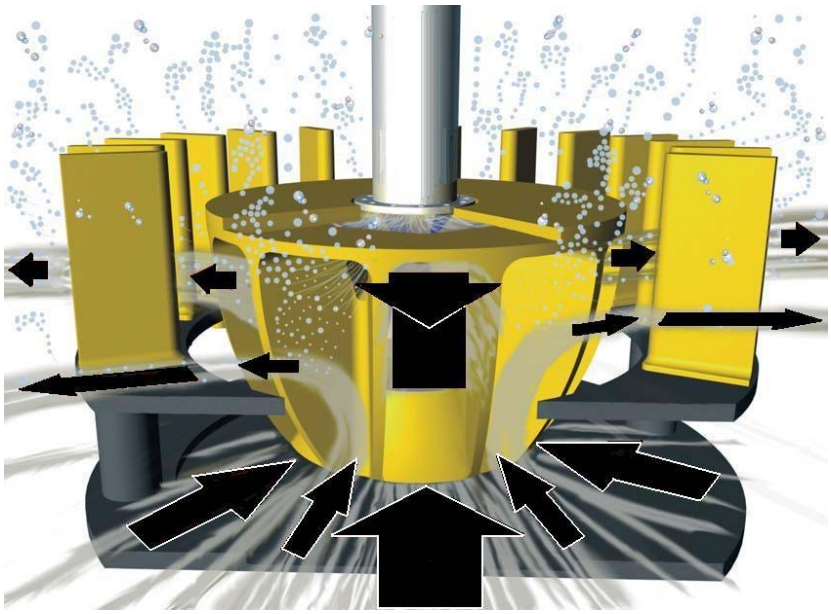

Figure 2. 2 Illustration of radial flow produced by impeller (Outotec, 2009)

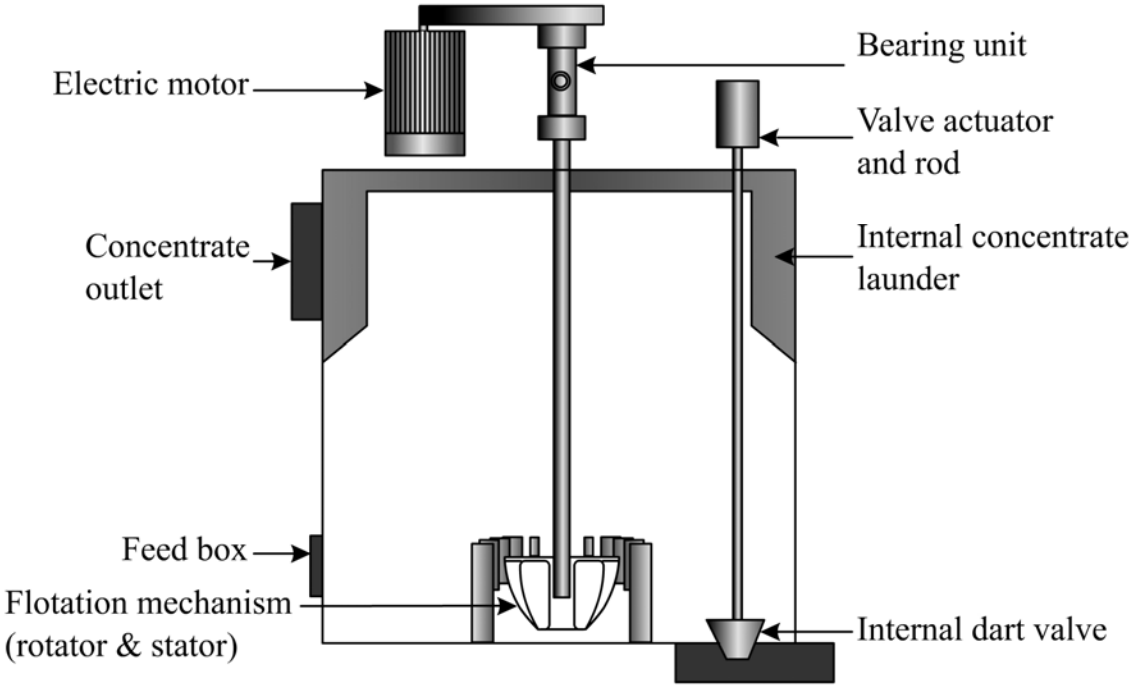

Figure 2. 3 Cut-away diagram of an Outotec tank cell (Outotec, 2009)

In Figure 2. 4, the diagram on the left shows the flow pattern developed in the Outotec cell; the impeller suctions fluid from above and below, and discharges it radially.

2.2.3 – Wemco

Wemco cells are self-aspirated mechanical machines. Impeller design is a rotor-disperser close to the top of the machine (Figure 2. 5). The rotor produces a vortex in the standpipe that creates vacuum that aspirates air into the cell. The rotor motion also induces a pump action that draws pulp through the false bottom as well as through the draft tube. Pulp and air are mixed in the diffuser, promoting particle-bubble collision. Aerated pulp is discharged through the diffuser (Degner and Treweek, 1976; Weber et al., 2007, MacNamara et al., 2007). The rotor is located close to the top of the cell with the idea of decreasing the probability of particle detachment (MacNamara et al., 2007). The

flow pattern is shown in the right hand side diagram of Figure 2. 4; the draft tube draws pulp from the bottom which is discharged outwards at the rotor level, producing a downward circulation of slurry in the tank (Yianatos et al., 2008).

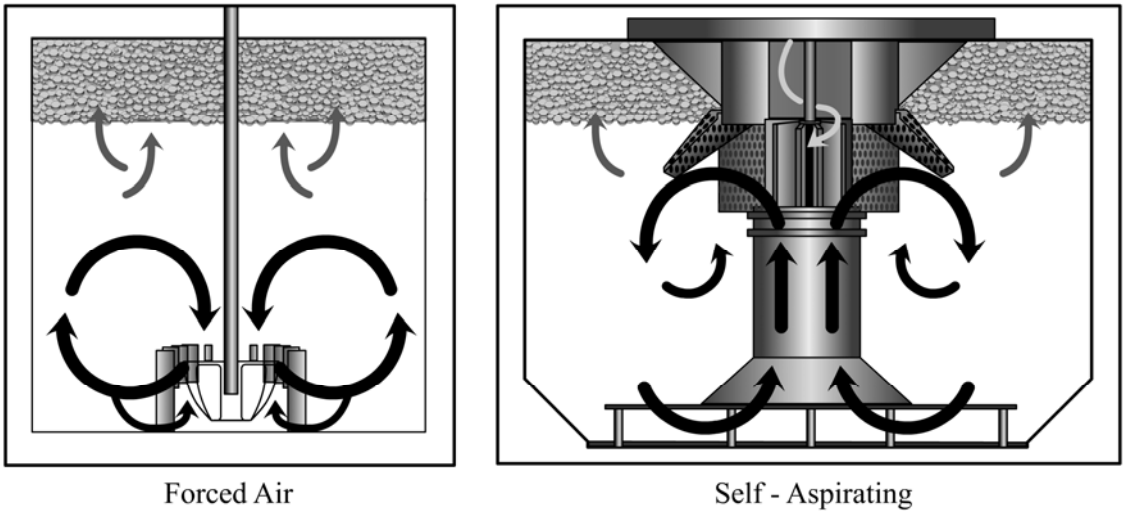

Figure 2. 4 Flow patterns in mechanical flotation cells: left, Outotec Tank cell; right, Wemco (Yianatos et al., 2008)

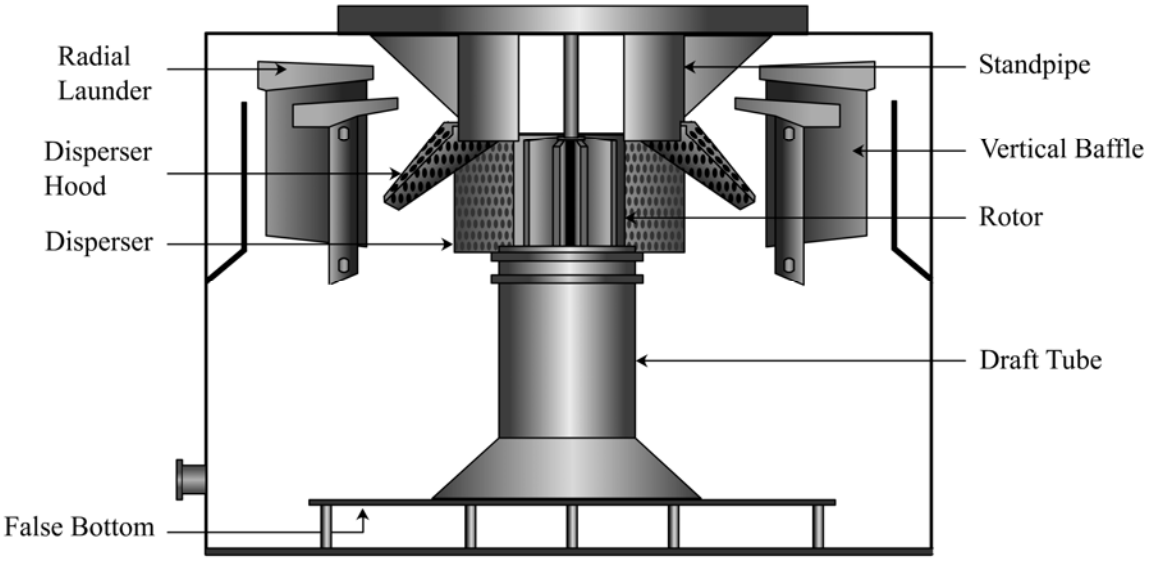

Figure 2. 5 Cut-away diagram of a Wemco cell (Weber, 2007)

2.3 – Pneumatic flotation cells

2.3.1 – General features

Pneumatic machines do not have a mechanically driven impeller to agitate the pulp and disperse the air. Air is introduced either by a jet of slurry (Jameson cell) or by jet-type spargers, porous media or slurry flow over in-line mixers (flotation columns) (Wills, 1997).

2.3.2 – Flotation column (Figure 2. 6)

Air is introduced at the bottom usually with a configuration of spargers, which can be internal or external (Finch, 1995). Pulp agitation is provided by the rising bubble swarm. In selected applications (normally cleaning stages) wash water is added at the top into the froth to help reduce the unselective recovery of fine particles due to water entrainment (Finch and Dobby, 1990; Wyslouzil, 2009). Figure 2. 7 shows a representation of the flow pattern in a flotation column that identifies four regions, namely descending flow, vertical flow, fast bubble flow and central plume (Tzeng, 1993; Lin et al., 1996).

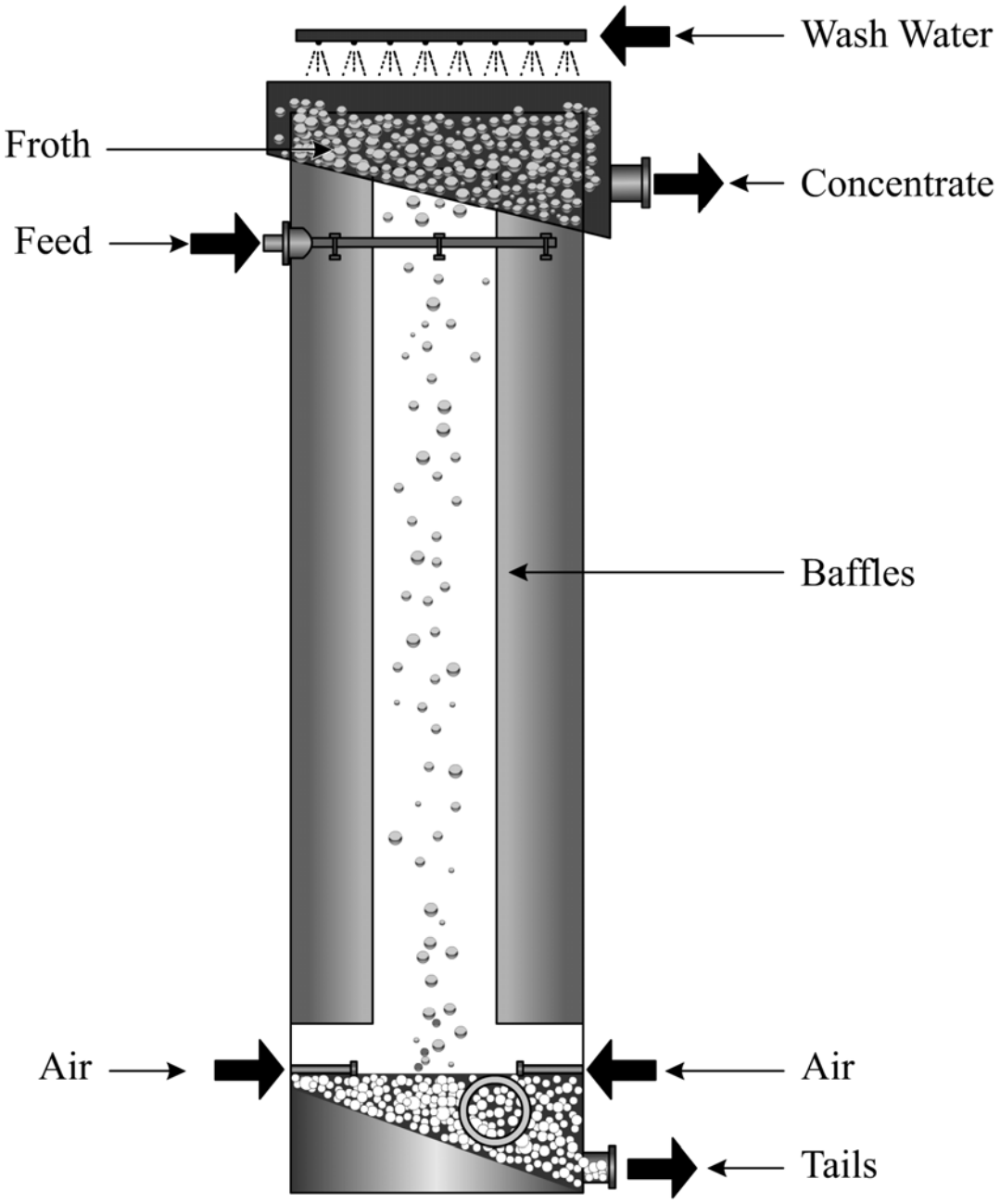

Figure 2. 6 Cut-away diagram of a flotation column (Wyslouzil, 2009)

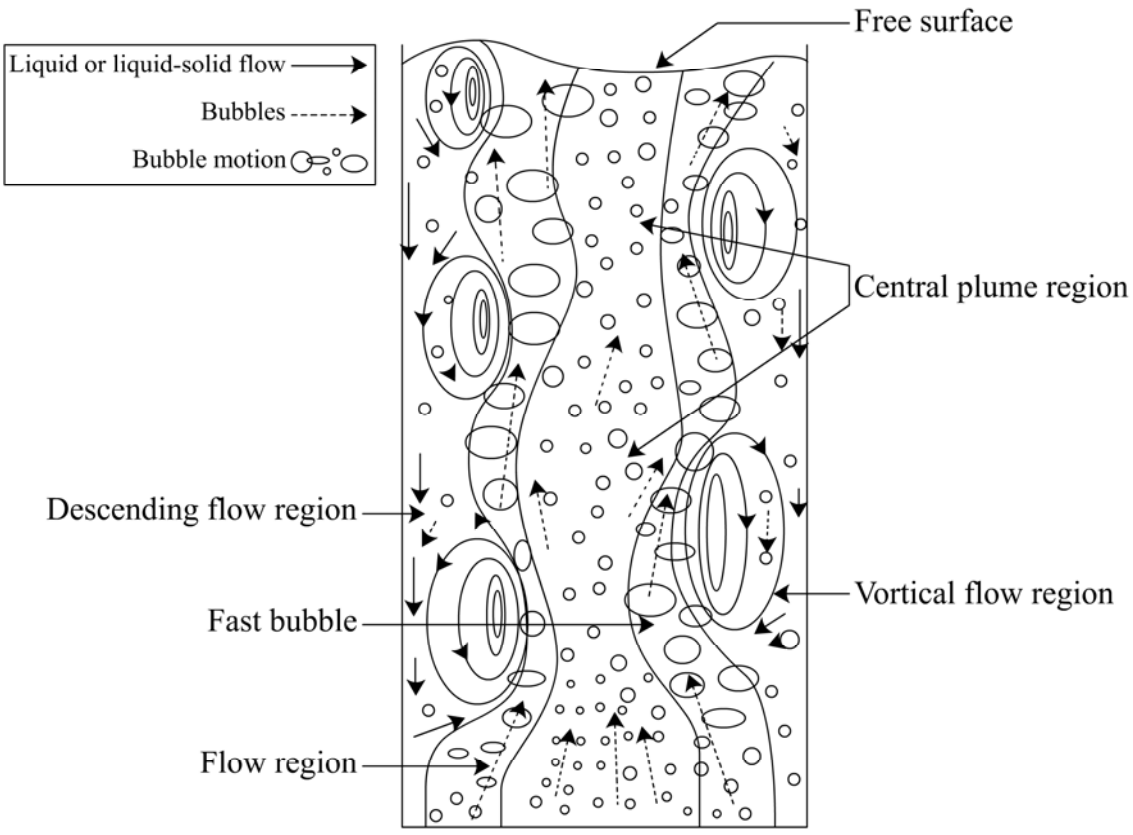

Figure 2. 7 Flow patterns in a flotation column (Tzeng et al., 1993)

2.3.3 – Jameson cell (Figure 2. 8)

Operation consists of introducing a jet of slurry into a tube, the downcomer (Figure 2. 9). The jet causes aspiration of air that is sheared into small bubbles. Mixing of bubbles and particles takes place in the downcomer. Slurry exits the downcomer and enters the pulp zone, where a secondary bubble/particle contact may take place and froth removal occurs (Clayton et al., 1991; Harbort et al., 1994, 2003, Cowburn et al., 2006; Xstrata Technology, 2009). To maintain a constant volumetric feed and thus control air aspiration, a portion of the tailing is recycled. These units have been classified as a reactor separator design, a possible third category of flotation machine (Finch, 1995).

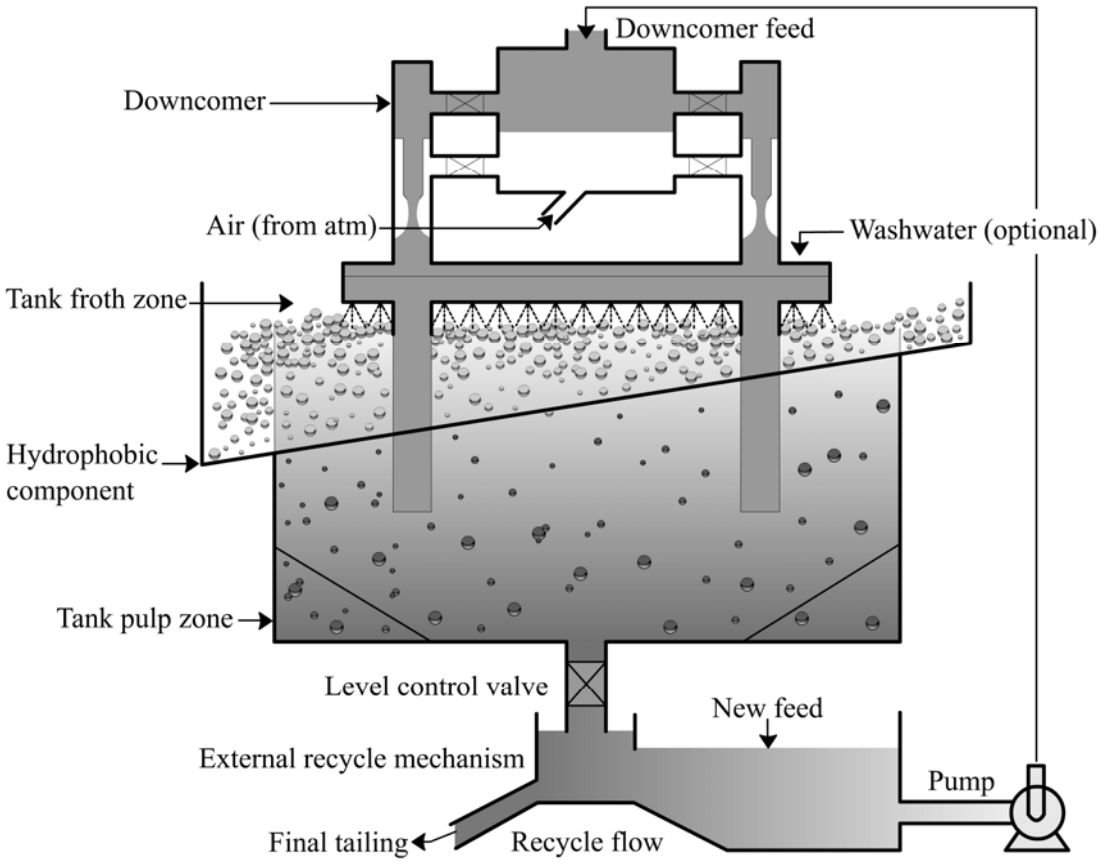

Figure 2. 8 Illustration of Jameson cell (Xstrata Technology, 2009)

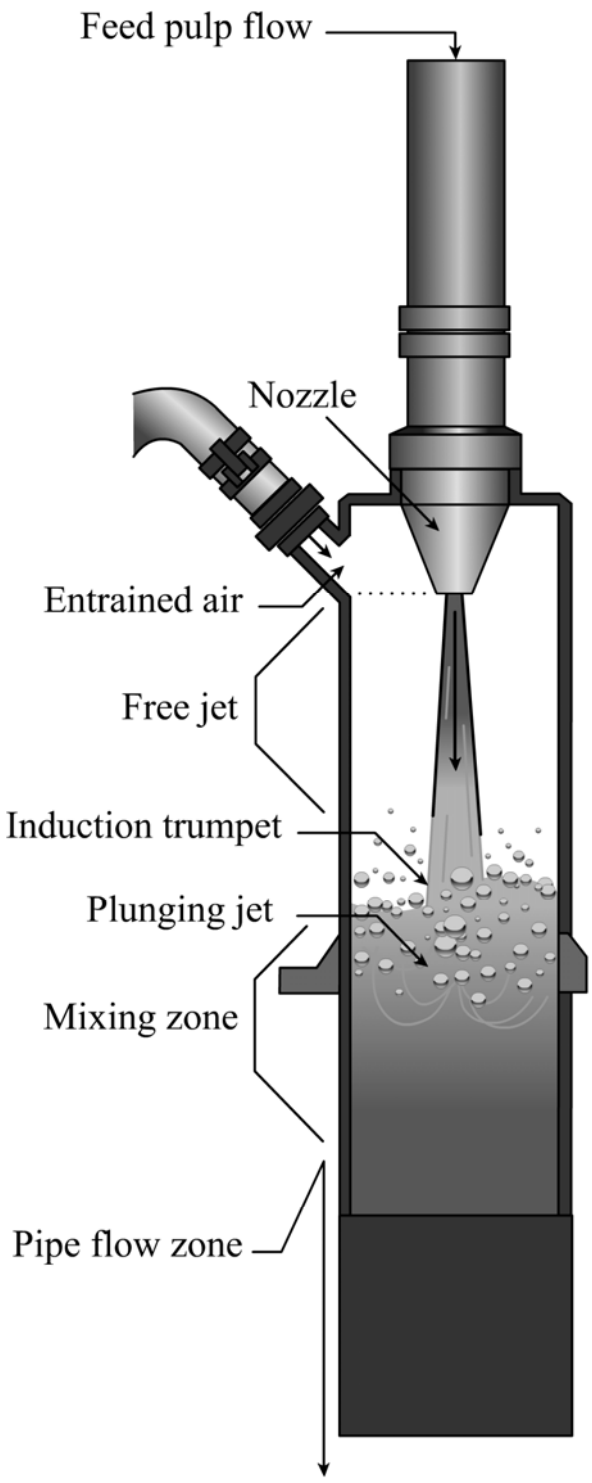

Figure 2. 9 Cut-away diagram of downcomer (Xstrata Technology, 2009)

CHAPTER 3

SUPERFICIAL GAS VELOCITY

3.1 – Some background

Superficial gas velocity (J_g) is the gas dispersion parameter selected for the gas distribution (cell mapping) task. It was defined in Chapter 1 as volumetric gas flow rate divided by cross-sectional area. Various research groups have developed techniques for measuring the parameter in industrial cells (Jameson and Allum, 1984; Falutsu, 1994; Gorain et al., 1996; Dahlke et al., 2001; Yianatos et al., 2001; Grau and Heiskanen, 2003; Torrealba-Vargas, 2004). A brief review of these techniques is given.

Jameson and Allum (1984) reported a technique that consisted of introducing a cylinder full of water into a flotation machine below the froth interface. As bubbles enter the cylinder the pressure inside increases and consequently the liquid level inside the cylinder is pushed down. The time to travel between two level marks is related to the superficial gas velocity.

Falutsu (1994) proposed a method that consisted in pumping slurry from the collection (pulp) zone through a probe immersed at a known depth in the machine. The J_g was calculated from a correlation relating gas flow rate, slurry flow rate and percent solids. The gas flow rate was measured by an inverted cylinder. This correlation varied depending on cell geometry and percent solids.

Gorain et al. (1996) reported a method that is an automated version of the inverted cylinder reported by Jameson and Allum. It consists of a tube with a water inlet valve, an air outlet valve and a pneumatically controlled pinch valve at the immersed tip that allows re-filling the tube with water for a subsequent measurement. The time taken for the descending water level to travel a known distance is measured and related to J_g.

Yianatos et al. (2001) reported a continuous method using a tube connected to a mass flow meter and a vacuum regulator at the top. The pressure inside the tube is maintained at atmospheric by the vacuum regulator, leading to a direct measurement of gas flow rate by the mass flow meter. The main characteristic of this method is that it allows direct and continuous measurements of J_g. Grau and Heiskanen (2003) upgraded this technique by adding a gas drying column and particle filter.

3.2 - McGill On-Off J_g Sensor (Gomez and Finch, 2007)

This sensor comprises two tubes (typically 10 cm diameter), the "sensor" and the "bubbler", closed at the top and housing a connection to a valve and pressure transducer (Figure 3. 1). The pressure transducers are connected to an electronic board that acquires the signals to a computer for further analysis. The tube labeled sensor is used to collect the air bubbles and record the increase in pressure when the valve is closed. The J_g is dependent on the rate of increase of pressure (dP/dt) according to (Torrealba-Vargas, 2004),

$$J_g = \left[\frac{P_{atm} + \rho_b \cdot H_L}{\rho_b \cdot \left[P_{atm} + \rho_b \cdot (H_L - H_0) \right]} \right] \cdot \frac{dP}{dt} \quad \text{(cm/s)} \qquad (3.\ 1)$$

where P_{atm} is the atmospheric pressure in cmH_2O, H_L is the total length of the sensor tube in cm, H_0 is the distance from the top of the sensor tube to the lip of the flotation machine in cm, and ρ_b is the density of the aerated slurry calculated using the pressure difference between the sensor and bubbler tubes when both are full of air,

$$\rho_b = \frac{P2 - P1}{H_{BD}} \quad (g/cm^3) \qquad (3.2)$$

where P1 and P2 are pressure measured in cmH_2O and H_{BD} is the distance, in cm, between the bottom of the two tubes.

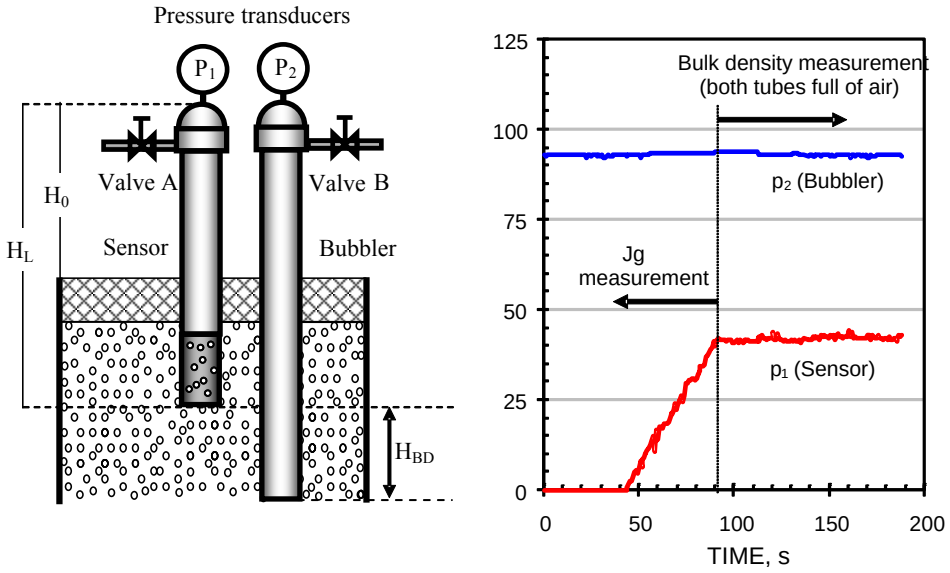

Figure 3. 1 Schematic of McGill on-off superficial gas velocity sensor and example pressure signals

3.3 - McGill Continuous J_g Sensor (Torrealba et al., 2004)

This technique uses the same sensor tube but with a pressure transmitter and a calibrated orifice connected at the top (Figure 3. 2). Bubbles enter the tube and the air expels through the calibrated orifice. The liquid level in the tube depresses till steady state is reached (air in as bubbles equals air out through orifice). The J_g is estimated from the pressure drop across the orifice (ΔP) using a calibration of the form,

$$J_g = a \cdot \sqrt{\frac{\Delta P}{\rho_a}} + b \qquad (3.3)$$

where a and b are empirical constants, and ρ_a is the density of the air.

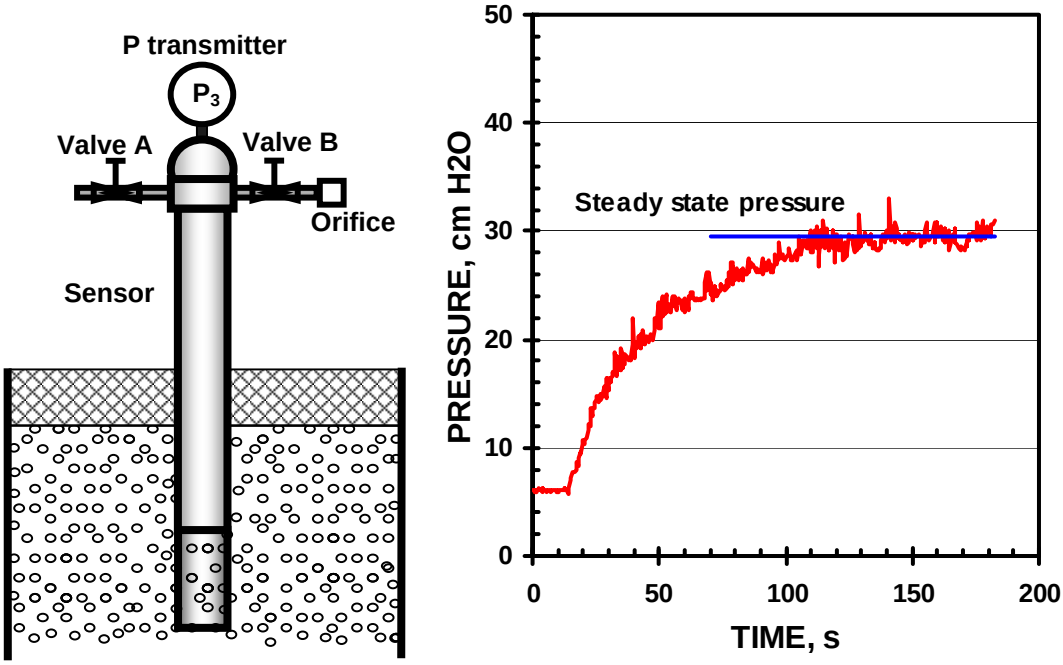

Figure 3. 2 Schematic of McGill continuous superficial gas velocity sensor and example pressure signal

3.4 – Fundamental analysis of McGill on-off sensor

Torrealba-Vargas et al. (2004) reported a difference between J_g when measured with the on-off and continuous techniques in tests on an industrial flotation cell (i.e., three phase system), giving in all cases a higher J_g when measured by the continuous method. There was no difference, however, between the two methods when J_g was measured in a water-air system (Torrealba-Vargas, 2004). Following is an analysis of the on-off mode with the purpose of finding the reason for the difference.

3.4.1 – McGill J_g on-off model of Torrealba-Vargas (2004)

The starting point of the derivation is the air mass balance with respect to the air entering the tube,

$$q_{in} = \frac{d(\rho_a \cdot V_a)}{dt} \tag{3. 4}$$

where q_{in} is the mass flow rate of air entering the tube, ρ_a is the density of the air and V_a is the volume of the air. Pressure is included using the chain rule,

$$q_{in} = \frac{d(\rho_a \cdot V_a)}{dP} \cdot \frac{dP}{dt} \tag{3. 5}$$

where,

$$\frac{d(\rho_a \cdot V_a)}{dP} = V\frac{d\rho_a}{dP} + \rho_a \frac{dV_a}{dH} \cdot \frac{dH}{dP} \tag{3. 6}$$

As the system operates at low absolute pressure (less than 130 kPa), the ideal gas law is assumed,

$$\rho_a = \frac{28.8 \cdot P}{RT} \tag{3. 7}$$

where 28.8 kg/kmol is the average molecular weight of air. Calculating the derivative of the air density with respect to pressure,

$$\frac{d\rho_a}{dP} = \frac{28.8}{RT} \tag{3. 8}$$

and expressing the volume as a function of the tube cross-sectional area,

$$V_a = A_t \cdot H \tag{3. 9}$$

gives the derivative of V with respect to H,

$$\frac{dV_a}{dH} = A_t \tag{3. 10}$$

Figure 3. 3 identifies the physical location of the variables with respect to the sensor. The key variables are: H and P, where H is the distance from the top of the sensor to the free surface of the aerated slurry inside the sensor at a determined time; and P the hydrostatic pressure outside the sensor at the level of the free surface of the aerated slurry inside the sensor, i.e., it is assumed that the density of the aerated slurry outside the sensor tube equals the density of the aerated slurry inside the tube. The expression for P is given by,

$$P = P_{atm} + \rho_b \cdot g(H - H_0) \tag{3. 11}$$

and defines the derivative of H with respect to pressure, as,

$$\frac{dH}{dP} = \frac{1}{\rho_b \cdot g} \tag{3. 12}$$

Substituting Equation (3. 7), Equation (3. 8), Equation (3. 9), Equation (3. 10) and Equation (3. 12) into Equation (3. 6) and re-arranging,

$$\frac{d(\rho_a \cdot V_a)}{dP} = \frac{28.8 \cdot A_t}{RT}\left(\frac{\rho_b \cdot g \cdot H + P}{\rho_b \cdot g}\right) \tag{3. 13}$$

and substituting Equation (3. 13) into Equation (3. 5) gives,

$$q_{in} = \frac{28.8 \cdot A_t}{RT}\left(\frac{\rho_b \cdot g \cdot H + P}{\rho_b \cdot g}\right) \cdot \frac{dP}{dt} \tag{3. 14}$$

where,

$$q_{in} = \rho_a \cdot Q_g = \rho_a \cdot J_g \cdot A_t \tag{3. 15}$$

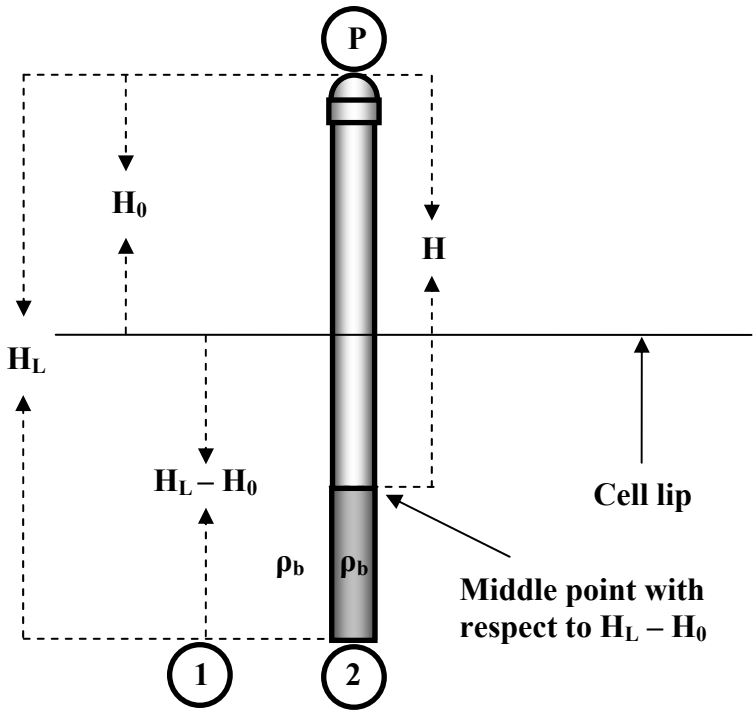

Figure 3. 3 McGill on-off model variables

Equation (3. 15) represents the mass of air entering the tube; therefore the density of the air has to be calculated at the pressure observed at the sensor tip (P_L),

$$q_{in} = \frac{28.8 \cdot P_L}{R \cdot T} \cdot J_g \cdot A_t \tag{3. 16}$$

Substituting Equation (3. 16) into Equation (3. 15) and re-arranging gives,

$$J_g = \left(\frac{\rho_b \cdot g \cdot H + P}{P_L \cdot \rho_b \cdot g} \right) \cdot \frac{dP}{dt} \tag{3. 17}$$

Equation (3. 17) is a function of H and P that has to be evaluated to obtain the final expression. The distance H can vary from H_0 to H_L, thus a choice is needed. It was considered appropriate to express H as the distance from the top of the sensor to the

middle point with respect to H_L-H_0 (Figure 3. 3), i.e., the middle of the sensor section immersed in the cell, given by

$$H = H_0 + \frac{H_L - H_0}{2} = \frac{H_L + H_0}{2} \tag{3. 18}$$

Substituting Equation (3. 11) and Equation (3. 18) into Equation (3. 17) and re-arranging gives,

$$J_g = \left(\frac{P_{atm} + \rho_b \cdot g \cdot H_L}{P_L \cdot \rho_b \cdot g} \right) . \frac{dP}{dt} \tag{3. 19}$$

Equation (3. 19) implies that ρ_b is the same inside and outside the sensor. This assumption apparently holds in the gas-liquid system as the on-off and continuous versions agree, indicating the gas holdup in the sensor is the same as that outside. There seems no reason this equality in gas holdup should not hold in the three phase. However, there remains the possibility that the aerated slurry density is not the same inside and outside the sensor. The argument is that inside the tube there is no mechanism to maintain particles in suspension; therefore the heavier particles can sediment, generating a lower slurry density and therefore lower aerated slurry density inside the sensor. The current on-off technique relies on measurements of ρ_b by using difference in pressure given by the bubbler tube and the sensor tube, which is an estimate of the aerated slurry density outside the sensor, ρ_b. A correction to the aerated slurry density inside the tube is required until the technique is modified to measure this density directly.

3.4.2 – McGill J_g on-off mode: model correction

Figure 3. 4 is Figure 3. 3, but with the aerated slurry density outside and inside the sensor, ρ_b and ρ_t respectively, no longer being taken as the same.

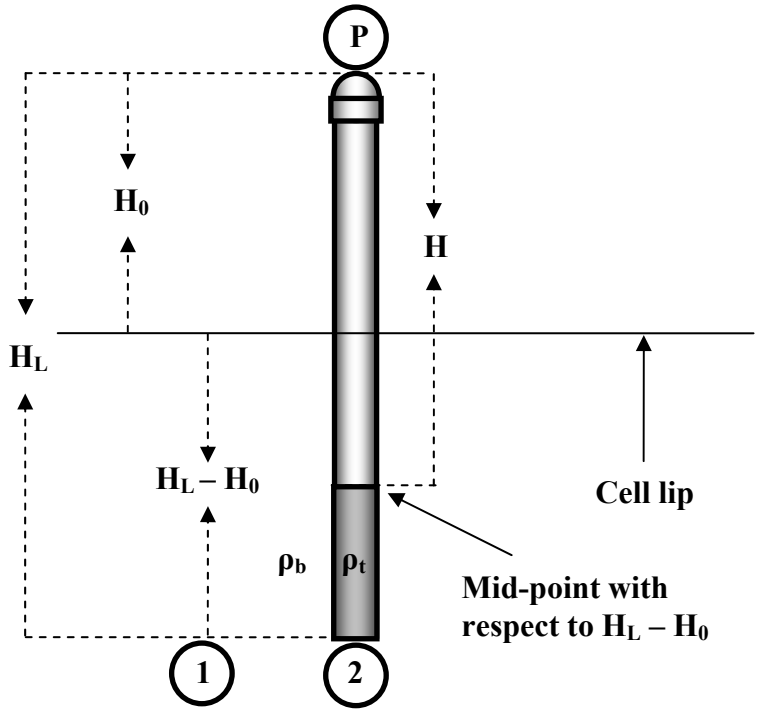

Figure 3. 4 Introducing model variables

The derivation is the same from Equation (3. 4) to Equation (3. 10). The correction enters by defining the pressure inside the tube differently. The basis is that: "Any two points at the same elevation in a continuous mass of the same static fluid will be at the same pressure" (White, 2006). Figure 3. 4 shows the selected two points, 1 and 2. The equality is expressed as,

$$P_{atm} + \rho_b \cdot g \cdot (H_L - H_0) = P + \rho_t \cdot g \cdot (H_L - H) \qquad (3.\ 20)$$

where the terms on the left and right hand side represent points 1 and 2, respectively. Solving for P gives,

$$P = P_{atm} + \rho_b \cdot g \cdot (H_L - H_0) - \rho_t \cdot g \cdot (H_L - H) \tag{3. 21}$$

and solving for H gives,

$$H = \frac{P + \rho_t \cdot g \cdot H_L - P_{atm} - \rho_b \cdot g \cdot (H_L - H_0)}{\rho_t \cdot g} \tag{3. 22}$$

Calculating the derivative dH/dP gives,

$$\frac{dH}{dP} = \frac{1}{\rho_t \cdot g} \tag{3. 23}$$

Substituting Equation (3. 7), Equation (3. 8), Equation (3. 9), Equation (3. 10), Equation (3. 15) and Equation (3. 23) into Equation (3. 5) and re-arranging gives,

$$J_g = \left(\frac{\rho_t \cdot g \cdot H + P}{P_L \cdot \rho_t \cdot g} \right) \cdot \frac{dP}{dt} \tag{3. 24}$$

The difference between Equation (3.17) and Equation (3. 24) is that the first is a function of the aerated slurry density outside the tube and the second is a function of the aerated slurry density inside the tube. Substituting Equation (3. 18) and Equation (3. 21) into Equation (3. 24) and re-arranging gives,

$$J_g = \left(\frac{P_{atm} + \rho_t \cdot g \cdot H_0 + \rho_b \cdot g \cdot (H_L - H_0)}{P_L \cdot \rho_t \cdot g} \right) \cdot \frac{dP}{dt} \tag{3. 25}$$

Equation (3. 25) is the corrected model and requires knowledge of the aerated slurry density inside the tube (ρ_t); and note when $\rho_t = \rho_b$ Equation (3. 25) reduces to Equation (3. 19).

3.4.3 – Estimation of aerated slurry density inside the tube, ρ_t

The first step is to define ρ_b in terms of the mass of water, m_w, mass of solids, m_s, (mass of gas is neglected) and total volume, including the air (V_T),

$$\rho_b = \frac{m_s + m_w}{V_T} \tag{3. 26}$$

For simplicity, it is proposed that ρ_t is an intermediate value between ρ_b and the density of aerated water (ρ_w),

$$\rho_t = \frac{\rho_b + \rho_w}{2} \tag{3. 27}$$

where ρ_w is arbitrarily defined as mass of water divided by the same total volume V_T,

$$m_w = \rho_w \cdot V_T \tag{3 .28}$$

It is convenient to express m_s as a function of m_w,

$$m_s = \eta \cdot m_w \tag{3. 29}$$

where η is the solids/liquid ratio (m_s/m_w). Substituting Equation (3. 28) into Equation (3. 26) gives,

$$\rho_b = \frac{m_w \cdot (1+\eta)}{V_T} \tag{3. 30}$$

Substituting Equation (3. 28) into Equation (3. 30) and solving for ρ_w gives,

$$\rho_w = \frac{1}{(1+\eta)} \cdot \rho_b \tag{3. 31}$$

and substituting Equation (3. 31) into Equation (3. 27) gives,

$$\rho_t = 0.5 \cdot \rho_b \cdot \left(1 + \frac{1}{1+\eta}\right) \tag{3. 32}$$

For convenience, let $m_s + m_w = 100$ (i.e., 100 %), then,

$$\eta = \frac{m_s}{100 - m_s} \tag{3. 33}$$

then subtituting Equation (3. 33) into Equation (3. 32) and re-arranging gives,

$$\rho_t = 0.005 \cdot \rho_b \cdot (200 - m_s) \tag{3. 34}$$

Equation (3. 34) expresses ρ_t as a function of ρ_b and m_s. The plot of this equation with m_s in the range 0-50 % is given in Figure 3. 5.

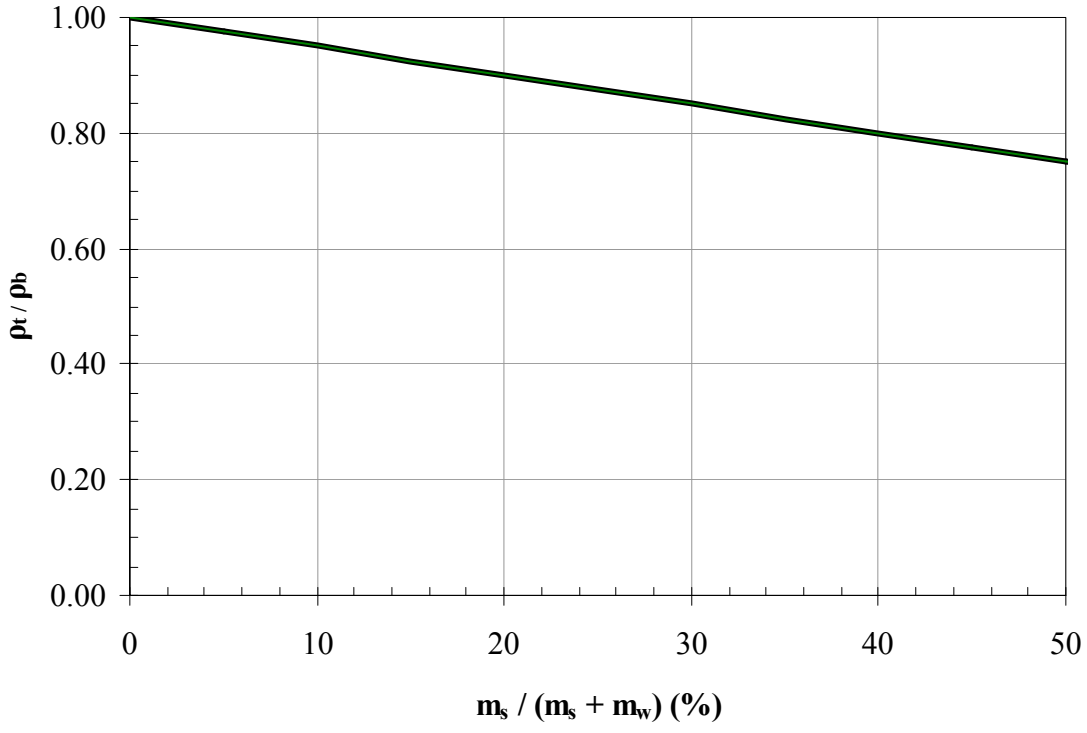

Figure 3. 5 Estimated variation of ρ_t as a function of weight percent solids in slurry

Taking m_s = 35 % as 'typical', Equation (3. 34) becomes,

$$\rho_t = 0.83 \cdot \rho_b \tag{3. 35}$$

giving a first approximation for measuring the corrected gas velocity, J_{gc}, as,

$$J_{gc} = \left(\frac{P_{atm} + \rho_b \cdot g \cdot (H_L - 0.17 \cdot H_0)}{0.83 \cdot P_L \cdot \rho_t \cdot g} \right) \cdot \frac{dP}{dt} \tag{3. 36}$$

Figure 3. 6 compares Equation (3. 19) and Equation (3. 36) based on the parameters given in Table 3. 1. It can be seen that the corrected model (J_{gc}) gives a higher gas velocity. This coincides with the observation that in air-slurry systems J_g continuous > J_g on-off noted by Torrealba-Vargas et al. (2004), and that the origin is a lower aerated slurry density inside the tube than outside. In the example in Figure 3. 6, the difference between the two models is 17%. The magnitude of the difference will change depending on the combination of parameters but in all cases J_{gc} will give a higher value, than J_g.

Table 3. 1 Set of parameters used for comparison between Jg models

Parameter	Value
P_{atm} (cmH2O)	1033
P_L (cmH2O)	1133
H_L (cm)	300
H_0 (cm)	200
ρ_b (g/cm^3)	1

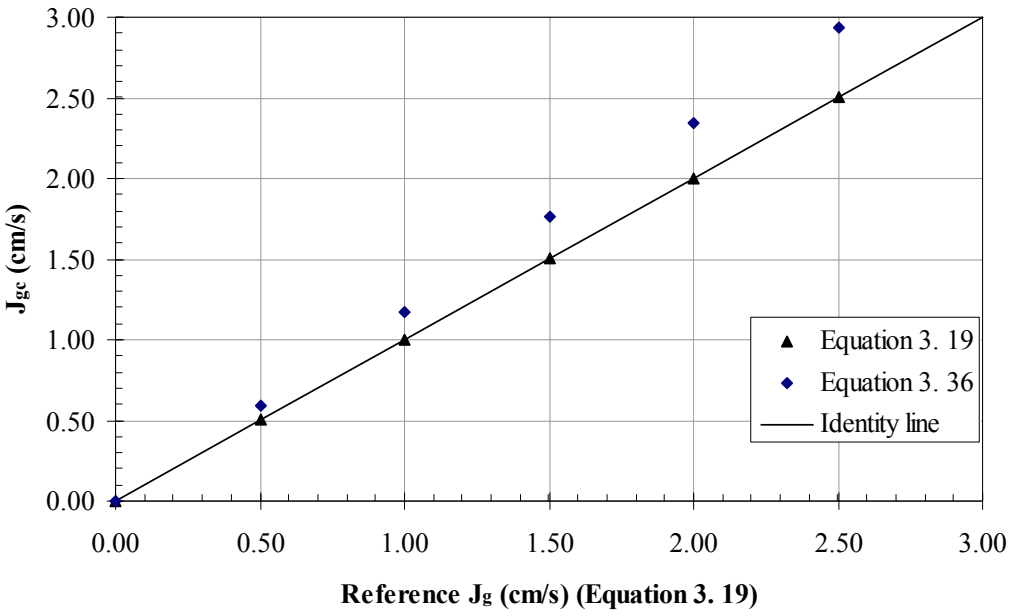

Figure 3. 6 Comparison between J_g given by Equation (3. 19) and J_{gc} given by Equation (3. 36)

3.4.4 – Using McGill on-off sensor to give 'continuous' J_g

The fundamental analysis presented in the previous section implies that the real J_g in an air-slurry system is given by the continuous technique, which does not need a correction. Another important advantage is that it provides a continuous signal more suitable for control purposes. A drawback with the continuous technique is that at some operating conditions the froth inside the tube builds and blocks the orifice affecting the calibration (Torrealba-Vargas, 2004). In contrast, froth buildup does not affect the on-off sensor. Another attractive feature of the on-off technique is that it does not require calibration which becomes a maintenance issue. If the on-off technique can give a continuous signal, or at least one at high enough frequency to effectively be continuous, it could also be used for control purposes.

The current procedure to calculate J_g with the on-off method requires off-line data processing. After the signals are collected and stored in a computer, the J_g is calculated with a spreadsheet application (MS Excel) that locates and determines the slopes required for the calculations. Figure 3. 7 shows an example of pressure signals collected to calculate J_g. Note that only one slope per "on-off" cycle is taken. Commonly more than 100 points are collected. Recommended practice is to take 5 "on-off" cycles (5 slopes) (Gomez and Finch, 2007).

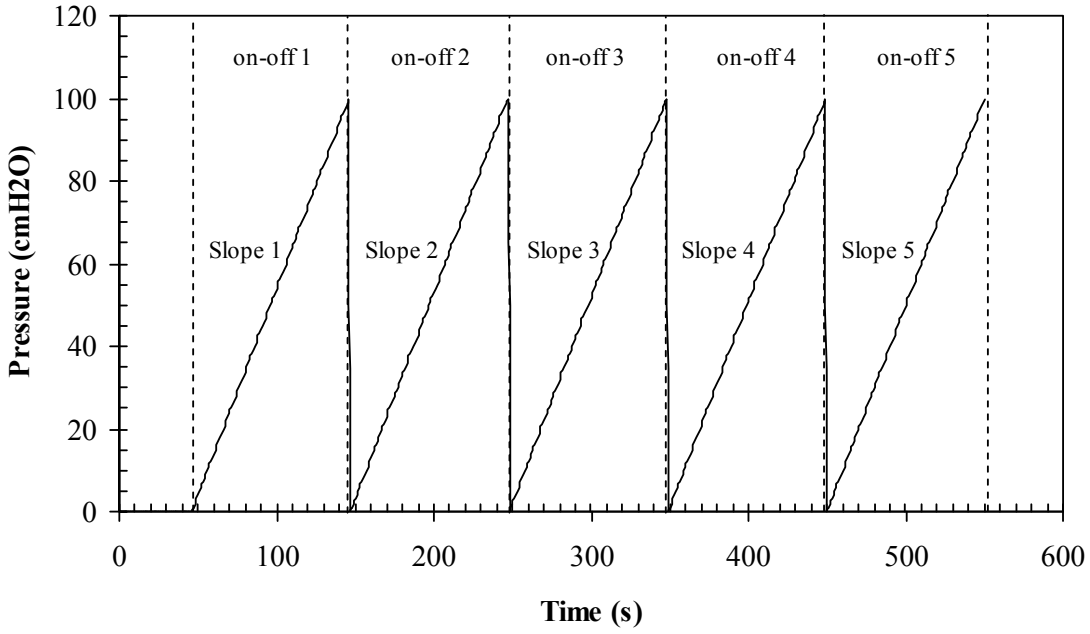

Figure 3. 7 Illustration of pressure signals used to calculate J_g using McGill "on-off" device (current procedure)

It is possible to obtain more frequent J_g estimates. Recall that calculation of J_g is based upon collection of slopes. For example, the standard procedure consists in collecting 5 slopes and calculates J_g from the average slope of those 5. The Central Limit Theorem states that the minimum recommended sample size is 30 (Montgomery and Runger, 2003). It is not practical to take 30 "on-off" cycles for control purposes because the required time to report a single value of J_g would be too long. To address this requirement, it is assumed that it is not strictly necessary to consider the complete "on-off" curve to calculate the slope. If the "on-off" cycle is divided into parts then it is possible to increase the number of slopes (samples). For example, if 5 "on-off" cycles with 100 points are divided into slopes comprising 5 points then each "on-off" cycle will

contribute 20 slopes to calculate a mean J_g for a total of 100 slopes given the standard 5 "on-off" cycles.

Two possible techniques to divide the "on-off" curves are presented termed "independent slopes" and "overlapped slopes". The independent slopes technique divides the "on-off" curves into several small sections. Figure 3. 8 shows an example that calculates one slope every 5 points ensuring that each point is used only once. The overlapped slopes technique divides the "on-off" curves into small sections that are not independent of each other (Figure 3. 9). For example, if the pressure signal is collected every 1 s and the resulting "on-off" curves have 100 points then this technique will provide 96 slopes of 5 points per "on-off" curve or 480 slopes considering 5 "on-off" curves. One implication is that the overlapped slopes technique has a better dynamic response, i.e., this technique will detect J_g changes in the process faster than using the independent slope technique.

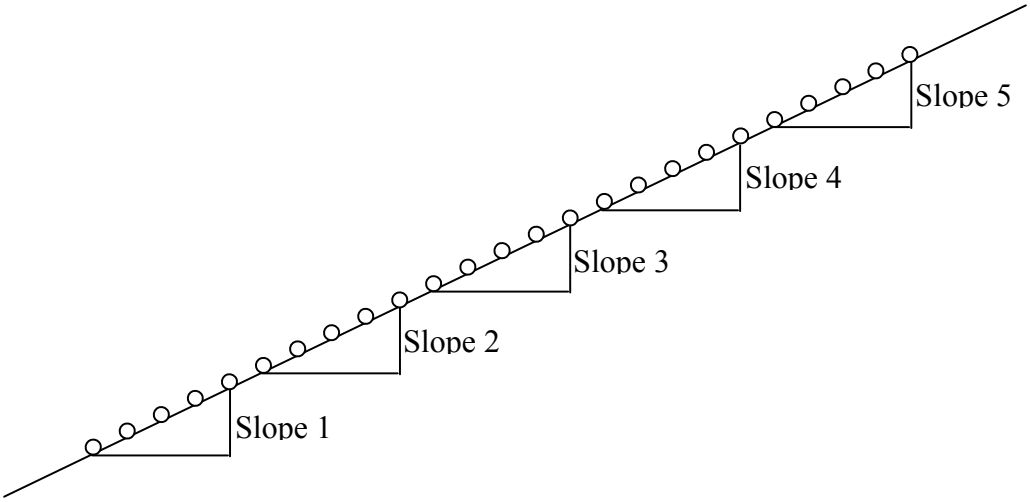

Figure 3. 8 Illustration of the "independent slopes" concept

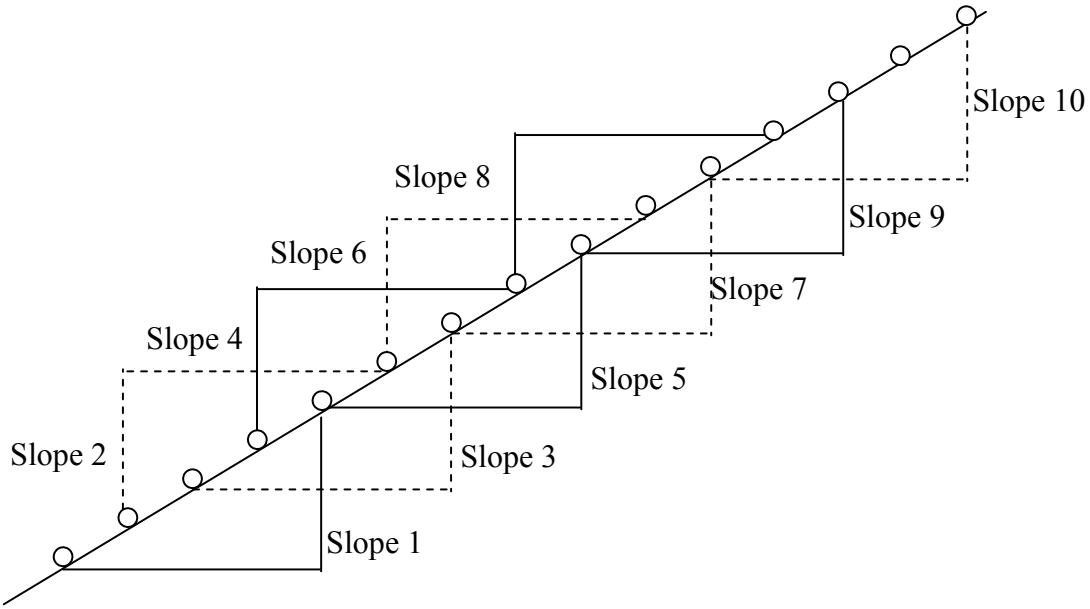

Figure 3. 9 Illustration of the "overlapped slopes" concept

To test the dynamic response, the behavior of the two algorithms was simulated. The selected test consisted of 2 step changes, the first up from 0.5 to 1 cm/s and the second down from 1 to 0.5 cm/s. Figure 3. 10 shows the simulated "on-off" curves. Figure 3. 11 shows the dynamic response using the two techniques. A significant difference is seen between the two. The overlapped slopes technique responds within ca. 1.5 minutes of the step change while the independent slopes technique responded on average within 8 minutes. From these results it is concluded that the overlapped slopes technique is more suitable to determine J_g from the "on-ff" J_g sensor to be considered for air control purposes.

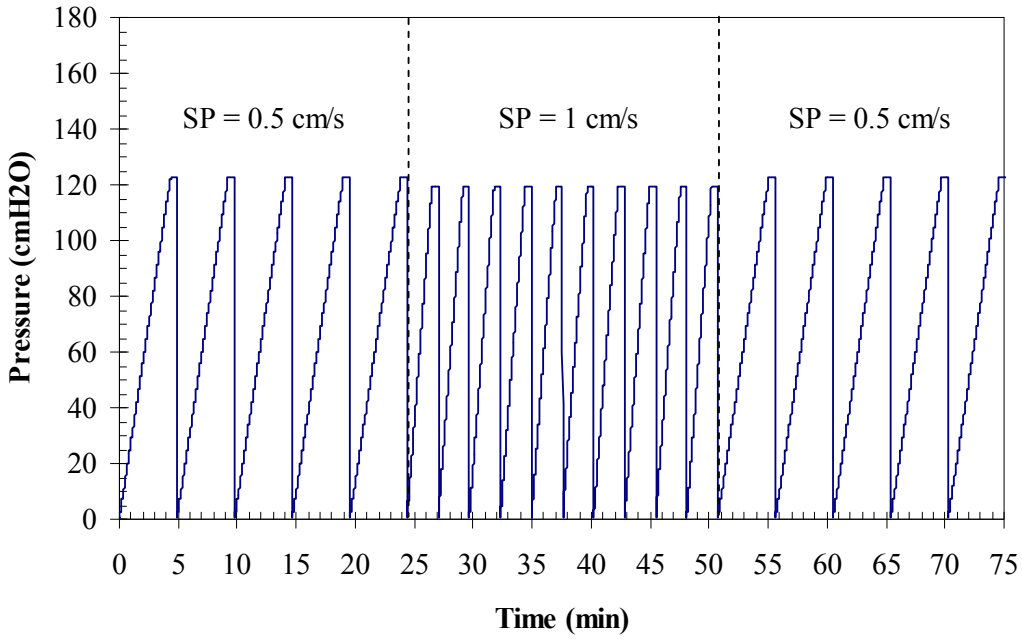

Figure 3. 10 Simulated "on-off" curves corresponding to the 2 set-point changes

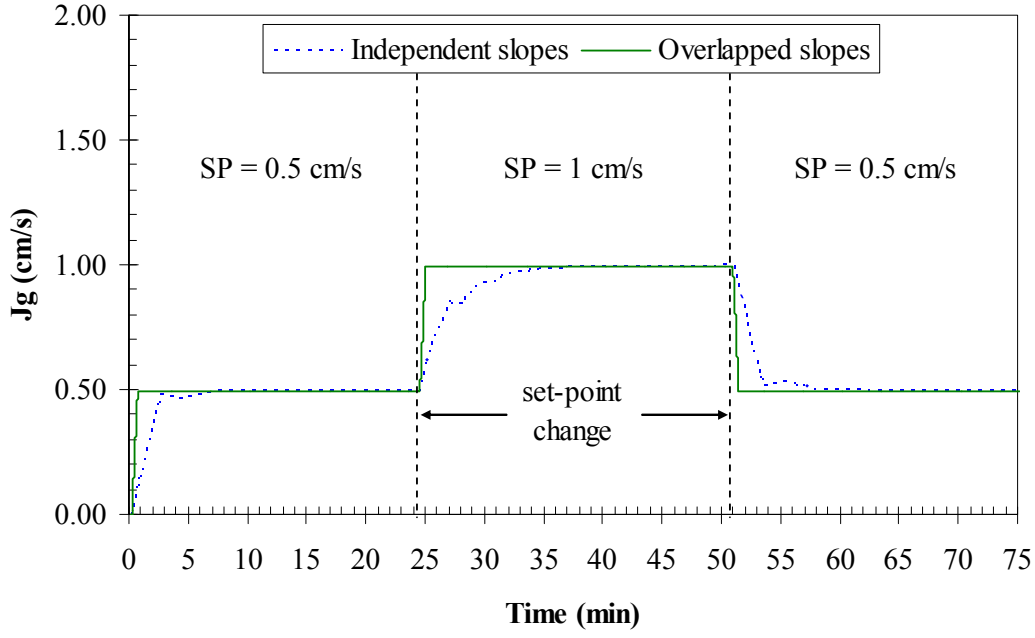

Figure 3. 11 Dynamic response comparison between "independent slopes" and "overlapped slopes" techniques

CHAPTER 4

GAS DISTRIBUTION IN FLOTATION CELLS

4.1 - Introduction

Gas distribution was defined in Chapter 1 as the spreading of the air bubbles throughout the cell volume. Understanding gas distribution gives insight into the flow patterns in the cell, being a source of information for research and design (Sanwani et al., 2006). It is intuitive that best metallurgical results are likely associated with uniform distribution of air.

One way to determine gas distribution is by taking radial and/or axial measurements of one of the gas dispersion properties previously introduced; gas velocity, gas holdup and/or bubble size (Xu et al., 1992; Gorain et al., 1996; Dahlke et al., 2001; Gomez et al., 2003; Doucet, 2006; Sanwani et al., 2006). In this work, gas distribution is reported based on measurements of gas velocity as a function of radial distance at a common depth, referred to as "radial J_g mapping".

In prior work it was demonstrated that there is radial symmetry in gas distribution in mechanical cells determined by measuring gas velocity at different radial positions at a constant depth (Dahlke et al., 2001; Doucet, 2006).

4.2. - Analysis of parabolic profile

Gas velocity was defined in Chapter 1 as a volumetric gas flow rate (Q_g) through an area A,

$$J_g = \frac{Q_g}{A} (cm/s) \qquad (1.\ 1)$$

Measuring gas velocity at several radial distances at a constant depth (radial J_g mapping), produces a "cell gas velocity profile". Figure 4. 1 illustrates a possible profile compared to the ideal (uniform) in a flotation cell of 100 cm radius (selected for convenience). Based on the previous finding of symmetry, the profiles are considered to be parabolic and represented by,

$$J_g = \beta - \alpha \cdot r^2 \qquad (4.\ 1)$$

where β and α are empirical constants.

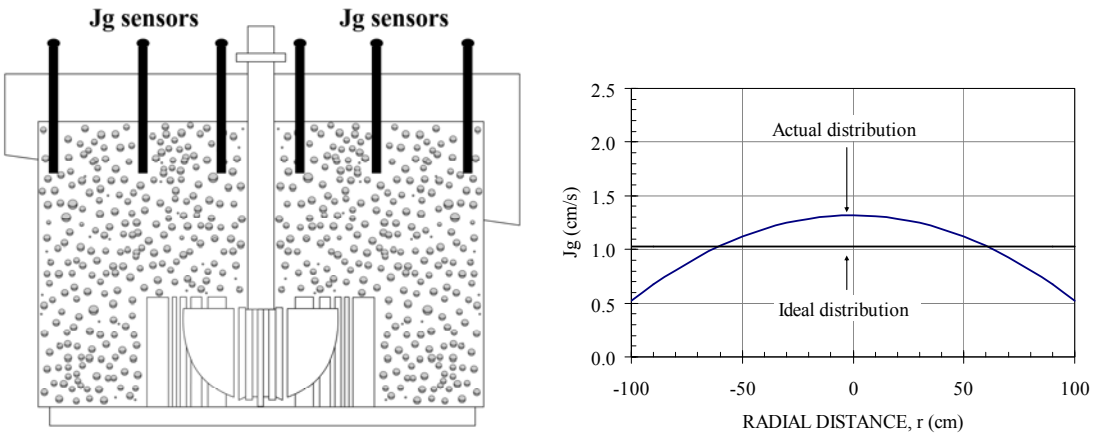

Figure 4. 1 Illustration of gas distribution measurement principle: left, experimental set-up of J_g sensors; right, ideal and possible ("actual") profiles

Assuming cylindrical geometry, Equation (4. 2) can be used to calculate the volumetric gas flow rate passing through an arbitrary cross-sectional area in the flotation cell by integration of the J_g profile; this calculation sums gas flow rate contributions of infinitesimal annular regions with differential area $dA = 2 \pi r\, dr$ (White, 2006),

$$Q_g = \int J_g \cdot dA \tag{4. 2}$$

Substituting Equation (4. 1) into Equation (4. 2) gives,

$$Q_g = \int_{r1}^{r2} \left(\beta - \alpha \cdot r^2\right) \cdot 2\pi\, r\, dr \tag{4. 3}$$

with the solution,

$$Q_g = \pi \cdot \beta \cdot \left(r_2^2 - r_1^2\right) - \frac{\pi \cdot \alpha}{2}\left(r_2^4 - r_1^4\right) \tag{4. 4}$$

where r_1 and r_2 are the internal and external radius of a circular or annular region where the gas flow rate is being calculated. It is convenient to express the radial distance as a dimensionless magnitude, $\varphi = r / R$ where R is the radius of the cell. Total gas flow rate through the cell in terms of the dimensionless radial distance is calculated based on the integration limits $\varphi_1 = 0$ and $\varphi_2 = 1$,

$$Q_{g\,(total)} = \pi \cdot \beta - \frac{\pi \cdot \alpha}{2} \tag{4. 5}$$

The gas flow rate (as a function of φ) expressed as a dimensionless magnitude is achieved dividing Equation (4. 4) by Equation (4. 5),

$$Q_{g(fraction)} = \frac{2 \cdot \beta \cdot \left(\varphi_2^2 - \varphi_1^2\right) - \alpha \cdot \left(\varphi_2^4 - \varphi_1^4\right)}{2 \cdot \beta - \alpha} \tag{4. 6}$$

Another way to calculate $Q_{g(fraction)}$ is by expressing Equation (4. 6) as a function of the area:

$$Q_{g(fraction)} = \frac{2 \cdot \beta \cdot \lambda - \alpha \cdot \lambda^2}{2 \cdot \beta - \alpha} \qquad (4.\ 7)$$

where $\lambda = A_\varphi / A_{cell}$ and A_φ is the dimensionless cross-sectional area for an arbitrary φ and A_{cell} is the cell cross-sectional area, i.e., when $\varphi = 1$. Figure 4. 2 shows $Q_{g(fraction)}$ as a function of radial distance and as a function of area. These plots are useful to quantify gas flow rate at specific geometric locations: for example, based on the data presented in the figure, the cumulative fraction of gas flow from the cell center up to 0.5 of the radius is 33% and the cumulative gas flow measured from the machine center up to 0.5 of the area is 60% corresponding to a radius of 0.7.

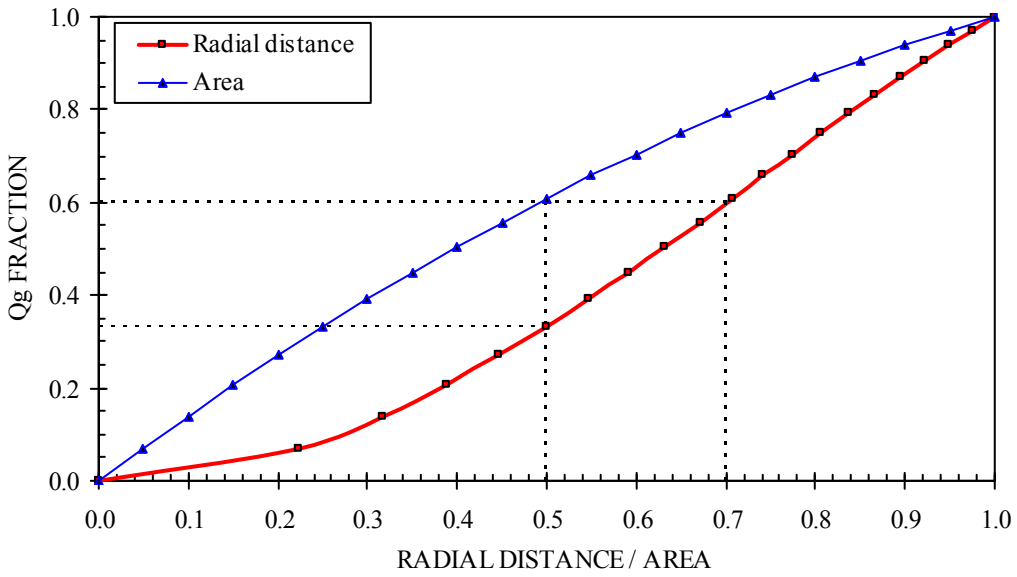

Figure 4. 2 Cumulative gas flow rate as a function of radial distance and area fraction

Comparison of gas distributions can be made using the cumulative gas flow rate curve. Figure 4. 3 and Figure 4. 4 show typical and uniform distributions as a function of area and radius, respectively.

4.3 - Gas distribution deviation index

There is a deviation (difference) between the actual and the ideally uniform distribution that can be calculated from the $Q_{g(fraction)}$ as a function of either area or radius. This deviation is defined by the area of the region between the two curves, Δ_A when calculated based on area and Δ_R when calculated on a basis of radius. These differences can be used to determine a parameter to characterize the air distribution in a flotation cell.

The Δ_A is given by,

$$\Delta_A = \int_0^1 \frac{2\cdot\beta\cdot\lambda - \alpha\cdot\lambda^2}{2\cdot\beta - \alpha}\cdot d\lambda - \int_0^1 \lambda\cdot d\lambda \tag{4. 8}$$

with the solution,

$$\Delta_A = \frac{1}{2\cdot\beta - \alpha}\left(\beta - \frac{\alpha}{3}\right) - 0.5 \tag{4. 9}$$

and the Δ_R is given by,

$$\Delta_R = \int_0^1 \frac{2\cdot\beta\cdot\varphi^2 - \alpha\cdot\varphi^4}{2\cdot\beta - \alpha}\cdot d\varphi - \int_0^1 \varphi^2\cdot d\varphi \tag{4. 10}$$

with the solution,

$$\Delta_R = \frac{1}{2\cdot\beta - \alpha}\cdot\left(\frac{2}{3}\cdot\beta - \frac{\alpha}{5}\right) - \frac{1}{3} \tag{4. 11}$$

The difference as a fraction of the area under the uniform distribution curve is called the DDI (distribution deviation index) that can be calculated on the basis of area or radius (DDI_A and DDI_R, respectively). Uniform distribution has a DDI = 0.

$$DDI_A = \frac{\Delta_A}{0.5} \tag{4. 12}$$

$$DDI_R = \frac{\Delta_R}{1/3} \tag{4. 13}$$

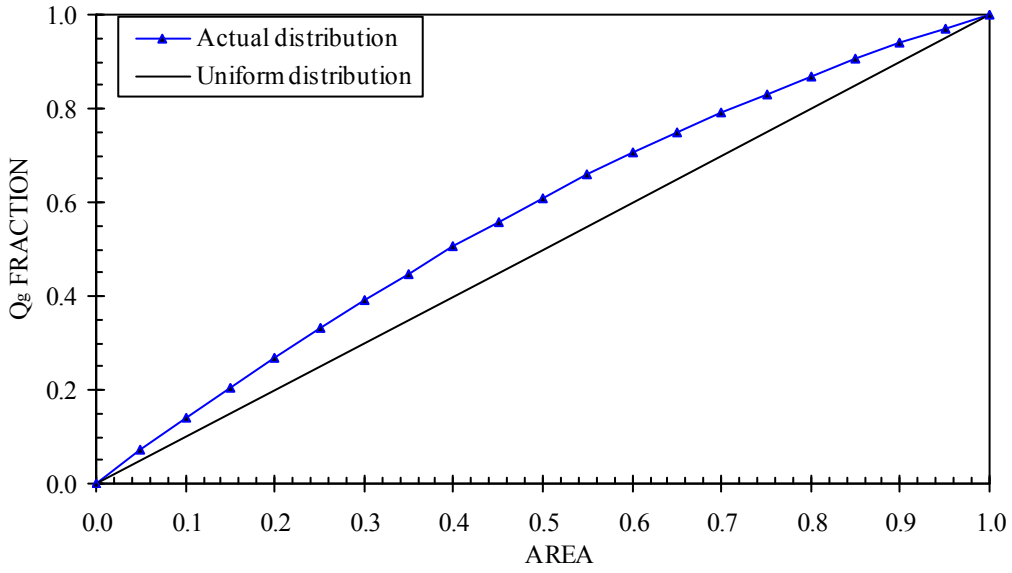

Figure 4. 3 Cumulative dimensionless gas flow rate as a function of area fraction

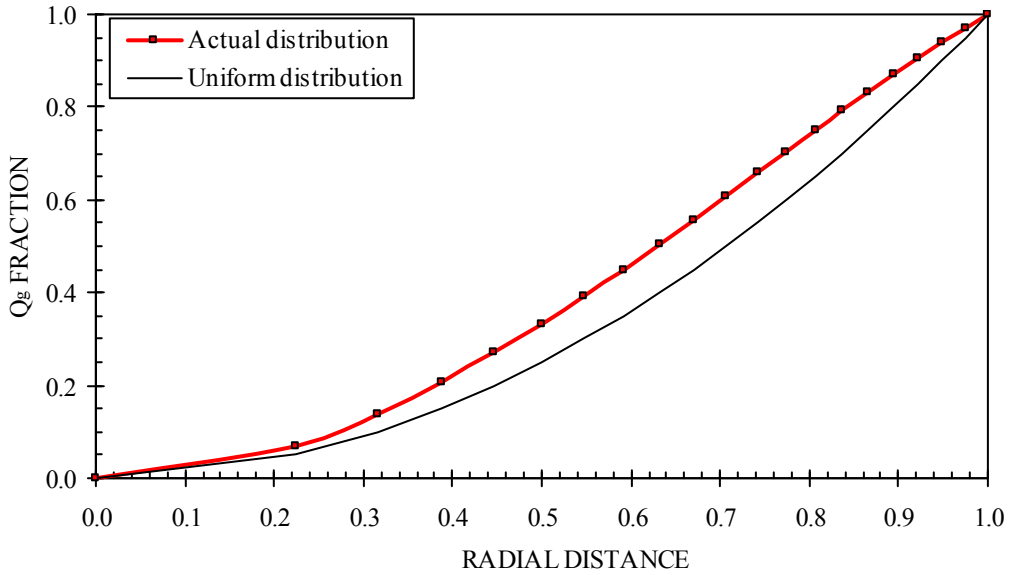

Figure 4. 4 Cumulative dimensionless gas flow rate as a function of dimensionless radial distance

4.4 - Sampling point for cell average J_g

Interpretation of gas distribution data provides a method to select a sampling point when a single measurement is required; for example the cell average J_g ($J_{g(av)}$). Dividing the cell into a number of annular regions of equal area it is possible to determine variations of $Q_{g(fraction)}$ as a function of radial distance from the machine center (Figure 4. 5). The horizontal dashed line in Figure 4. 5 represents the fraction of gas flow rate when uniformly distributed through annular regions for the case where A_{cell} is divided into 200 annular regions (i.e., approximating an infinite number); therefore the fraction of gas flow rate passing through each annulus is 0.005. The curved line shows an example of an actual distribution, which shows higher fraction of gas flow rate at the center than towards the wall of the cell. The intersection of these two lines determines a radial distance ($\varphi = 0.71$) that indicates where to measure the average J_g in the cell.

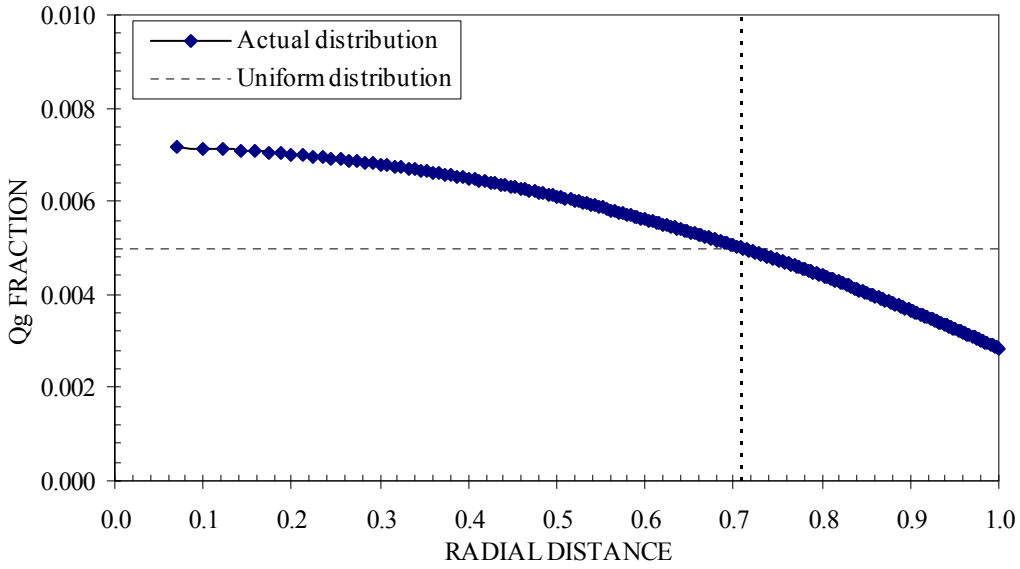

Figure 4. 5 Gas flow rate vs. radial distance

Determination of this radial distance can also be achieved by solving Equation (4. 7) for φ when $Q_{g(fraction)}$ equals 1/n, i.e., average gas flow rate for n annular regions of equal area,

$$\frac{2\cdot\beta\cdot\left(\varphi_2^2-\varphi_1^2\right)-\alpha\cdot\left(\varphi_2^4-\varphi_1^4\right)}{2\cdot\beta-\alpha}=\frac{1}{n} \tag{4. 14}$$

It is convenient to express φ_2 as a function of φ_1,

$$\varphi_2=\sqrt{\frac{1}{n}+\varphi_1^2} \tag{4. 15}$$

where substituting Equation (4. 15) into Equation (4. 14) and rearranging gives,

$$2\cdot\beta\cdot\left[\left(\frac{1}{n}+\varphi_1^2\right)-\varphi_1^2\right]-\alpha\cdot\left[\left(\frac{1}{n}+\varphi_1^2\right)^2-\varphi_1^4\right]=\frac{1}{n}\cdot\left(2\cdot\beta-\alpha\right) \tag{4. 16}$$

Solving Equation (4. 16) for r_1 gives,

$$\varphi_1=\sqrt{0.5\cdot\left(1-\frac{1}{n}\right)} \tag{4. 17}$$

and substituting Equation (4. 17) into Equation (4. 15) gives,

$$\varphi_2=\sqrt{0.5\cdot\left(1+\frac{1}{n}\right)} \tag{4. 18}$$

Dividing the total area into an infinite number of annuli of equal area is equivalent to taking the limit when n tends to infinity. Under this condition φ_1 equals φ_2 thus,

$$\lim_{n\to\infty}\sqrt{0.5\cdot\left(1-\frac{1}{n}\right)}=\lim_{n\to\infty}\sqrt{0.5\cdot\left(1+\frac{1}{n}\right)}=0.71 \tag{4. 19}$$

Equation (4. 19) gives the same the radial distance as found graphically and means that this intersection point is common for any parabolic gas distribution and locates the radial distance to measure $J_{g(av)}$. This argument can be further demonstrated by dividing the total gas flow rate (Equation (4. 4) integrated from $r_1 = 0$ to $r_2 = R$) by the cell cross-sectional area, $\pi \cdot R^2$,

$$J_{g(av)} = \frac{\pi \cdot \beta \cdot R^2 - \frac{\pi \cdot \alpha}{2} \cdot R^4}{\pi \cdot R^2} \tag{4. 20}$$

with the solution,

$$J_{g(av)} = \beta - 0.5 \cdot R^2 \cdot \alpha \tag{4. 21}$$

Comparison of Equation (4. 21) with Equation (4. 1) shows that,

$$r^2 = 0.5 \cdot R^2 \tag{4. 22}$$

and expressing as a function of the dimensionless radial distance,

$$\varphi = \frac{r}{R} = \sqrt{0.5} = 0.71 \tag{4. 23}$$

Equation (4. 23) confirms that $J_{g(av)}$ is found at the radial position $\varphi = 0.71$ and that this is valid for any parabolic gas distribution. It is important to note that this radial distance by itself does not give information about the quality of the air distribution; it only identifies the correct sampling point to measure the average J_g in a cell which may find use, for instance, when single point comparison of cells is made.

CHAPTER 5

RESULTS: SUPERFICIAL GAS VELOCITY

5.1 - Introduction

Experimental results from laboratory and plant regarding the two gas velocity measurement techniques are presented in this chapter. The difference in J_g using the on-off and continuous technique is examined.

5.2. – Laboratory tests

5.2.1 – Calibration of mass flow meters

The flow meters used are MKS mass flow controllers/transmitters of ranges: 0-5 LPM, 0-20 LPM, 0-30 LPM and 0-400 LPM. Figure 5. 1 shows the set-up used to calibrate the mass flow meters. The set-up comprises a graduated 15.24 cm diameter plastic column sealed at the top with connections to a pressure transmitter, temperature sensor, a relief ball valve and to an air source. The column is connected hydraulically at the bottom to a 5.08 cm diameter pipe opened at the top having a discharge to an electronic scale. The calibration procedure starts by setting the desire Q_g set-point. The valve remains open until the air flow reaches the steady state value. At this point the valve is closed; the air accumulates inside the column, displacing the water that exits through the top of the parallel pipe. The water collected is recorded by the electronic scale and the weight used to determine the volumetric flow rate of air (assuming water density of 1 g/cm^3). The pressure and temperature are recorded as well to report the air flow rate at standard conditions (0° C, 1 atm). The data for the calibration of the mass

flow meters is presented in Appendix A. Figure 5. 2 to Figure 5. 5 show the calibration curves for the mass flow meters used in the laboratory.

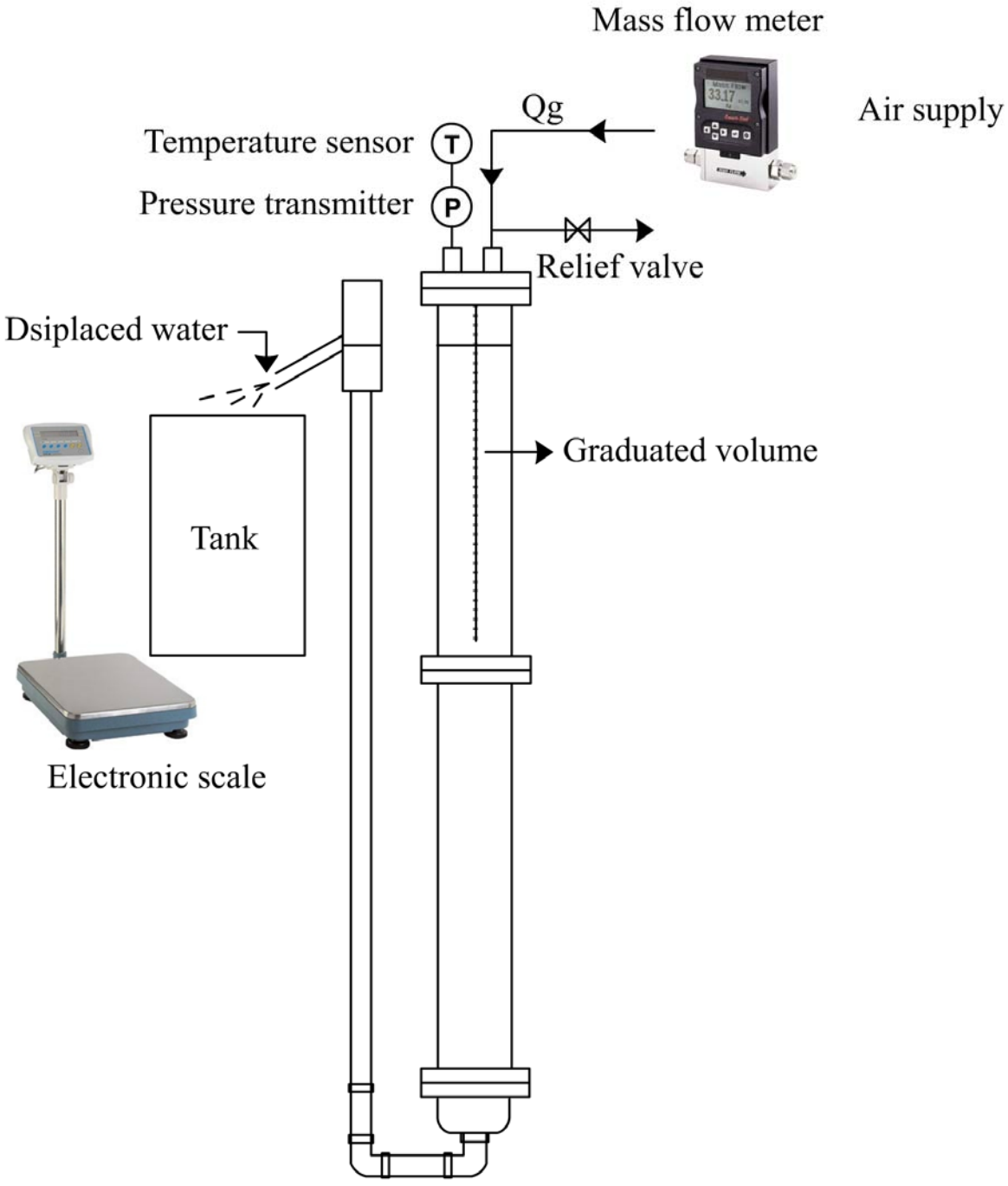

Figure 5. 1 Mass flow meter calibration set-up

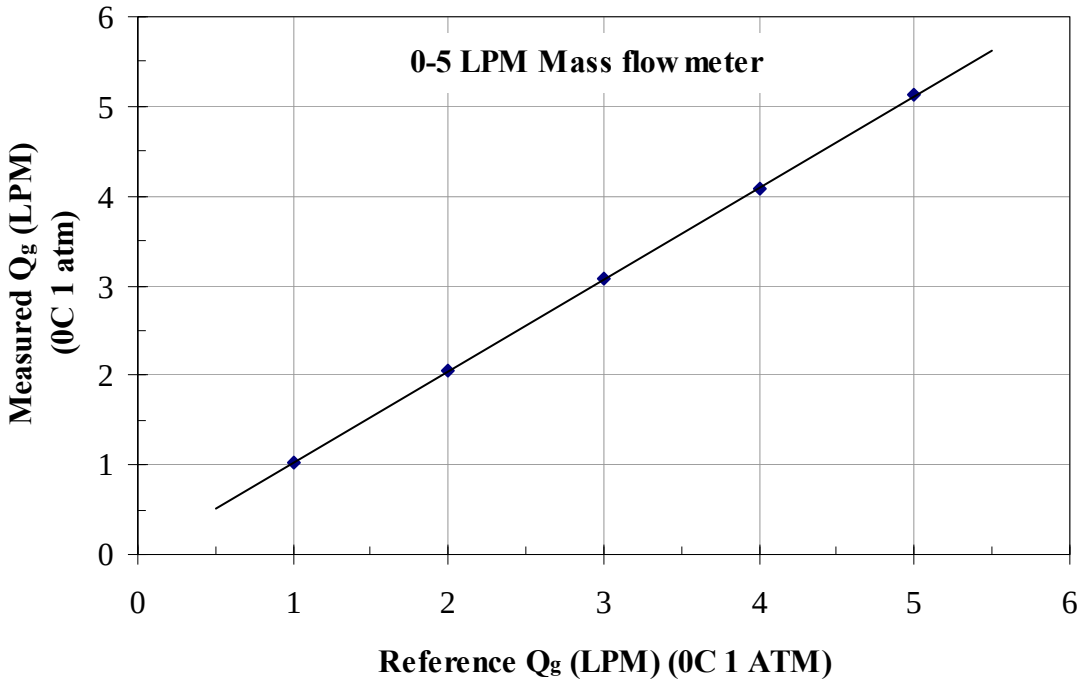

Figure 5. 2 Calibration 5 LPM mass flow meter

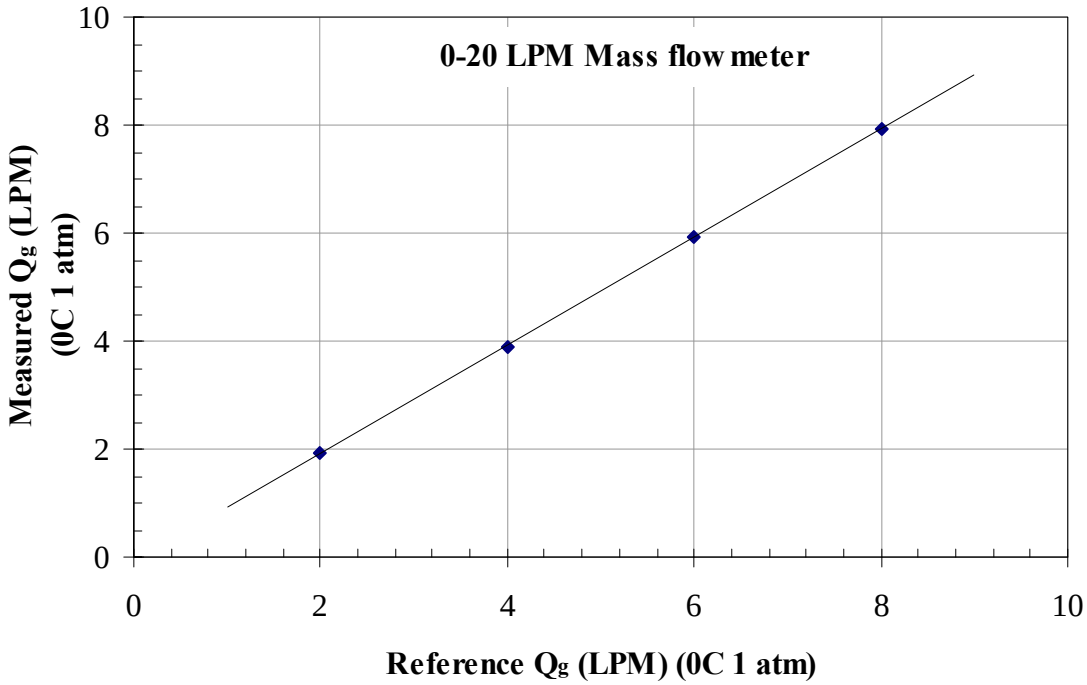

Figure 5. 3 Calibration for the 20 LPM mass flow meter

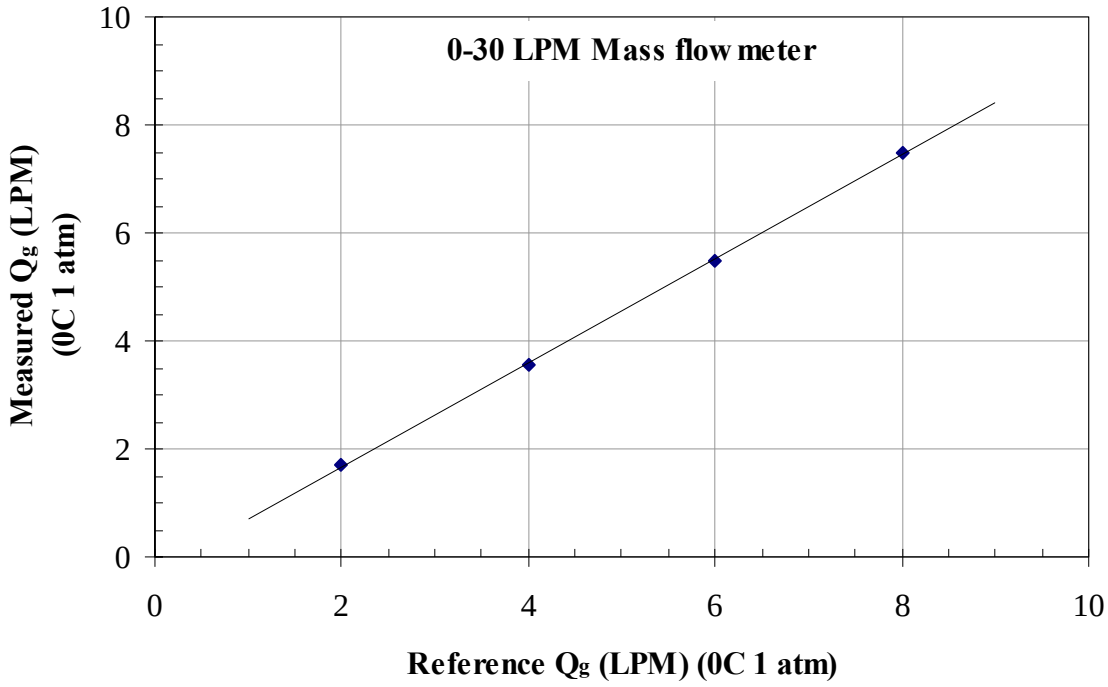

Figure 5. 4 Calibration for the 30 LPM mass flow meter

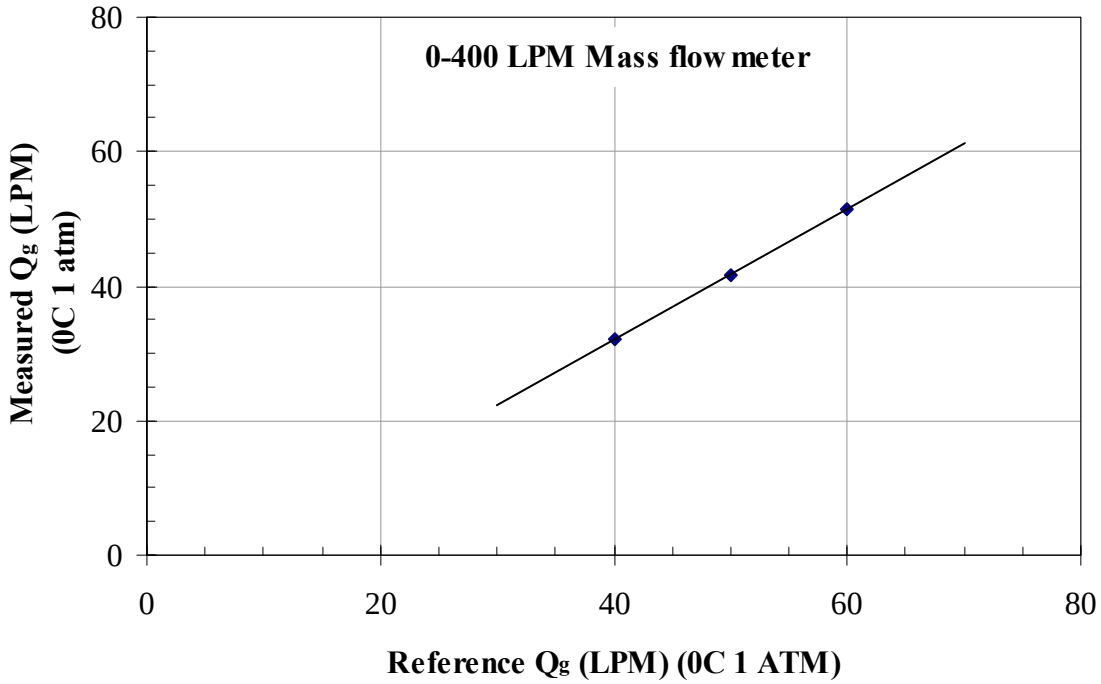

Figure 5. 5 Calibration for the 400 LPM mass flow meter

5.2.2 - Calibration of pressure transmitters

The pressure transmitters used in the experiments were Wika model S-10 in the ranges 0-127 cmH2O and 0-1054 cmH2O. Figure 5. 6 and Figure 5. 7 show the calibration curves; and the data are presented in Table A. 2 in Appendix A. The calibration procedure consisted in comparing the pressure signal with hydrostatic pressure given by a known height of water in the 15.24 cm diameter column.

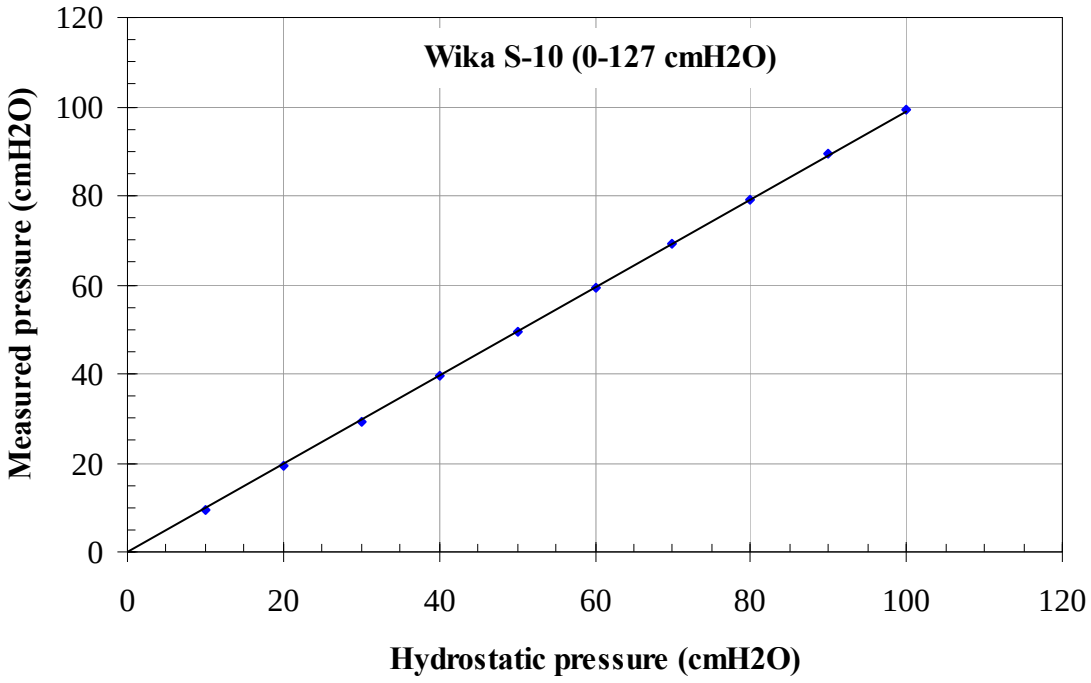

Figure 5. 6 Pressure transmitter calibration (range 0-127 cmH_2O)

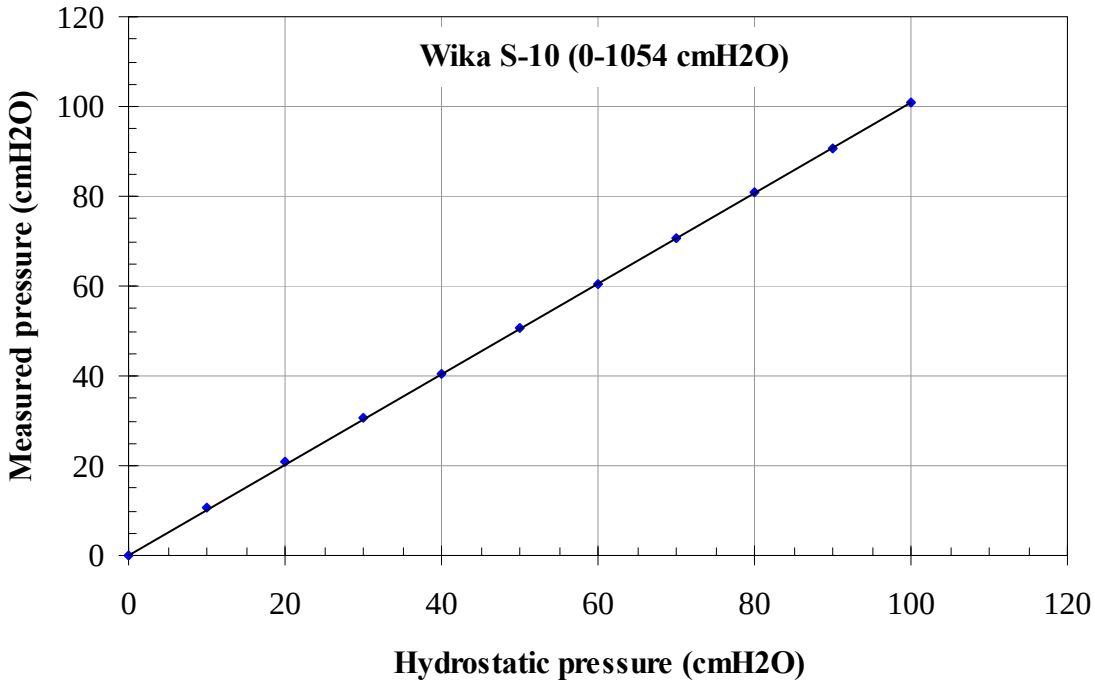

Figure 5. 7 Pressure transmitter calibration (range 0-1054 cmH2O)

5.2.3 – Calibration of orifices for continuous J_g sensor

Fundamental aspects of flow thorough an orifice are given in Appendix B. The orifices are made of a cylindrical piece of plastic (3 cm in length), machined at one end to fit a ½" NPT thread (Figure 5. 8, above). The orifice nominal diameter (d) identifies each orifice. A set-up was designed to calibrate up to 4 orifices (Figure 5. 8). The set-up comprised a plastic pipe with several ports, having one port connected to the air flow, one to a temperature transmitter and one other to a pressure transducer. Each orifice is connected to a ball valve to isolate them from each other. The calibration procedure consisted in introducing a known air flow rate. The pressure and temperature are measured as the air exits through the orifice. Data are collected until steady state is reached (ca. 3 minutes).

Figure 5. 9 shows the calibration curves for the orifices used. The diameters of the orifices were chosen to cover the practical range of gas velocity introduced in Chapter 1 (0.5 to 2.5 cm/s). The results of the calibrations are presented in Appendix A.

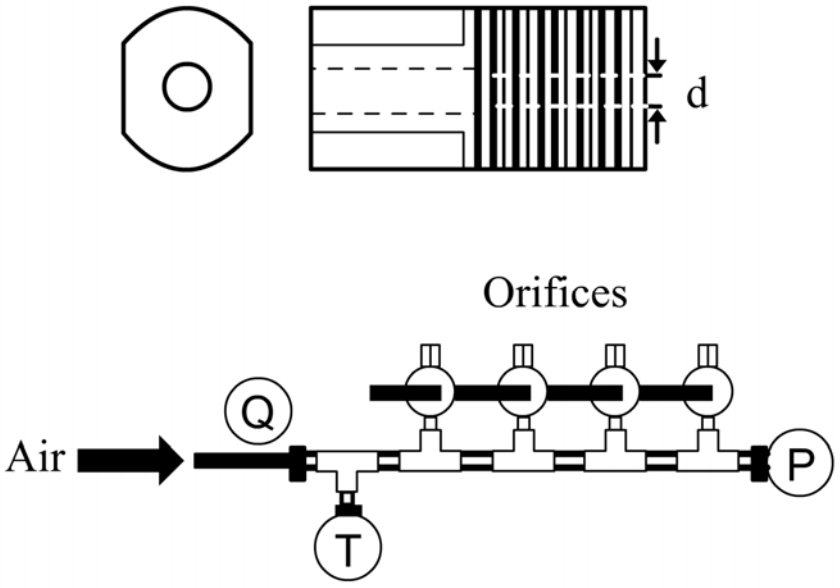

Figure 5. 8 Illustration of orifice (above) and calibration set-up (below)

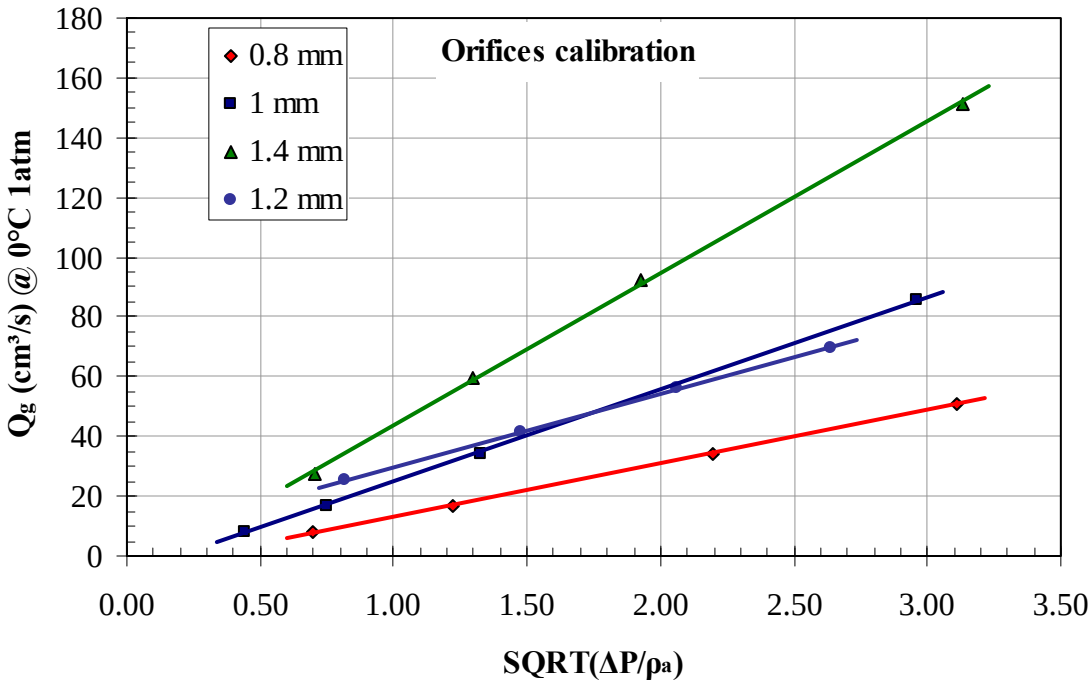

Figure 5. 9 Orifice calibration curves

5.2.4 – Comparison between continuous and on-off J_g technique

To confirm that the on-off model for water (Equation 3. 19) gives the same results as the continuous version, a sensor designed to operate in either mode was installed in a 50 cm diameter column. Two tests were carried out; The first involved introducing a known air flow rate directly into the sensor to measure gas velocity (Figure 5. 10). This avoids issues surrounding collecting bubbles. Figure 5. 11 shows good agreement between the two modes of operation, with perhaps a trend to deviate as reference J_g exceeds ca. 2 cm/s.

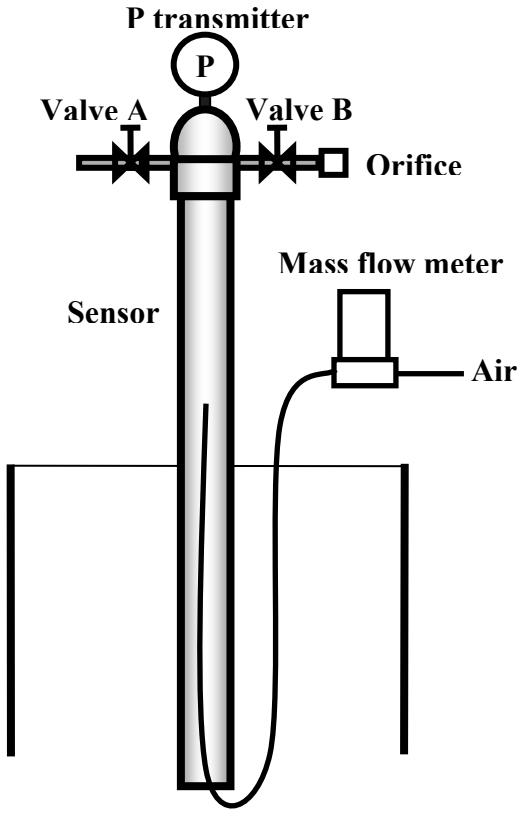

Figure 5. 10 Illustration of the test to confirm continuous and on-off technique; air fed directly to the sensor

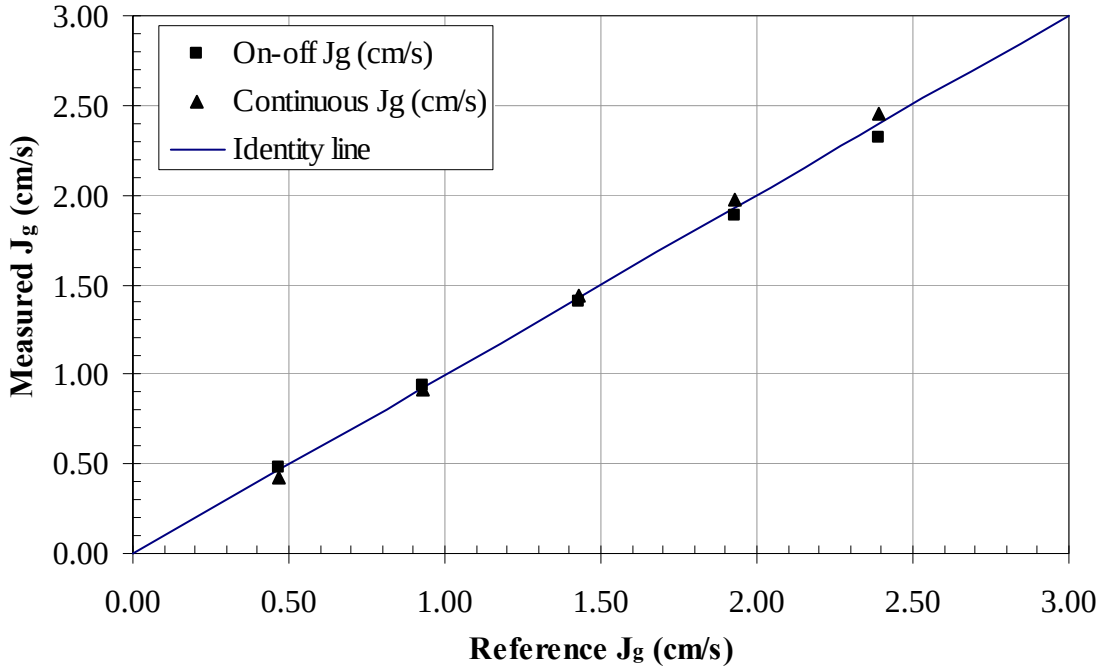

Figure 5. 11 Test 1: Comparison between on-off and continuos mode

The second test involved collecting bubbles and used an air-frother solution. Figure 5. 12 shows the set-up with frother solution being introduced into the column from a reservoir using a peristaltic pump. The air was supplied through a mass flow meter from the bottom and dispersed into bubbles by a porous metal sparger. The overflow was returned to the system via the reservoir tank. The frother used was 1-pentanol, selected because it was desired to have minimum froth formation. The frother concentration was 80 ppm, being above the critical coalescence concentration (CCC ca. 35 ppm, Finch et al., 2008) to ensure bubbles as small as possible. Figure 5. 13 shows that the results operating the J_g sensor in continuous and on-off mode are in excellent agreement. A consistent deviation above the reference J_g is noted possibly caused by a parabolic gas velocity profile inside the column giving higher gas rates near the centre.

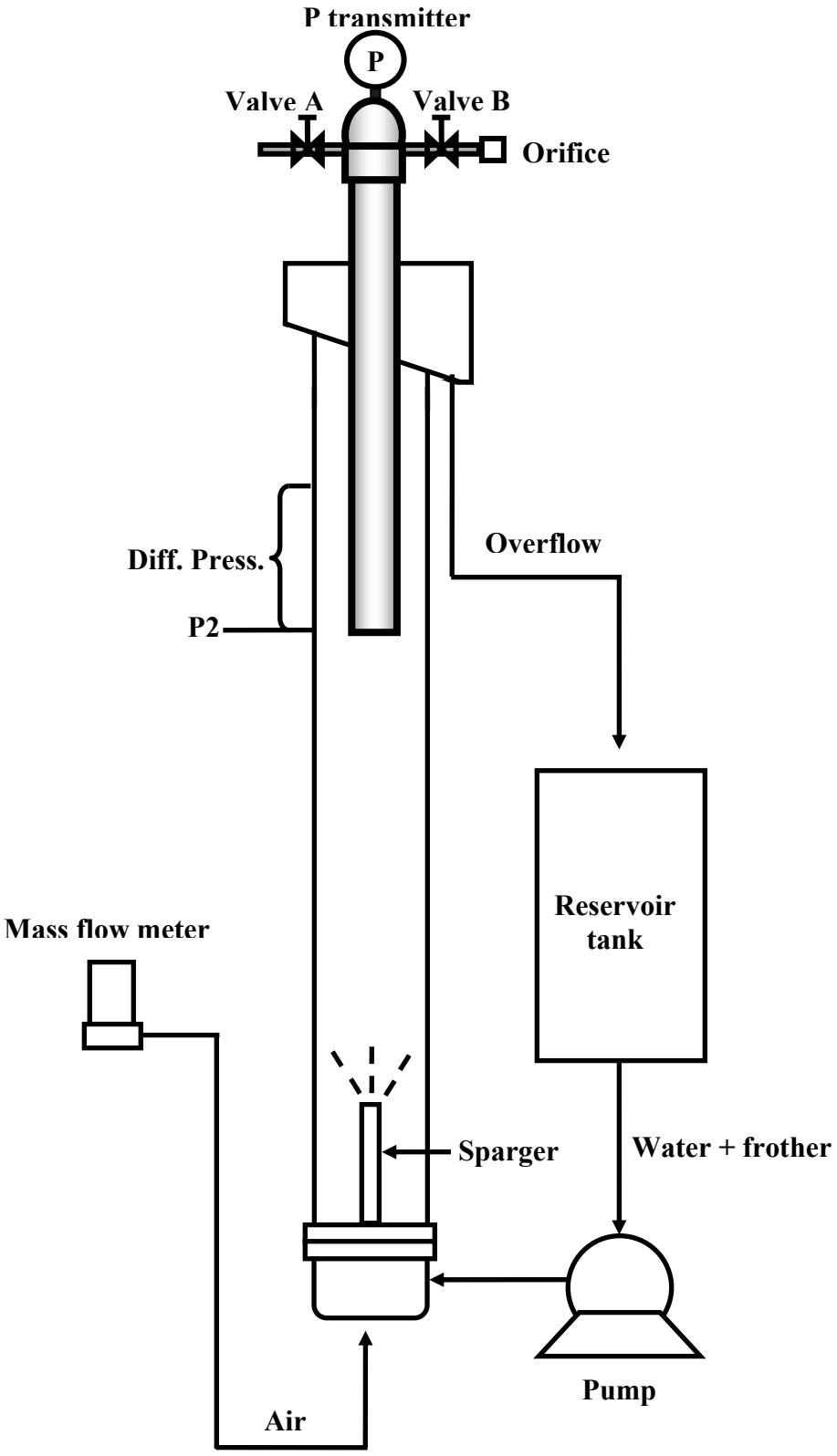

Figure 5. 12 Laboratory set-up

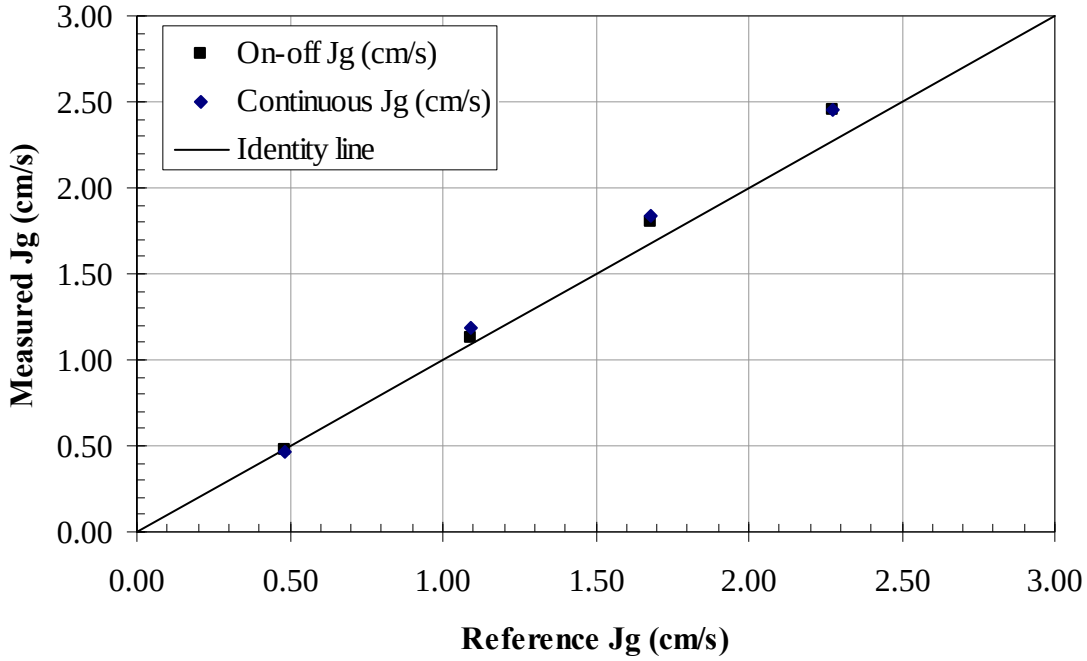

Figure 5. 13 Test 2: Comparison between continuous and on-off methods (sampling bubbles)

5.3. – Plant experiences

Two plant trials comparing the continuous and on-off method were undertaken, one at Troilus located in northern Quebec and the other one at Salvador located in northern Chile.

5.3.1 - Troilus

Troilus is a gold/copper mine 120 km north of Chibougamau, Quebec, operated by Inmet Mining Corp. Construction of the open pit mine commenced in 1994 with production starting by 1997. The average throughput is 18 500 metric tons per day.

The test cell was a circular cross-section column 4 m in diameter and 10 m high ahead of a rougher bank of seven GL&V/Dorr Oliver DO – 1550 UT cells. Figure 5. 14 is a top view of the sensor installation and Figure 5. 15 shows the side view with sensor

dimensions. The two sensors were installed one beside the other to try to minimize differences due to variations in air across the cell. The tubes were 10.16 cm diameter by 250 cm high and were installed 114 cm below the column lip. The pressure signals were collected with Wika S-10 pressure transducers in the range 0-127 cmH_2O. The pressure transducers were connected to a Dutec® data acquisition device and the signal was collected with GE Fanuc iFix 4.0. The software stores the data for off-line analysis.

Figure 5. 16 shows examples of the three pressure signals collected. It is evident that the system was stable during the tests. The sampling period was ca. 55 minutes. The start of sampling for the on-off mode was when the continuous signal reached a steady value.

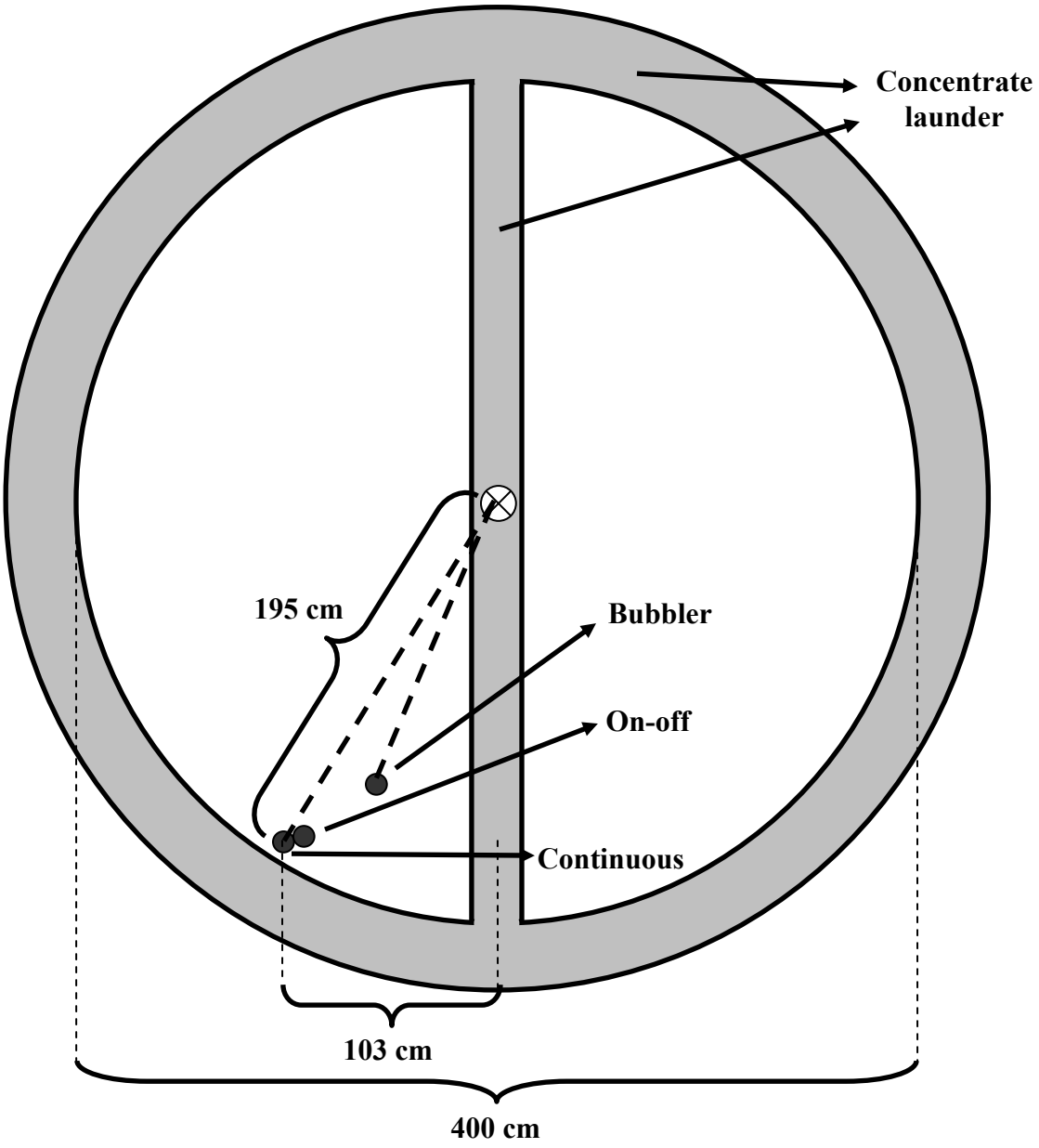

Figure 5. 14 Top view of the J_g sensor installation at Troilus

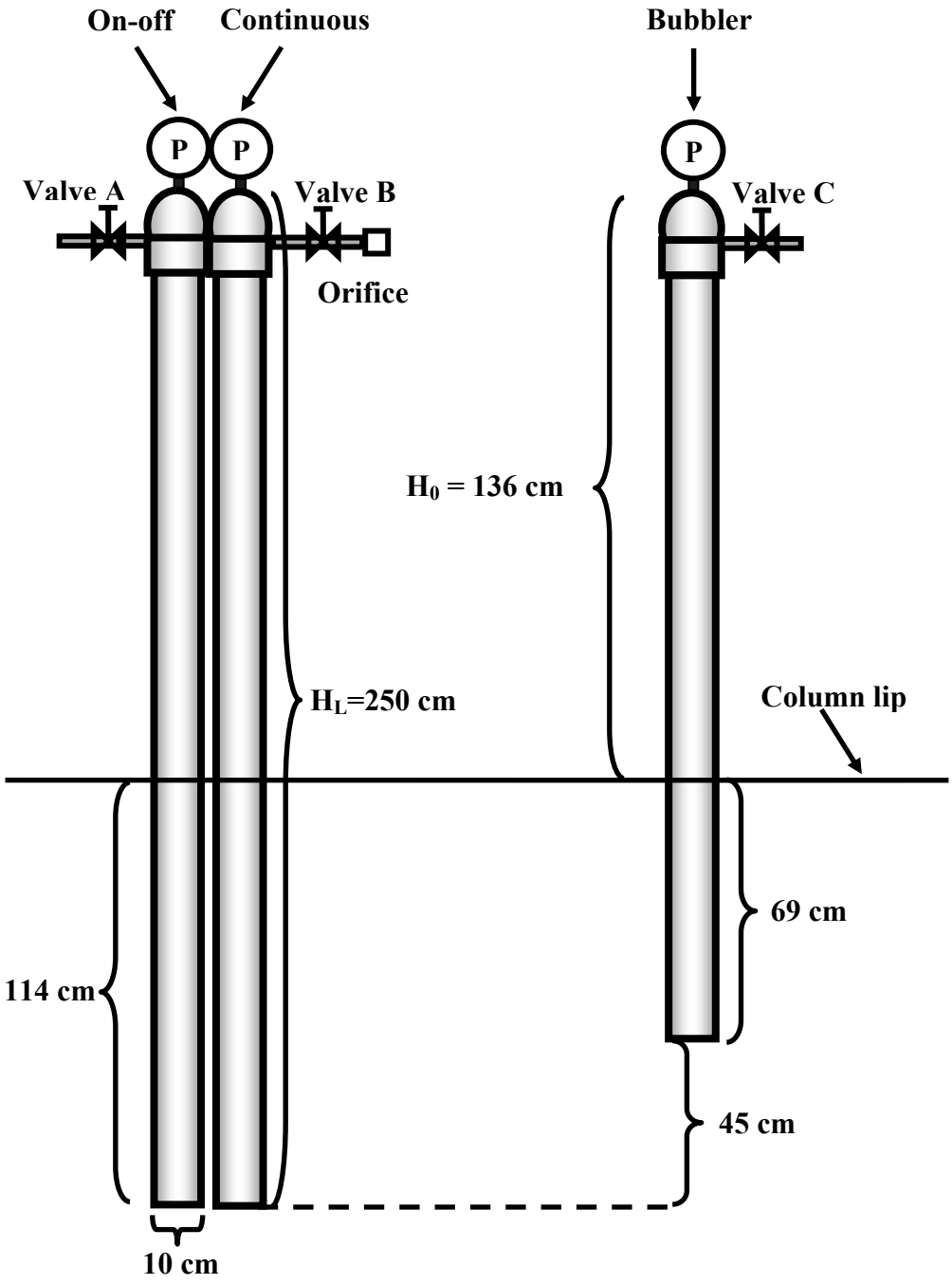

Figure 5. 15 Side view of the J_g sensor installation at Troilus

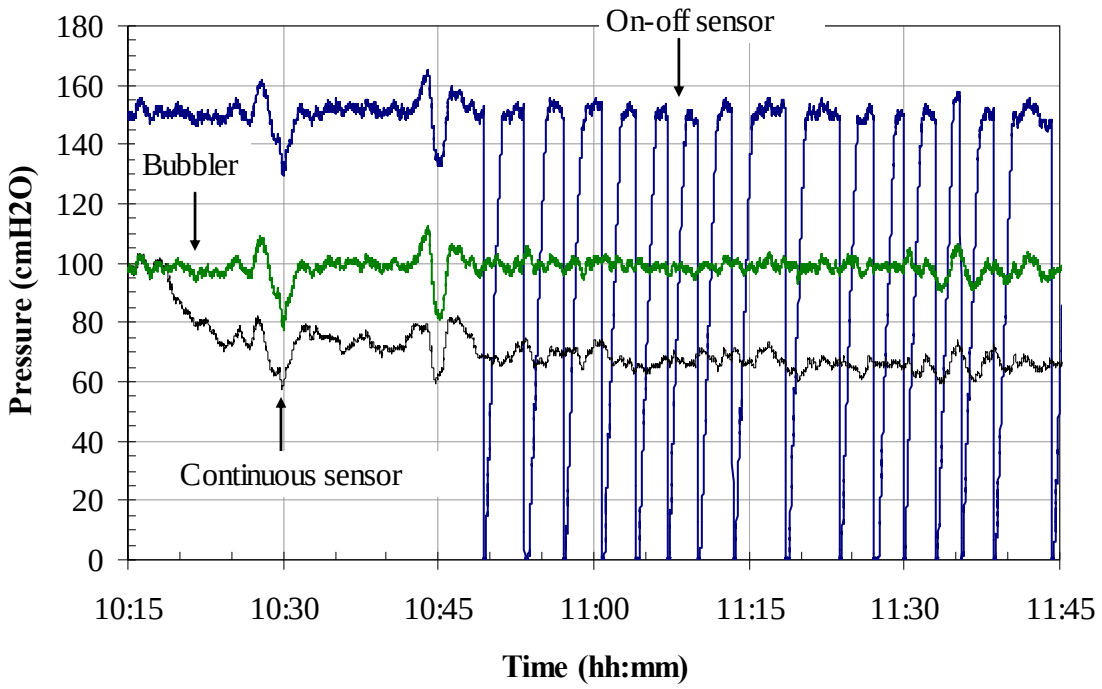

Figure 5. 16 Pressure versus time curves of comparison between on-off and continuous method at Troilus

Figure 5. 17 shows the results of the comparison between the continuous and the two solutions for the on-off method (i.e., Equation 3. 19 and Equation 3. 36). It can be seen that for all cases the signal given by the continuous technique is higher than the on-off using the original Equation 3.19 giving a consistent bias of ca. 16%. In contrast, the values given by the corrected Equation 3.36 are closer to the continuous method, the difference (error) between the two methods being decreased to ca. 4%. These results support the contention that a difference in density of the aerated slurry inside and outside the tube is responsible for the deviation between the continuous and on-off modes. The estimate of aerated slurry density used in deriving Equation 3.36 appears to coincide with this particular case but independent assessment is required.

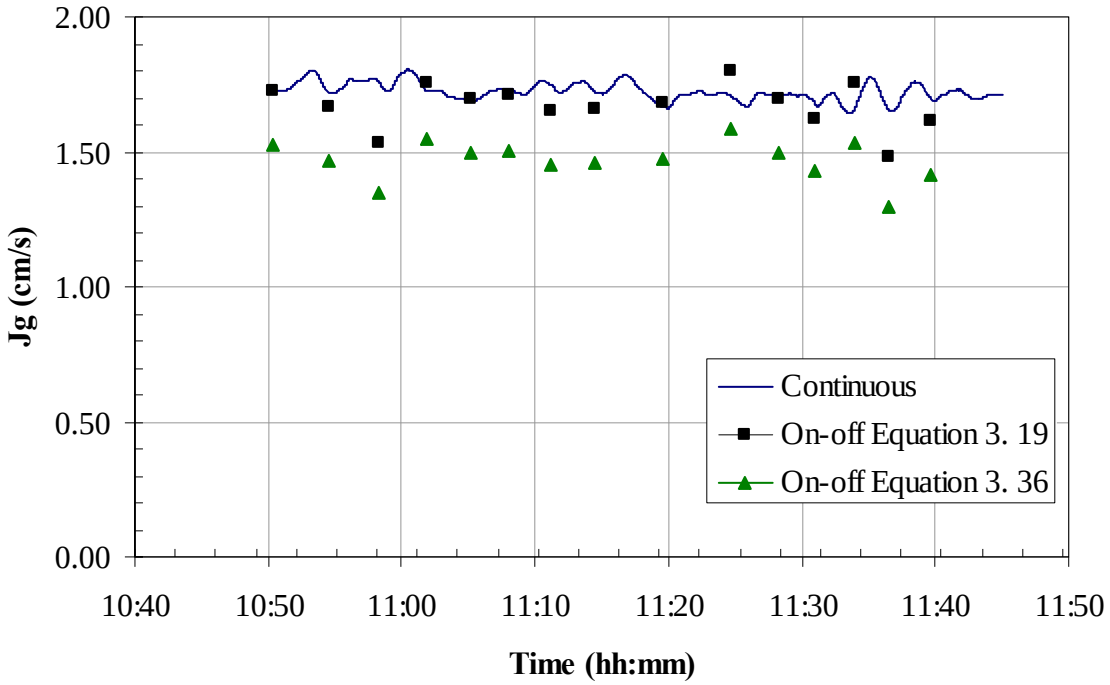

Figure 5. 17 Results of comparison between on-off and continuous J_g at Troilus

5.3.2 - Salvador

The other set of data was collected at the Salvador concentrator, located in Chile in the Andes Mountain region, 1100 km north of the capital city, Santiago. Salvador is operated by Codelco and exploits oxide and sulphide ores producing ca. 64 000 metric tons of copper cathode a year along with 1200 metric tons of molybdenum concentrate.

Figure 5. 18 and Figure 5. 19 show the top and side view, respectively, of the J_g sensor installation. In this case, the same tube was used to measured gas velocity by the two methods, assuring the same sampling point for both. Figure 5. 20 illustrates the pressure vs. time curves that show the sensor was first set in continuous mode and after a steady state of 10 minutes (from 17:10 to 17:20) was converted to on-off mode. The

signal given by the “bubbler” tube confirms that there were no changes influencing hydrostatic pressure (i.e., no level variations or changes in air supply to the cell).

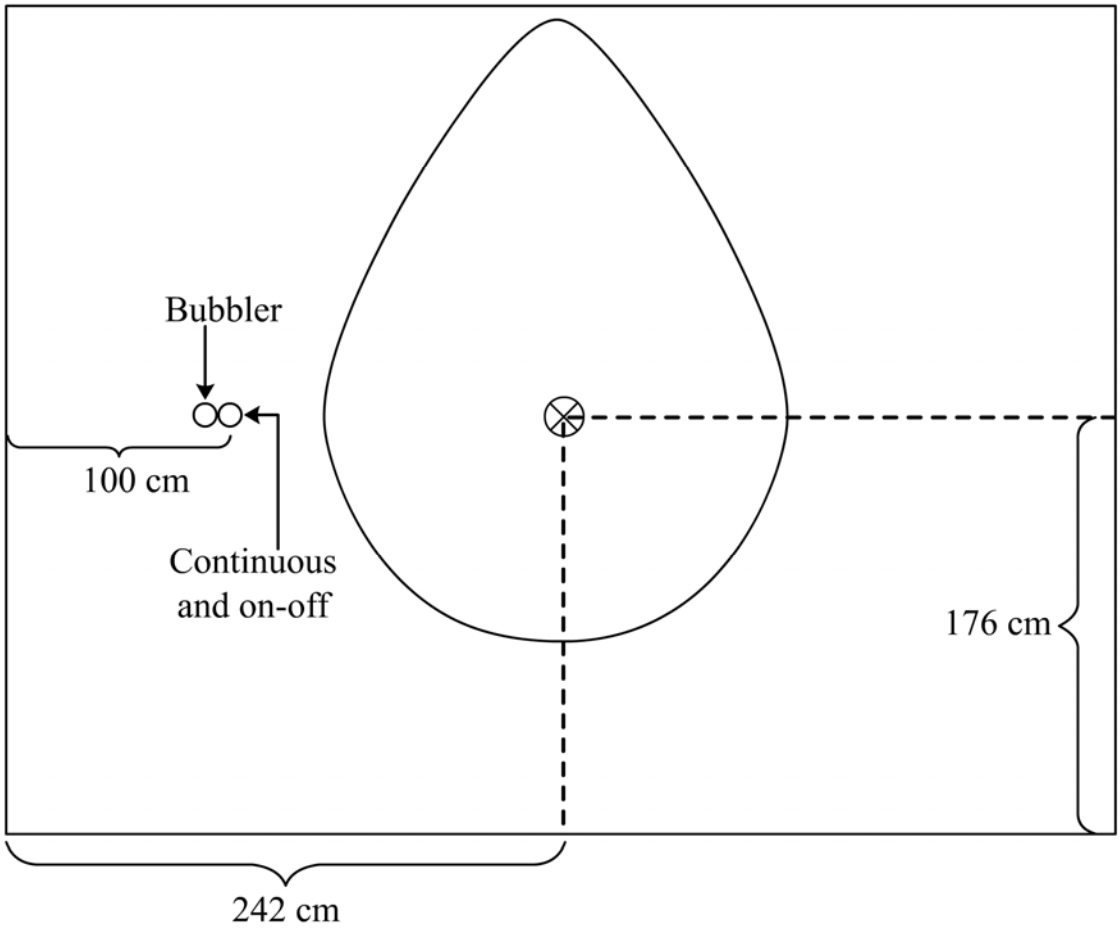

Figure 5. 18 Top view of the J_g sensor installation at Salvador

The comparison in Figure 5. 21 shows that the continuous technique gives a higher J_g than the on-off. The true (i.e., continuous) J_g is ca 1.5 cm/s; the on-off using Equation 3. 19 gives values nearly 30% lower (ca. 1.1 cm/s) and using Equation 3. 36 this closes to ca. 10% (ca. 1.3 cm/s), i.e., supporting once more that the error lies in the aerated slurry density inside the sensor being lower than that outside. In this case, however, the estimate of the aerated slurry density in the sensor is not correct as a ca.

10% error remains. It is not clear yet how to measure the slurry density in the sensor to provide the independent proof.

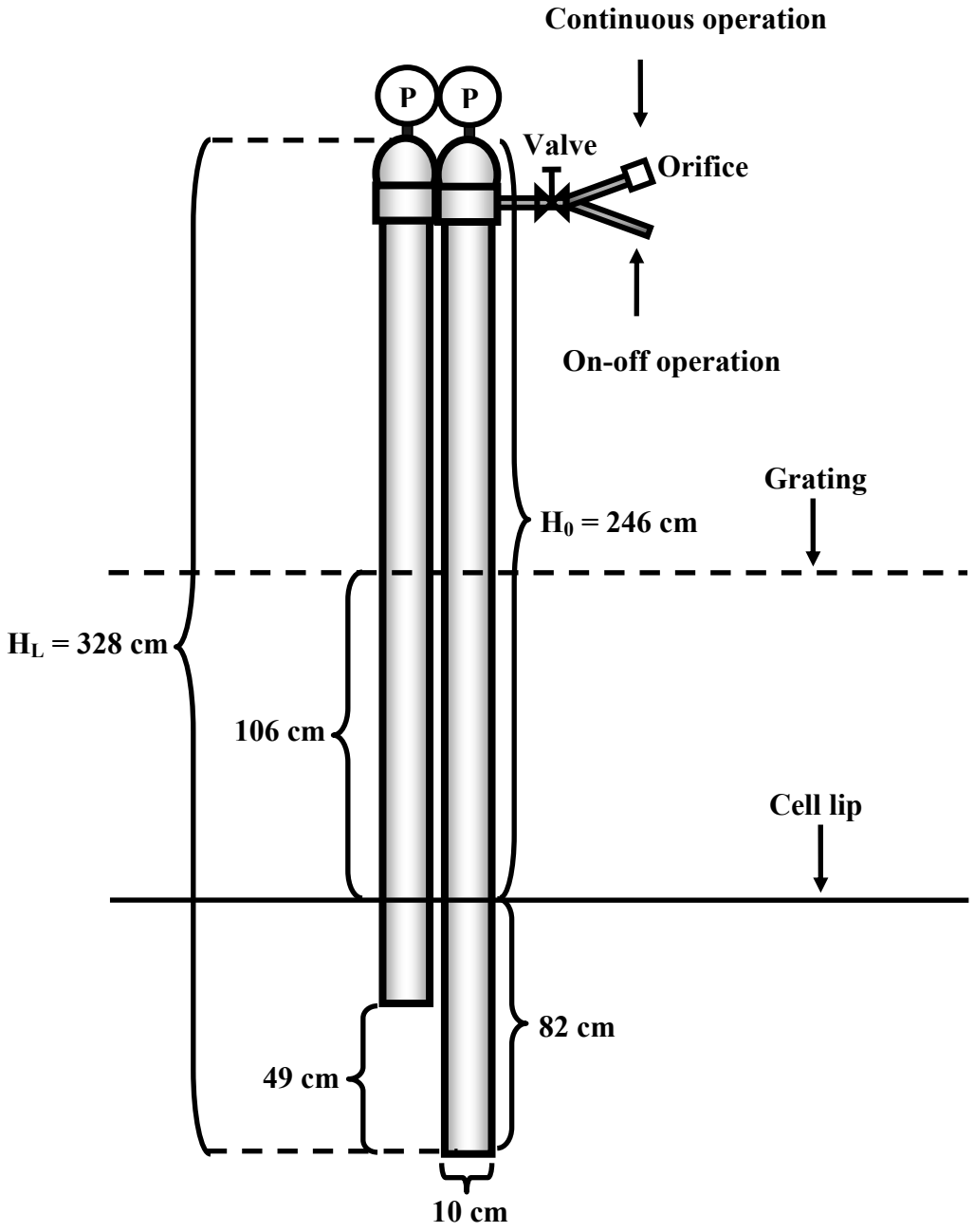

Figure 5. 19 Side view of the J_g sensor installation at Salvador

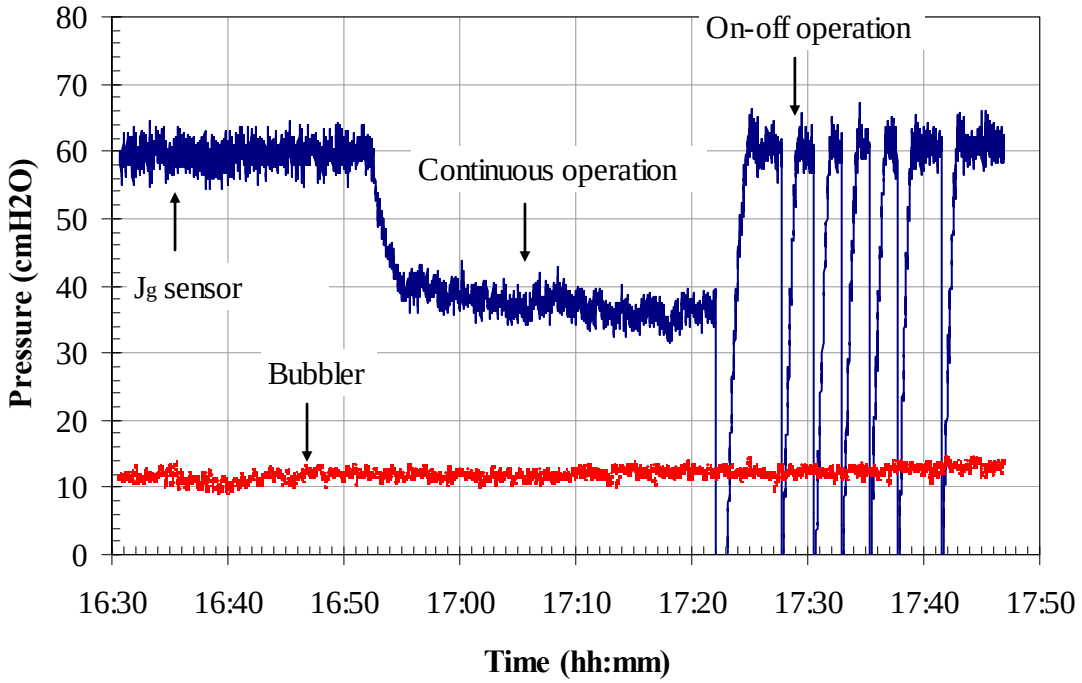

Figure 5. 20 Pressure versus time curves of comparison between on-off and continuous method at Salvador

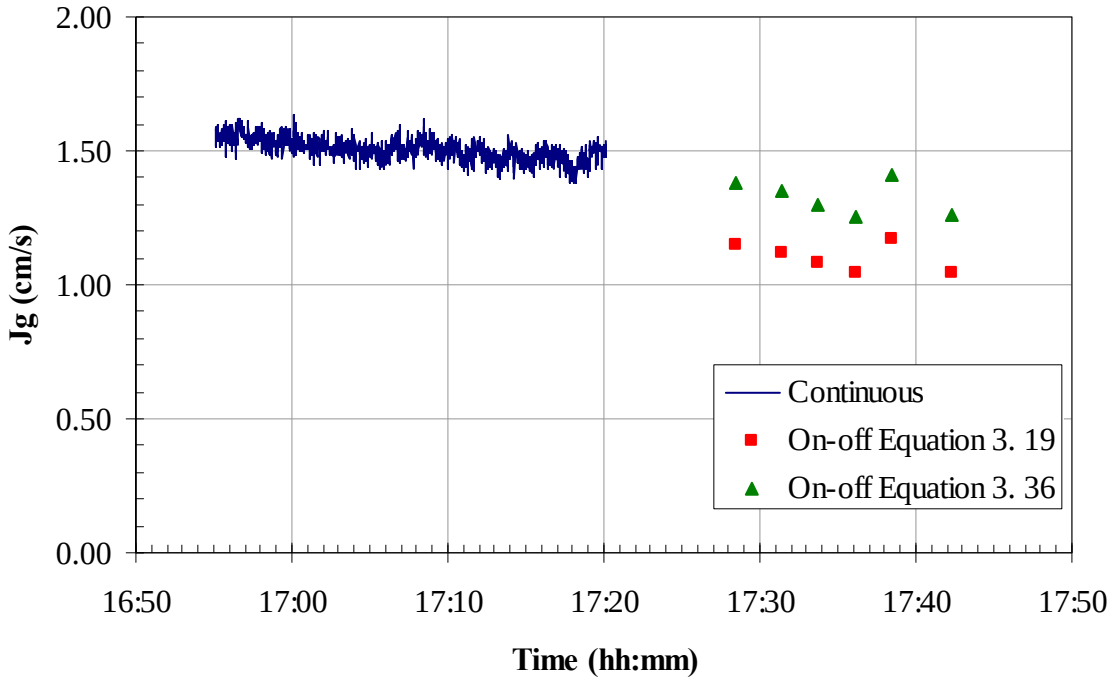

Figure 5. 21 Results of comparison between on-off and continuous J_g at Salvador

CHAPTER 6

RESULTS: GAS DISTRIBUTION

6.1 – Introduction

In this chapter experimental results of cell gas velocity profiles and distribution deviation index obtained from laboratory and plant are presented.

6.2 – Laboratory tests

Gas velocity mapping was performed in a Metso model 0800 mechanical cell, 113 cm diameter and 123 cm high. The flotation cell is connected to an ABB frequency variator model ACS400. Figure 6. 1 shows the set-up used. The feed to the cell was supplied from the reservoir by a centrifugal pump and the overflow was recirculated. To have minimum froth depth and fine bubble size, the selected frother was 1-pentanol at a concentration of 80 ppm.

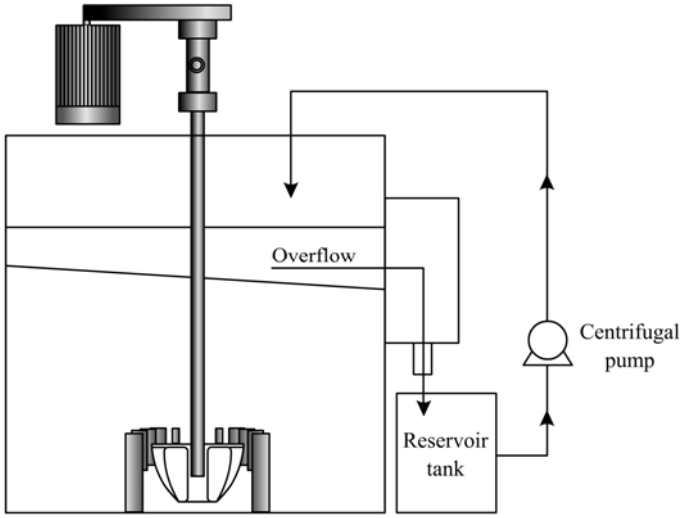

Figure 6. 1 **M**easurement set-up for Metso cell

Five gas velocity sensors of 7.62 cm diameter and 87 cm high were installed at different radial positions. Figure 6. 2 and Figure 6. 3 show the top view and side view, respectively, and Figure 6. 4 is a picture of the set-up. The sensors were installed as close to the impeller shaft and to the wall as possible. This particular flotation cell has a circular baffle 43 cm from the tank bottom that dictated how close to the wall cell the sensor installation could be.

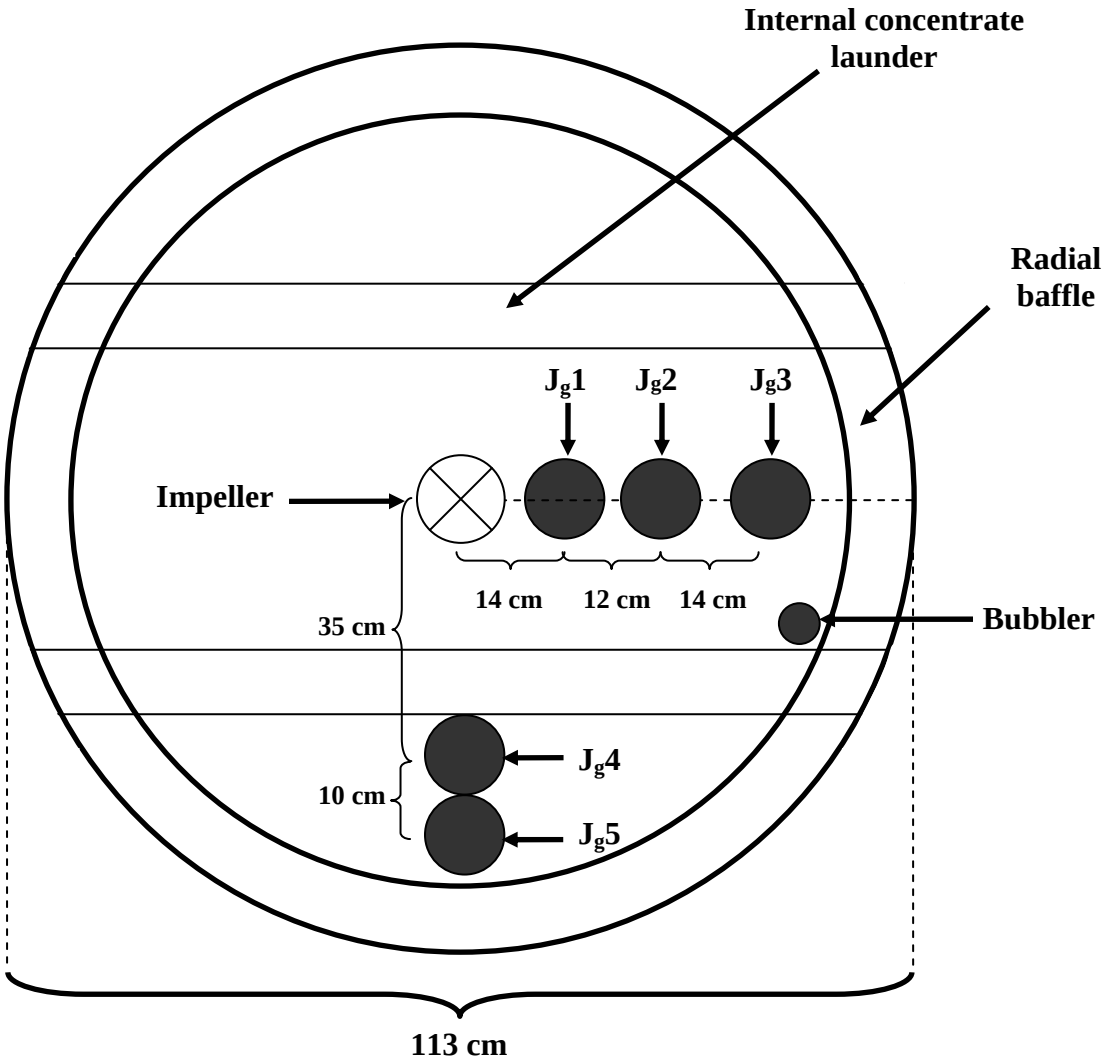

Figure 6. 2 Top view of the J_g sensor installation in Metso 0800 cell

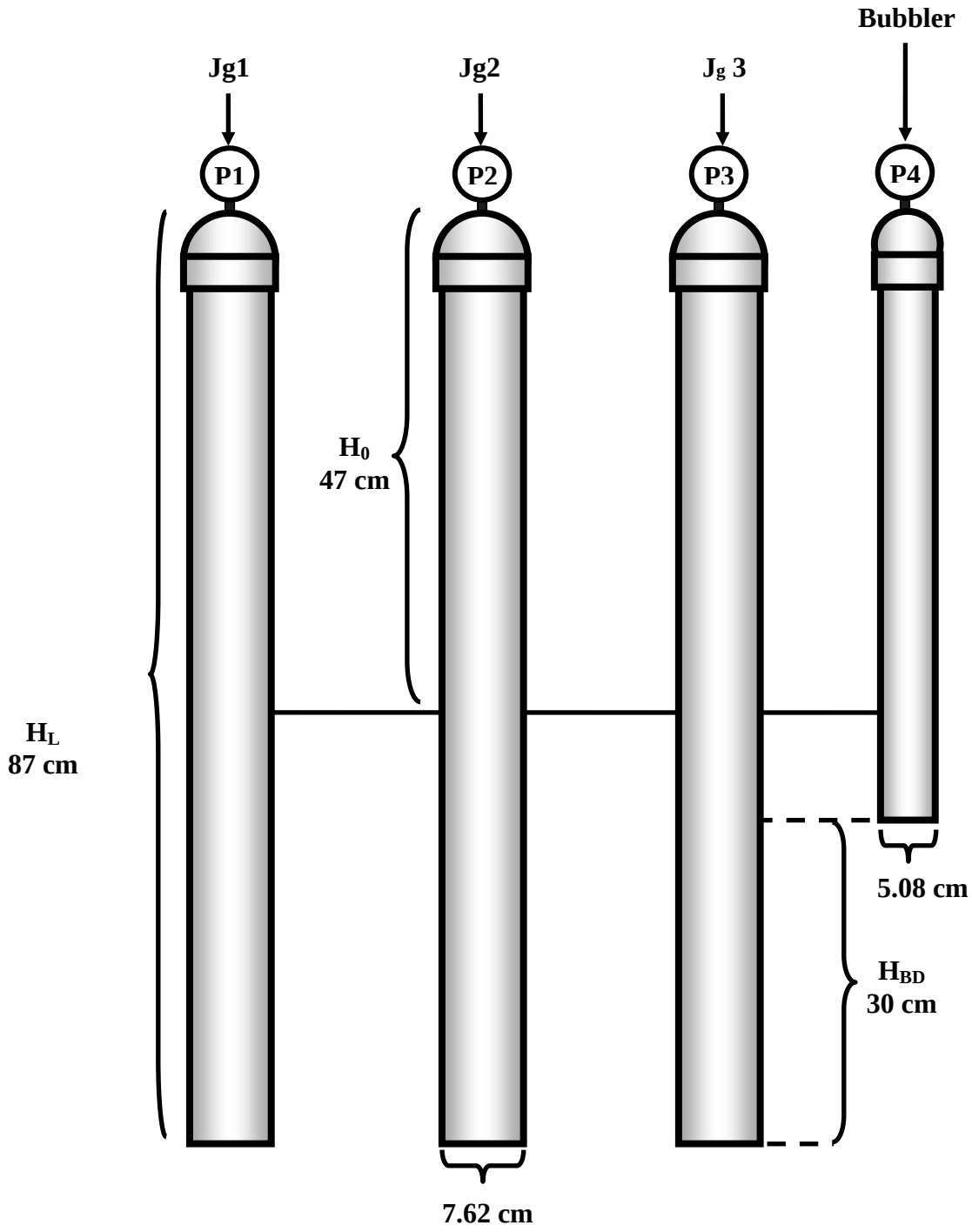

Figure 6. 3 Side view of the J_g sensor installation in Metso 0800 cell

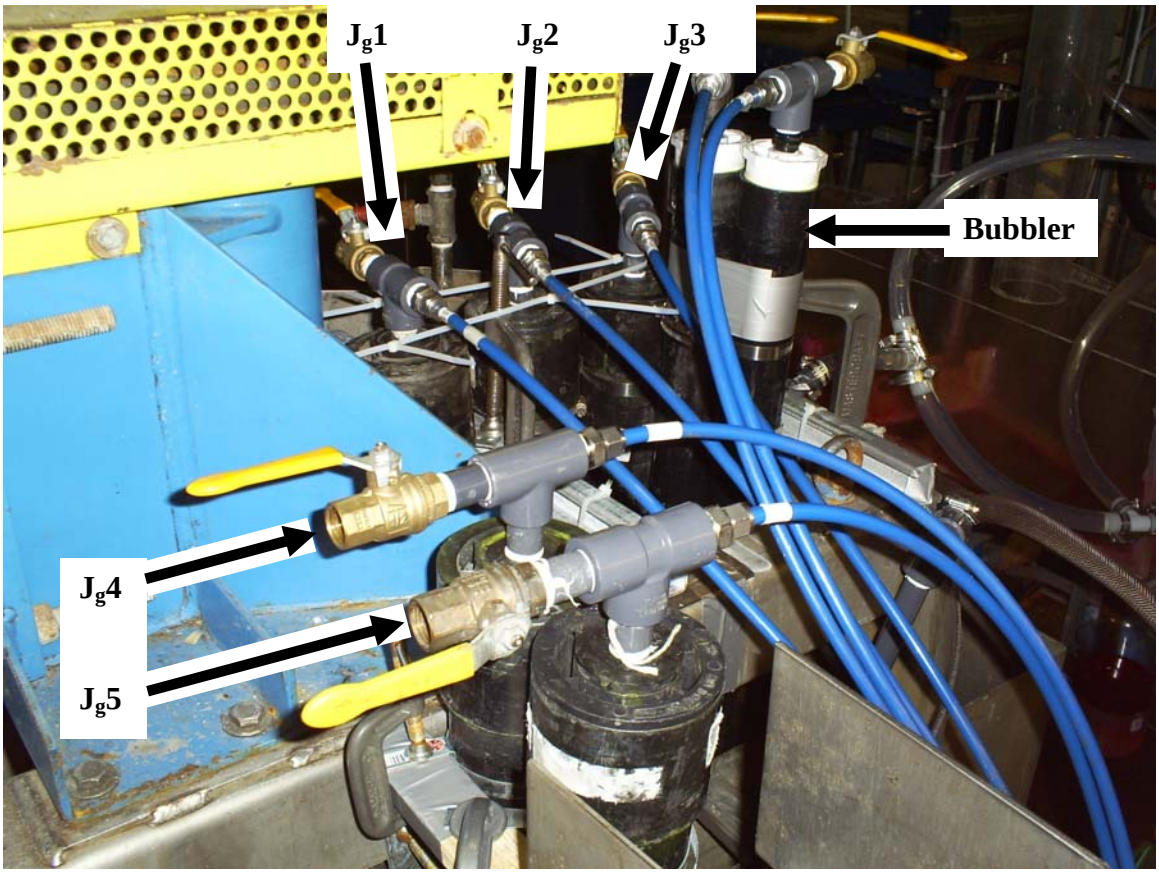

Figure 6. 4 Picture of the installation in the laboratory

The gas velocity profile was measured for two levels of impeller speed (718 and 1786 RPM) and two levels of air flow rate (13 and 25 m^3/h). Figure 6. 5 shows gas the profiles obtained for the two levels of air flow rate at the low impeller speed. At low air rate the impeller is able to distribute the air. The result is close to the parabolic profile that has been assumed. Note by extrapolation of the parabola that there appears to be no air reaching the wall of the cell.

In contrast, at the high level of air flow, the parabolic profile is not obtained, the air almost directly exiting the cell through the central area; the combination of low

impeller speed and high air rate does not provide the necessary energy per unit volume of air to distribute the bubbles. The curve drawn represents an intuitive combination of two regions: one parabolic towards the wall and another with a sudden increase in J_g towards the centre. During the test, turbulence was observed around the impeller shaft, the air appearing in "slugs", disturbing the surface of the cell significantly.

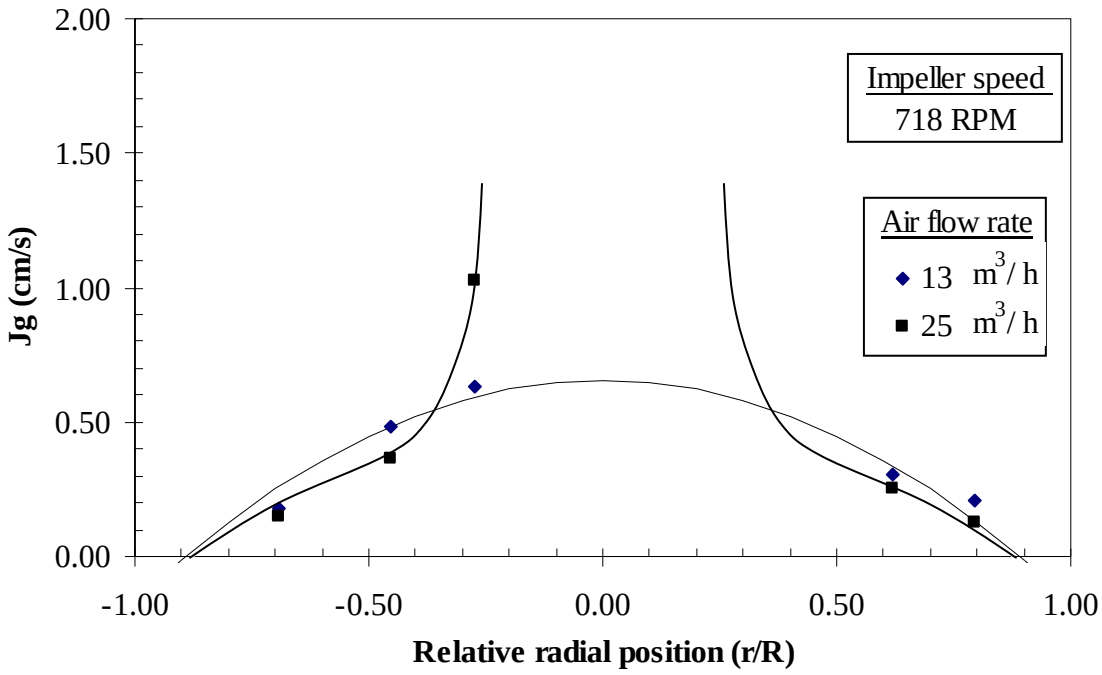

Figure 6. 5 Gas velocity profiles obtained for two levels of air flow rate at low impeller speed

Gas distribution is significantly improved when the system is operated at high impeller speed (Figure 6. 6). The profiles for the two air rates were effectively uniform, i.e., an ideal distribution. This is arguably the best condition to collect mineral particles, i.e., bubbles distributed in the same proportion throughout the cell.

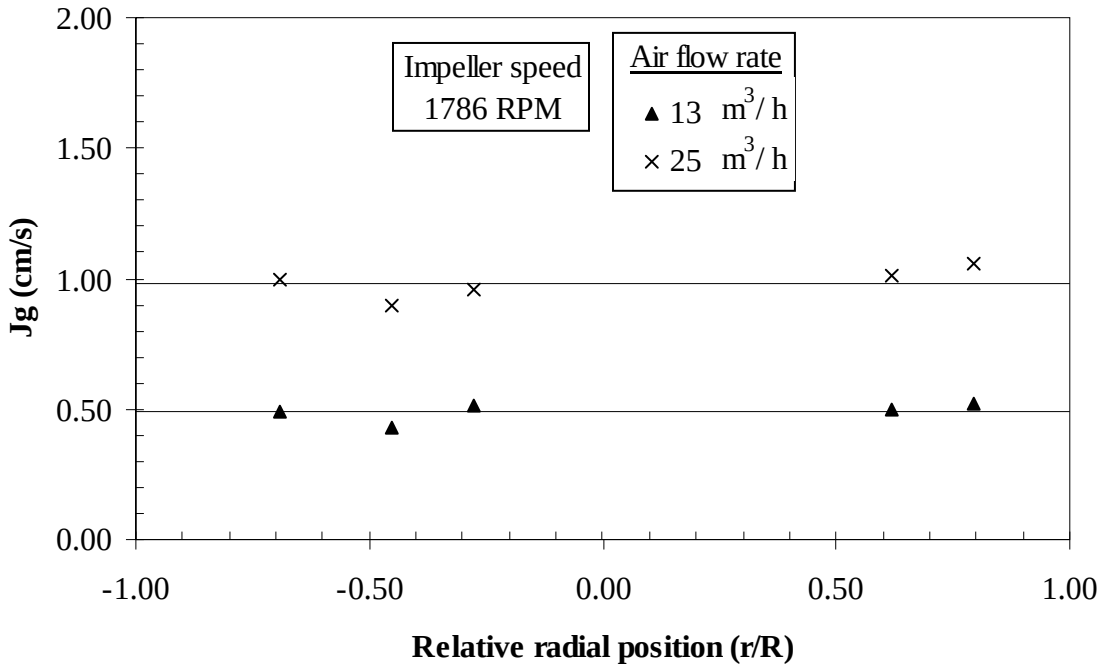

Figure 6. 6 Gas velocity profiles obtained for two levels of air flow rate and high impeller speed

Figure 6. 7 shows the three gas distributions in terms of DDI_A (the low impeller speed, high air flow rate condition was discarded). The difference between the system operated at low and high impeller speed is evident. The two cases for the high impeller speed show ideal distribution, $DDI_A \rightarrow 0$. This indicates that as long as the impeller is operated above a certain speed the bubbles are well distributed throughout the cell. These results show impeller speed is an important factor affecting gas distribution. Although this fact is no doubt appreciated, uniform air distribution to flotation cells does not seem to be a targeted operating condition. Gas distribution can also be a factor in characterizing gas dispersion; for example, bubble size vs. air rate will depend on how well the air is distributed, to the sampling point.

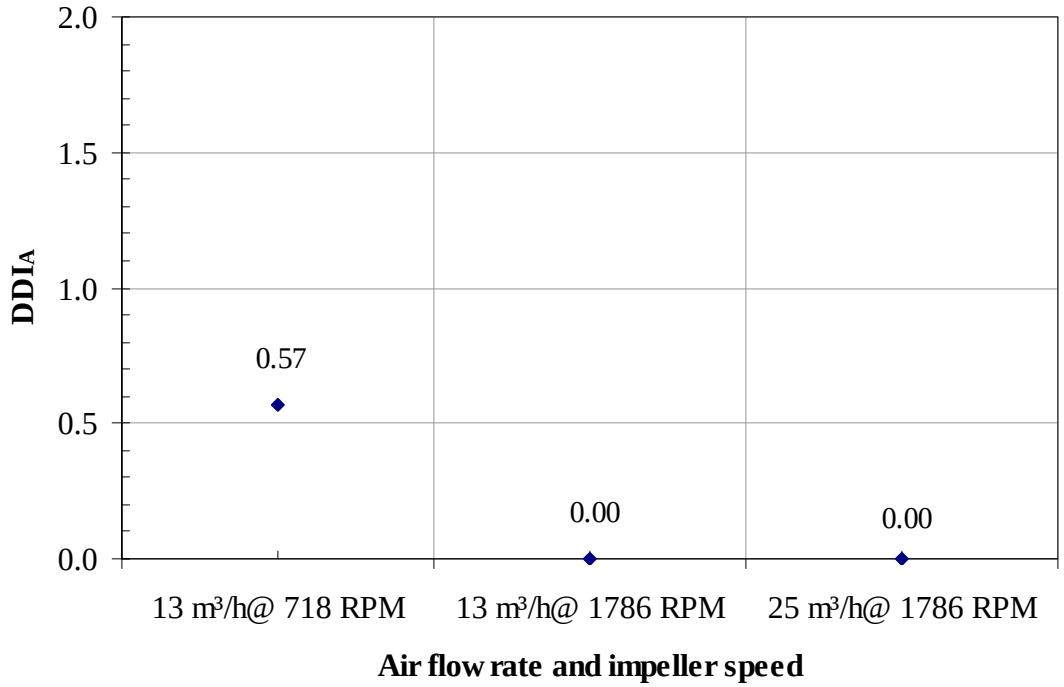

Figure 6. 7 Distribution deviation index (DDI_A) for the test run in the Metso model 0800 mechanical cell

6.3 – Plant experiences

Gas velocity mapping was conducted in two copper concentrators in northern Chile, Salvador and Chuquicamata, in two machine types, a Wemco hybrid-self-aspirated/forced air cell and an Outotec forced air cell, respectively.

6.3.1 – Salvador

The Salvador concentrator was introduced in Chapter 5. The tests were carried out in a square 45 m^3 Wemco mechanical cell. Figure 6. 8 and Figure 6. 9, respectively, show the top view and side view of the installation of the J_g sensors. Gas velocity profiles were measured by installing three J_g sensors at one side of the cell. Due to the structure grating and the impeller mechanism, installation of the J_g sensors closer to the wall or impeller

shaft was not possible. Based on prior evidence the symmetrical distribution assumption is reasonable.

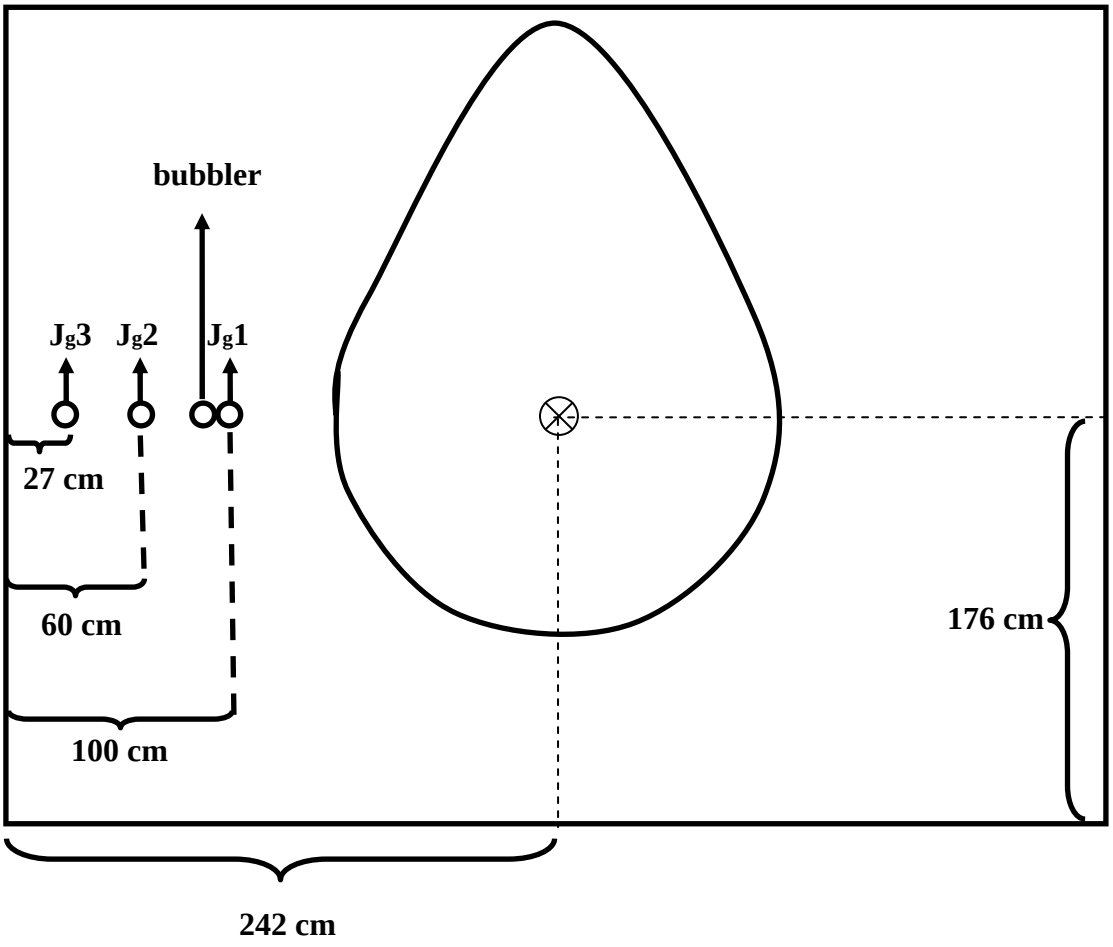

Figure 6. 8 Top view of the sensors installation at Salvador

This particular machine had been modified to operate in either self-aspirated or forced air mode. Figure 6. 9 is a picture of the installation at the plant. The three J_g sensors and the bubbler tube were firmly roped to the cell structure, to counter the strong turbulence in the cell.

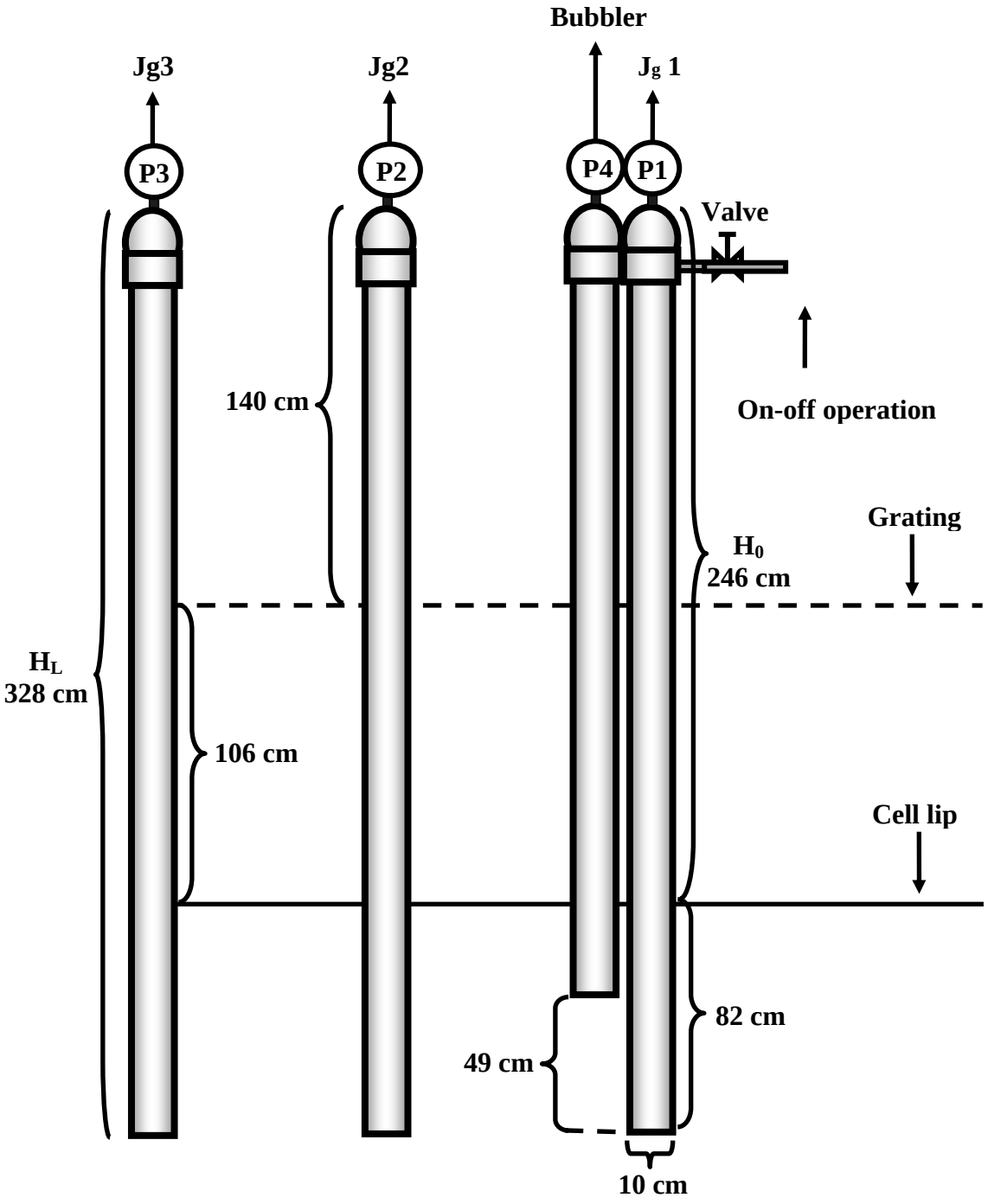

Figure 6. 9 Side view sensors installation at Salvador

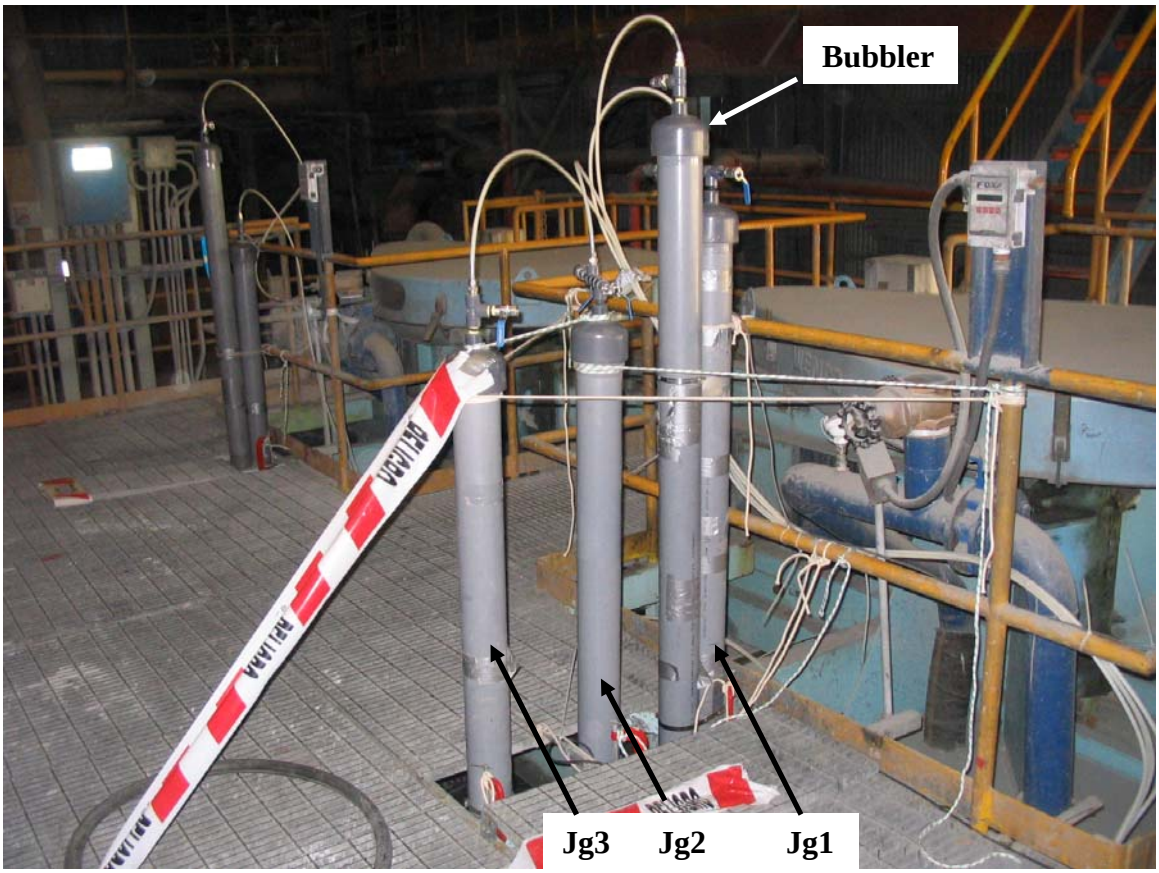

Figure 6. 10 Picture of the J_g sensors installed at Salvador

6.3.1.1 – Self-aspirated mode

Figure 6. 11 shows gas velocity profiles obtained when the cell was operated with water only in self-aspirated mode at three frother concentrations (0, 12 and 20 ppm). All three curves have different profiles, being consistent with the increment in frother concentration, i.e., the more frother in the system the better the gas distribution (flatter the profile). It appears that the data were collected at different gas flow rates, particularly at 12 ppm. This is related to cell operation: the air aspirated into the machine is affected by the hydrostatic pressure, i.e. pulp (or water in this case) level. Level control proved difficult and as a consequence for the three conditions different froth depths, i.e. water levels, were obtained that produced the different air aspiration rates. It is believed that

this difficulty does not degrade the gas distribution information; i.e., the observation that increasing the frother concentration improves gas distribution is valid. The reason offered is that as frother concentration increases bubbles become smaller, which reduces their rise velocity that allows the rotor to distribute them more readily.

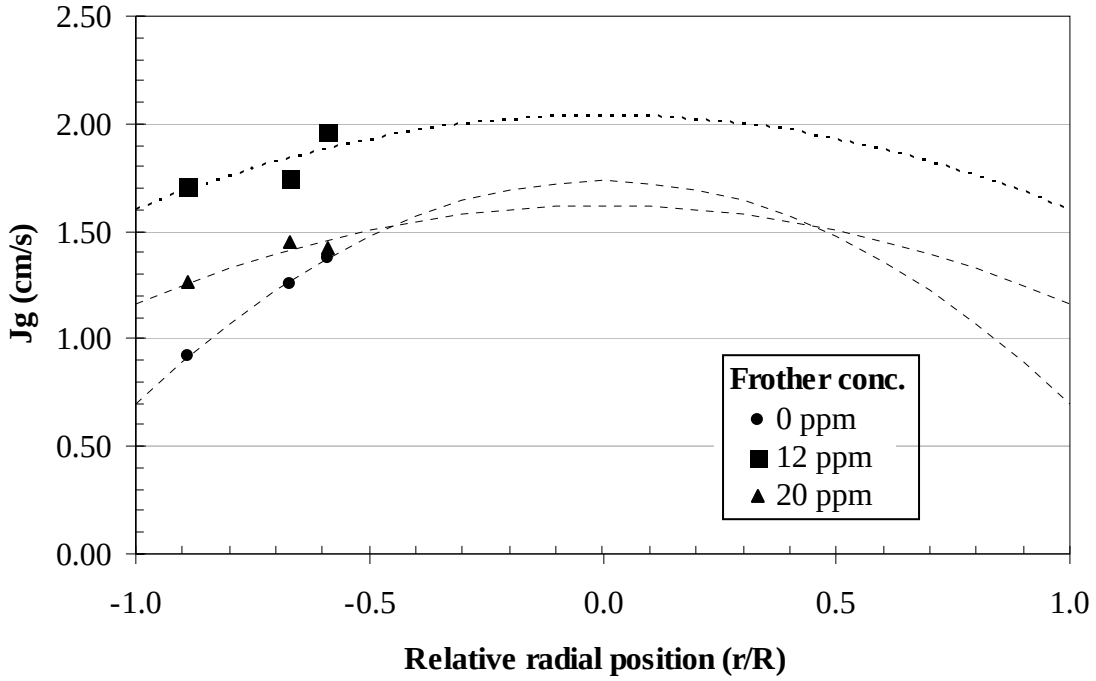

Figure 6. 11 Effect of frother addition on gas velocity profile: Salvador self-aspirated mode

Figure 6. 12 shows the gas distributions expressed as DDI_A, confirming that the higher frother concentrations gave better gas distribution. In the case of 0 ppm the amount of air flowing through the central area is significantly higher. There is not much difference between the 12 and 20 ppm concentrations; both give good distributions ($DDI_A < 0.05$) recalling that $DDI_A = 0$ is the ideal distribution.

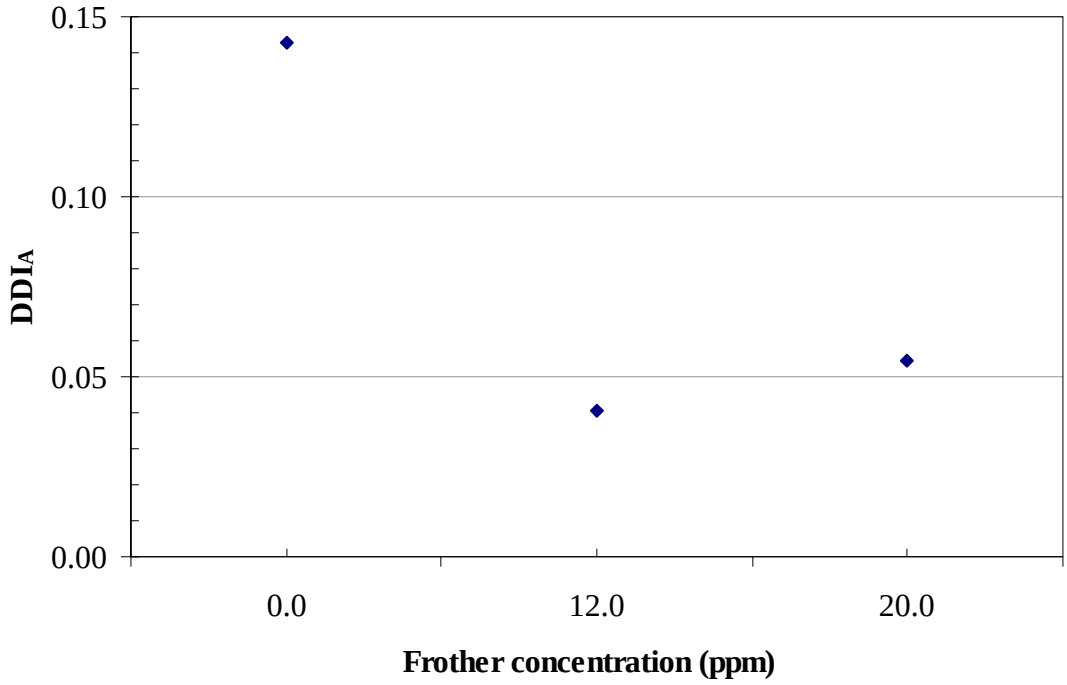

Figure 6. 12 Distribution deviation index (DDI), Salvador self-aspirated mode

6.3.1.2 – Forced air mode

In the next set of tests pulp was used and, for this case, the unit was converted to forced air operation. Air flow rate was changed while keeping frother concentration constant. Figure 6. 13 shows the gas velocity profiles for four gas flow rates: 0.79, 3.72, 5.52 and 7.64 m^3/h. It can be seen that changing the air flow rate did not produce changes in the gas velocity profile. This similarly in profile between air rates suggests that the air is not well distributed, and that a large portion of air exits through the central area. Visual observations confirmed that air flow rate increments caused increased disturbance in the central area (the slurry seemed to be "boiling"). This scenario is similar to that observed in the Metso cell tests at low impeller speed and high air flow rate. As in the Metso case, Figure 6. 13 shows an intuitive interpretation of the gas velocity profile, formed by combining a parabolic profile with a sudden increment of J_g near the central area.

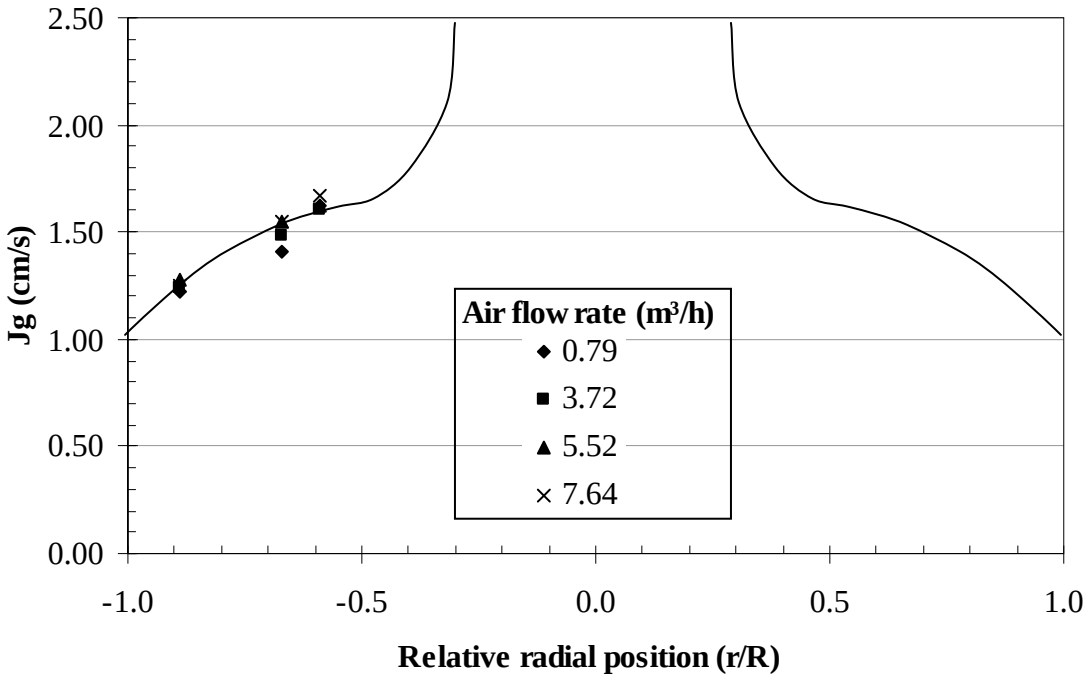

Figure 6. 13 Gas velocity profiles for different gas flow rates for Wemco cell operated as forced air

6.3.2 - Chuquicamata

Another survey was performed at the Chuquicamata concentrator, located 1 650 kilometers north of the capital city, Santiago, and 2 870 meters above sea level. Chuquicamata entered operations in 1910. Its current production is ca. 800 000 tons of electro-refined copper with 99.99% purity. It also produces ca. 19 000 metric tons of fine molybdenum.

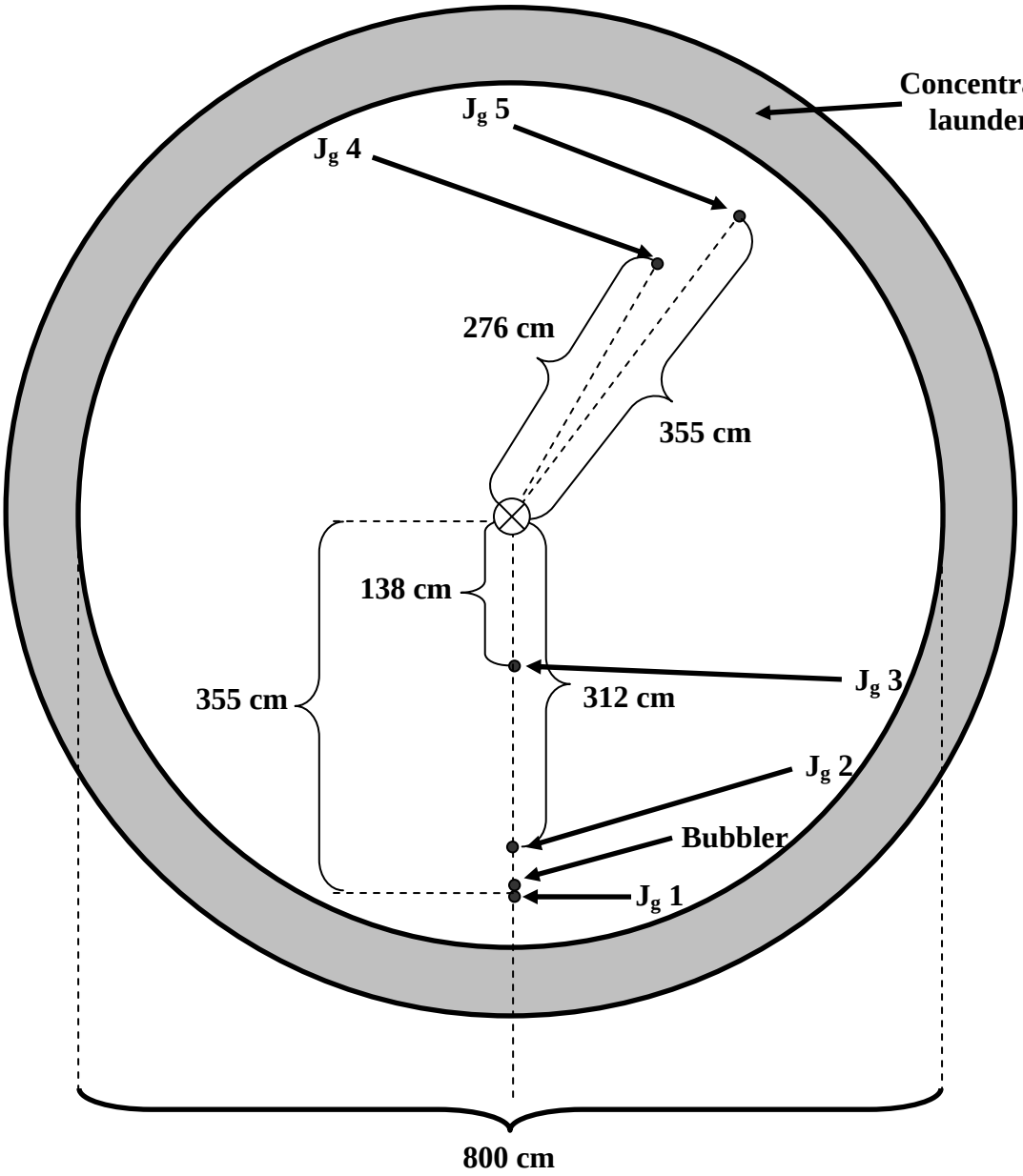

Figure 6. 14 Top view illustration of the installation of J_g sensors at Chuquicamata

Gas velocity profiling was performed in a 300 m^3 Outotec cell. Figure 6. 14 and Figure 6. 15 show top view and side view, respectively, of the J_g sensor installation. Due to the size of the machine, the sensors and the bubbler are ca. 500 cm long. Figure 6. 16 is a picture of the sensors firmly attached to the structure.

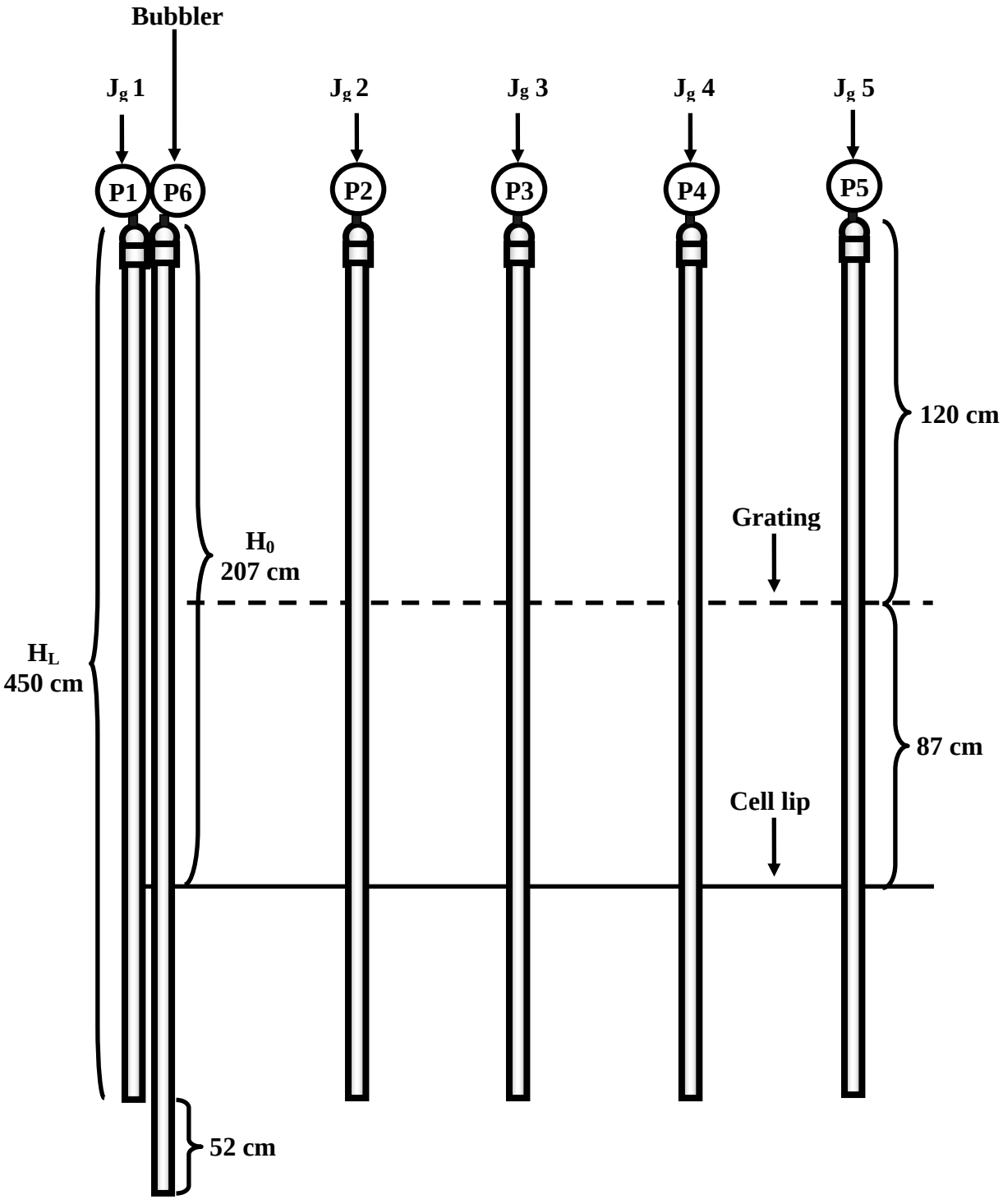

Figure 6. 15 Side view illustration of the J_g sensor installation at Chuquicamata

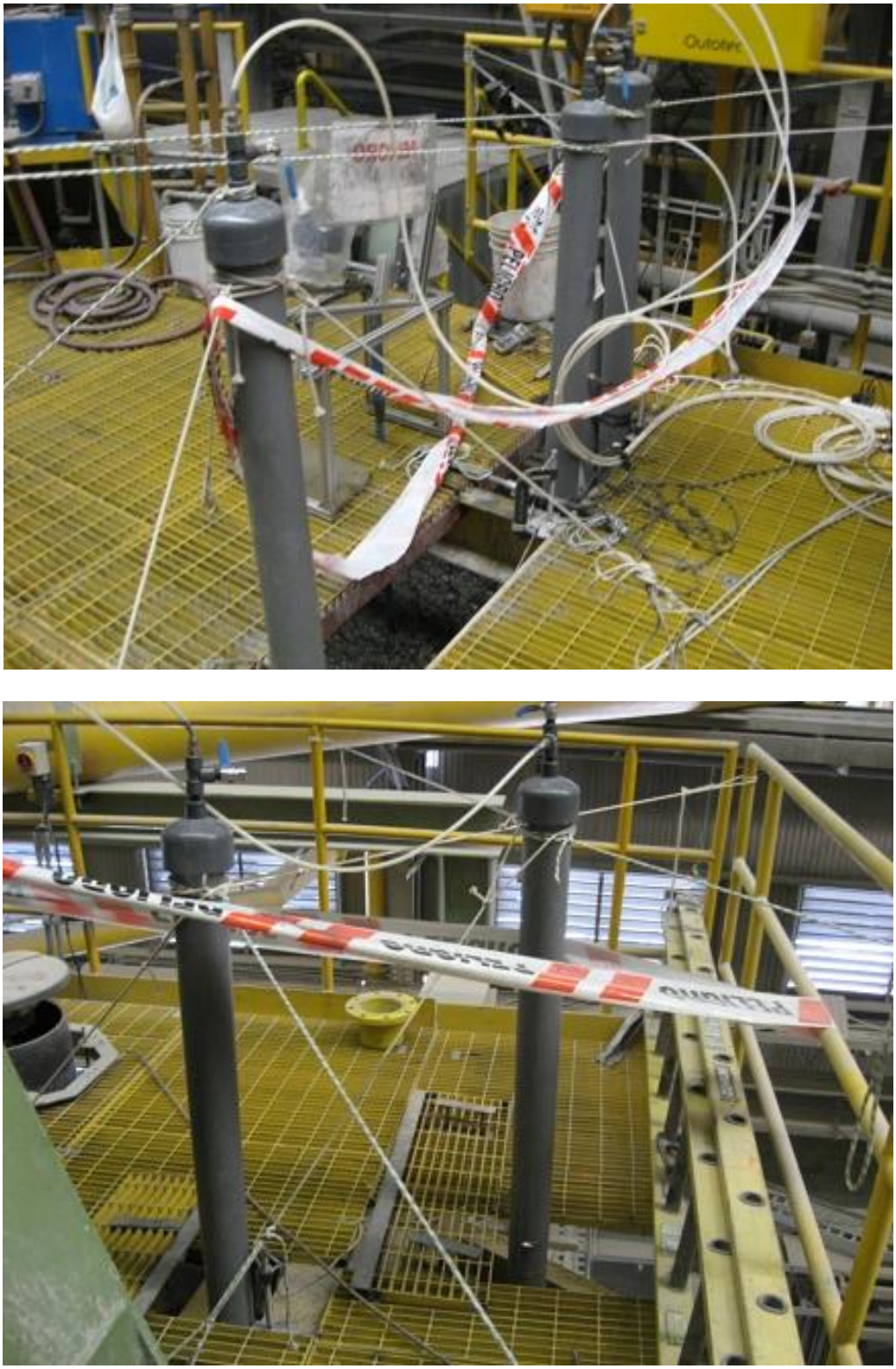

Figure 6. 16 Picture of the J_g sensor installation at Chuquicamata concentrator: Jg_1, Jg_2 and Jg_3 (above); Jg_4 and Jg_5 (below)

Figure 6. 17 shows the gas velocity profiles when the system was run with water only at five frother concentrations (14, 16, 19, 25 and 35 ppm) and a fixed gas flow rate (20 m^3/h). It was not possible to start with a lower frother concentration because the re-circulated water at the plant contained 14 ppm frother. No difference in profile was observed, attributed to the combination of high frother concentration and adequate impeller speed. The profiles represent good gas distribution, there being practically no difference between the J_g registered towards the wall and towards the center.

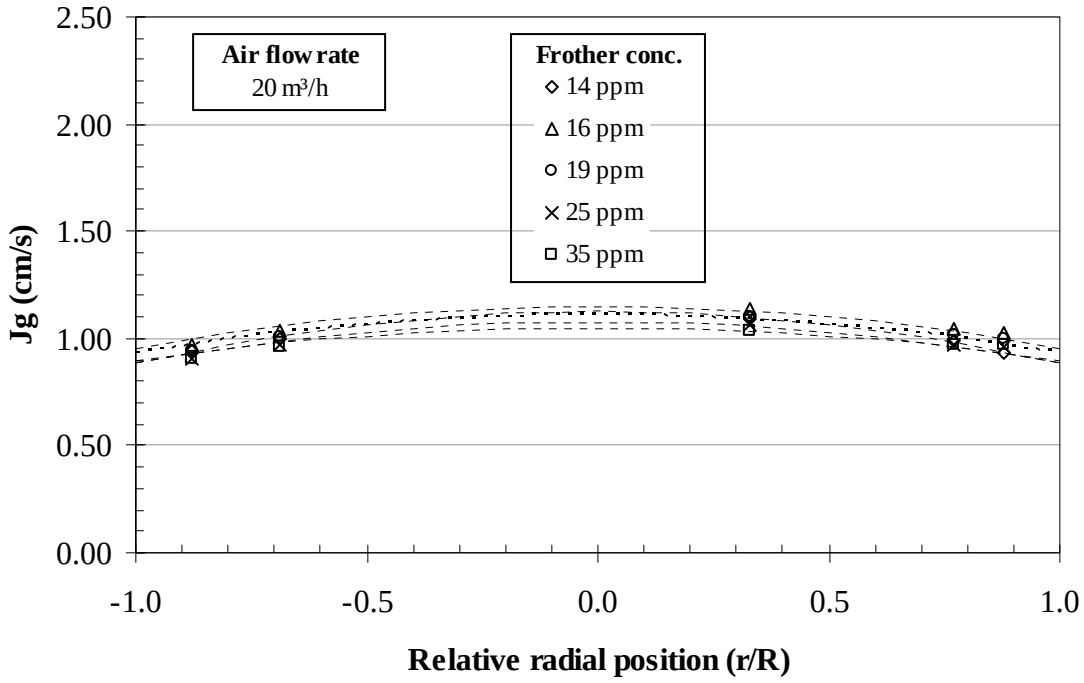

Figure 6. 17 Effect of frother addition on gas velocity profile at Chuquicamata

Figure 6. 18 shows gas velocity profiles measured when the system was operated with water only at fixed frother concentration (14 ppm) and three gas flow rates, 10, 20 and 30 m^3/h. A small increment in curvature as the air flow rate was increased is

detected.

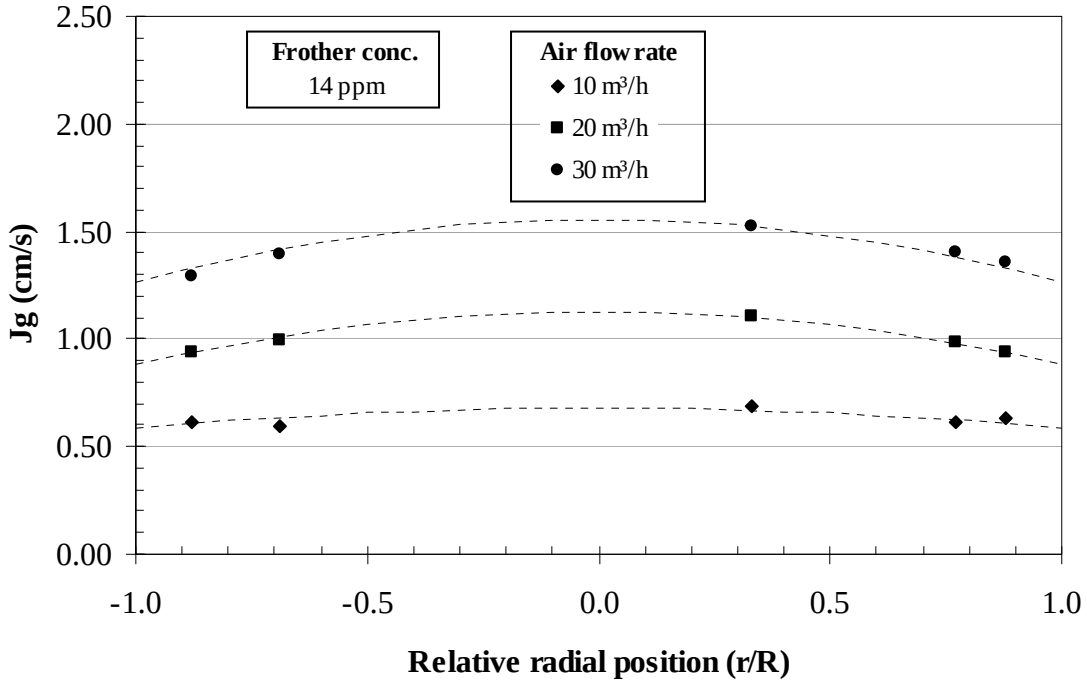

Figure 6. 18 Gas distribution at fixed frother concentration

Figure 6. 19 and Figure 6. 20 show the gas distributions expressed as DDI_A for the tests at fixed air flow rate and fixed frother concentration, respectively. For the second case, the highest frother concentration produced the lowest DDI_A but the values are all so low that the differences are not material (i.e. there would be not an expected impact on metallurgical response). In the case of the tests at fixed frother concentration, the best scenario (lowest DDI_A) was found to be at the lowest flow rate. The DDI_A calculated for the two other flows, i.e., 20 and 30 m^3/h, are higher and close to each other. Again, however, in practical terms, gas distribution in the Outotec machine is close to ideal ($DDI_A \rightarrow 0$).

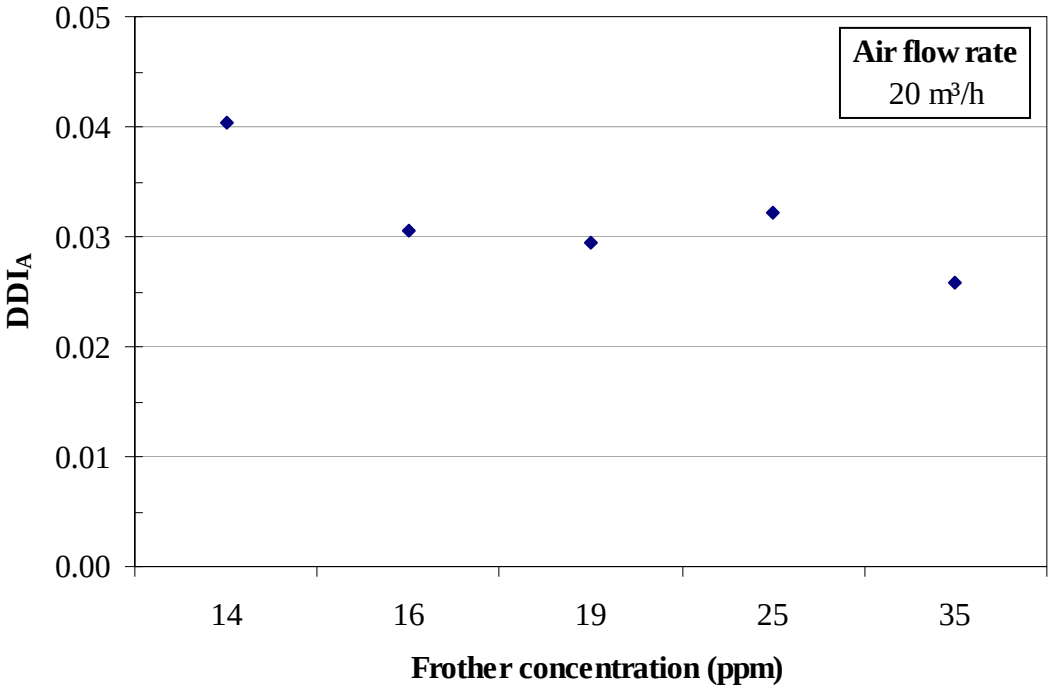

Figure 6. 19 Gas distribution deviation index for fixed air flow rate

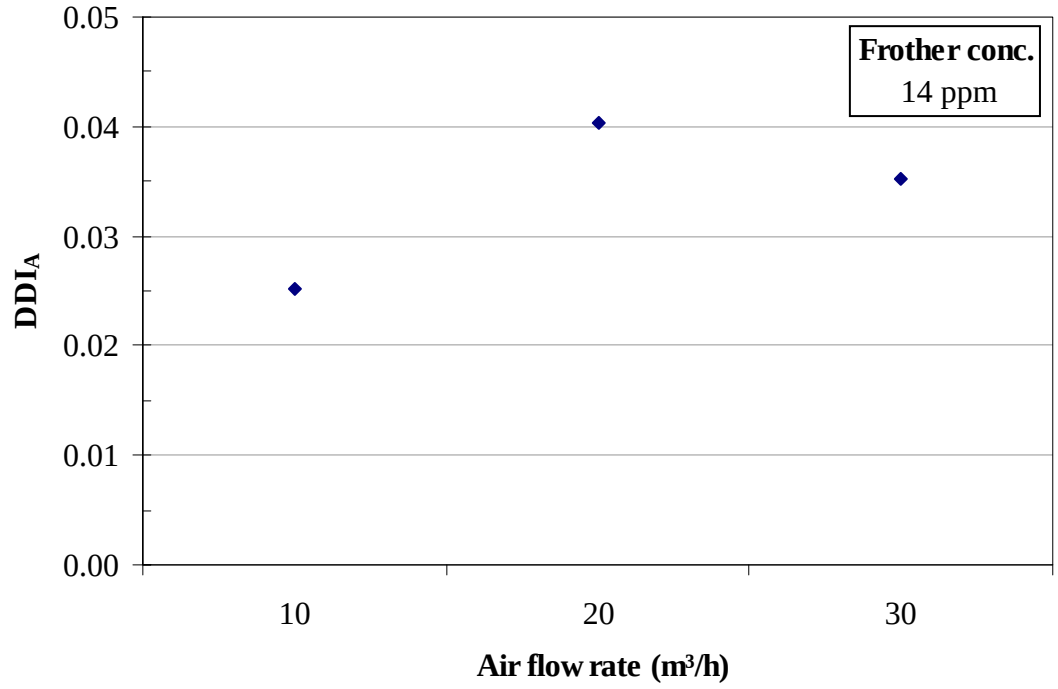

Figure 6. 20 Gas distribution deviation index for fixed frother concentration

Based on the results in the Outotec cell, it is difficult to imagine better performance in terms of gas distribution. It is speculated that the impeller speed was the cause of such good gas distributions, but this hypothesis has to be verified.

CHAPTER 7

CONCLUSIONS AND FUTURE WORK

7.1 – Conclusions

An analysis of gas velocity measurements and its use to gas distribution is the principal outcome of this work. In specific detail, the following are concluded:

7.1.1 – Difference between continuous and on-off technique

Two techniques for measuring superficial gas velocity, on-off and continuous, were validated in a water-air system, showing good agreement. Measurements in plant indicated a consistent difference with higher gas velocity using the continuous mode.

The origin of the difference was tested by challenging the original assumption that the density of the aerated slurry was the same outside and inside the sensor. The on-off model was re-derived (corrected) now assuming that there is a difference between the aerated slurry densities inside and outside the sensor. The physical interpretation is that particles can sediment from the sensor tube. Comparison between the original and corrected model supported that the aerated slurry densities inside and outside the sensor were different. Correction of the on-off model reconciled the on-off and continuous gas velocity techniques.

7.1.2 – Estimation of density of aerated slurry inside the Jg sensor

For simplicity, it was proposed that the density of the aerated slurry inside the J_g sensor is intermediate between the density of the aerated slurry outside the sensor and a density of aerated water (no solids) inside the tube. This estimate of density gives 0.83 ρ_b, where ρ_b is aerated slurry density outside the sensor for slurry with 35 percent solids by weight.

7.1.3 – Using McGill on-off sensor to give continuous J_g

The J_g signal given by the continuous technique is more suitable for process control than the intermittent signal given by the on-off technique. An issue with the continuous device is that under certain conditions froth buildup occurs in the sensor tube that eventually fouls the orifice, leading to error in J_g. A method for collecting a continuous signal from the on-off technique was proposed.

7.1.4 – Gas distribution

A technique for measuring gas distribution was presented consisting in measuring J_g simultaneously at different radial distances at a common depth (radial J_g mapping). Interpretation of the data from J_g mapping was based on an assumption of parabolic profile. Derivation of a deviation distribution index (DDI) was presented to be used as a numerical parameter to represent the quality of the air distribution.

7.1.5 – Sampling point for the cell average J_g

On occasion, measurements of gas dispersion properties are performed at a single sampling point in the cell. Based on the parabolic profile, a sampling point was derived from the theory of flow through circular pipes. The sampling point to give the average J_g was determined to be at the dimensionless radial distance equal 0.71.

7.2 – Future work

7.2.1 – Measurement of the density of aerated slurry inside the sensor

To determine J_g with the on-off method with the accuracy of the continuous method, it is required to develop a technique to measure the density of the aerated slurry inside the sensor.

7.2.2 – Continuous J_g measurements using the on-off technique

The method for collecting a continuous signal from the on-off technique requires more detailed analysis to find an algorithm that gives a signal most suited for process control purposes.

7.2.3 – Metallurgical impact of gas distribution management

It is necessary to collect experimental evidence from plants to confirm the suspicion that best metallurgical results are obtained when uniform gas distribution is provided to the cells.

REFERENCES

- Azgomi, F., Gomez, C.O., Finch, J.A., "Correspondance of gas holdup and bubble size in presence of different frothers", Int.J. Miner. Process., 83, pp. 1-11, 2007.
- Claridge, P.G., "Operation and maintenance in mineral processing plants", CIM, Montreal, Special volume 40, pp. 267-290, 1989.
- Clayton, R., G.J. Jameson, Manlapig, E.V., "The development and application of the Jameson cell", Minerals Engineering, Vol. 4, Nos 7–11, pp. 925–933, 1991.
- Cooper, M., Dahlke, R., Gomez, C.O. and Finch, J.A., "Impact of air distribution profile on banks in a Zn cleaning circuit", CIM Bulletin, 97, 1083, pp. 73-78, 2004.
- Cowburn, J., Harbort, G., Manlapig, E., Pokrajcic, Z., "Improving the recovery of coarse coal particles in a Jameson cell", Minerals Engineering, Vol. 19, pp. 609 – 618, 2006.
- Dahlke, R., Scott, D., Leroux, D., Gomez, C.O., Finch, J.A., "Troubleshooting cell operation using gas velocity measurements", Proceedings-33rd Annual Meeting of the Canadian Mineral Processors (division of CIM), January 23–25, pp. 359–370, 2001.
- Dahlke, R., Gomez, C.O., Finch, J.A., "Operating range of a flotation cell determined from gas holdup vs. gas rate", Minerals Engineering, 18, pp. 977 – 980, 2005.

- Degner, V.R., Treweek, H.B., “Large flotation cell design and development”, A.M. Gaudin Memorial Volume, Vol.2, Ed. M.C. Fuerstenau, AIME, New York, pp. 838 – 837, 1976.
- Dobby, G.S., Finch, J.A., “Column flotation: A selected review, part II”, Minerals Engineering, Vol. 4, Nos 7 – 11, pp. 911 – 923, 1991.
- Dodge, B.F., “Chemical Engineering Thermodynamics”, first edition, McGraw Hill, pp. 317-320, 1944.
- Doucet, J.S., “Cell characterization: Understanding gas dispersion in industrial flotation machines”, Master Thesis, McGill University, Montreal, Quebec, Canada, 2006.
- Fallenius, K., “Outokumpu flotation machines”, A.M. Gaudin Memorial Volume, Vol.2, Ed. M.C. Fuerstenau, AIME, New York, pp. 838 – 861, 1976.
- Falutsu, M., “Direct measurement of gas rate in a flotation machine”, Minerals Engineering, Vol. 7, No 12, pp. 1487-1494, 1994.
- Finch, J.A. and Dobby, G.S, “Column flotation”, Pergamon Press, 1990.
- Finch, J.A., “Column flotation: A selected review – part iv: Novel flotation devices”, Minerals Engineering, vol. 8, No. 6, pp. 587-602, 1995.
- Finch, J.A., Gomez, C.O., Hardie, C. and Leichtle, G., “Bubble surface area flux: a parameter to characterize flotation cells”, Annual Operator’s Conference of the Canadian Mineral Processors, 31, pp. 199-209, Ottawa, 1999.
- Finch, J.A., Xiao, J., Hardie, C. and Gomez, C.O., “Gas dispersion properties: bubble surface area flux and gas holdup”, Minerals Engineering, 13, 4, pp. 365 – 372, 2000.

- Finch, J.A., Nesset, J. E., Acuña, C., “Role of frother on bubble production and behavior in flotation”, Minerals Engineering, 21, pp. 949-957, 2008.
- Fox, R. and McDonald, “Introduction to Fluid Mechanics”, Fifth edition, John Wiley & Sons, INC., pp. 382-383, 1998.
- Gerhart, P.M., Gross, R.J., Hochstein, J.I., “Fundamentals of Fluid Mechanics”, second edition, Addison-Wesley Publishing Company, 1992, pp. 526-527, 1992.
- Gomez, C.O. and Finch, J.A., “Gas dispersion measurements in flotation machines”, CIM Bulletin, vol. 95, 1066, pp. 73-78, 2002.
- Gomez, C.O., Cortés-López, F., Finch, J.A., “Industrial testing of a gas holdup sensor flor flotation systems”, Minerals Engineering, 16, pp. 493-501, 2003.
- Gomez, C.O., and Finch, J.A., “Gas dispersion measurements in flotation cells”, International Journal of Mineral Processing 84, pp. 51–58, 2007.
- Gorain, B.K., Franzidis, J.P. and Manlapig, E.V., “Studies on impeller type, impeller speed and air flow rate in an industrial scale flotation cell. Part 3: Effect on superficial gas velocity”, Minerals Engineering, Vol. 9, No. 6, pp. 639-654, 1996.
- Gorain, B.K., Franzidis, J.P., Manlapig, E.V., “Studies on impeller type, impeller speed and air flow rate in an industrial scale flotation cell. Part 4: Effect of bubble surface area flux on flotation performance”, Minerals Engineering, Vol. 10, No. 4, pp. 367-379, 1997.
- Gorain, B.K, “Optimization of flotation circuits with large flotation cells”, In: G.J. Jameson and R.H. Yoon, Editors, Proceedings Centenary of Flotation Symposium, Brisbane, QLD, 6-9 June, Aus IMM, pp. 843–852, 2005.

- Grau, R.A., Heiskanen, K., “Gas dispersion measurements in a flotation cell”, Minerals Engineering 16, 1081-1089, 2003.
- Grau, R., Heiskanen, K., “Bubble size distribution in laboratory scale flotation cells”, Minerals Engineering, 18, pp. 1164-1172, 2005.
- Harbort, G.J., Jackson, B.R., Manlapig, E.V., “Recent advances in Jameson flotation cell technology”, Minerals Engineering, Vol. 7, Nos. 2/3, pp. 319 – 332, 1994.
- Harbort, G., De Bono, S., Carr, D., Lawson, “Jameson cell fundamentals – A revised perspective”, Minerals Engineering, Vol. 16, pp. 1091 – 1101, 2003.
- Harris, C.C., “Flotation machines”, A.M. Gaudin Memorial Volume, Vol.2, Ed. M.C. Fuerstenau, AIME, New York, pp. 753 – 815, 1976.
- Hernandez, H., Gomez, C.O., Finch, J.A., “Gas dispersion de-inking in a flotation column”, Minerals Engineering, 16, pp. 739-744, 2003.
- Janna, W., “Introduction to Fluid Mechanics”, third edition, PWS Publishing Company, Boston, pp. 566-567, 1993.
- Jameson, G.J., “Physics and hydrodynamics of bubbles”, The Scientific Basis of Flotation, Ed. Kenneth J. Ives, pp. 53 - 77, 1984.
- Jameson, G.J. and Allum, P., “A survey of bubbles sizes in industrial flotation cells”, Report to Amira Ltda, 22 august 1984.
- Jonaitis, A.J., “Design, development, application, and operating benefits of 100-m^3 + Outokumpu TankCell flotation cells”, Advances in Flotation Technology, B.K. Parekh and J.D. Miller, Eds., Proceedings Annual SME Meeting, Mar. 1-3, 1999, Denver, USA, pp. 371-380.

- John, J.E., Haberman, W., “Introduction to Fluid Mechanics”, third edition, Prentice Hall, pp. 498, 1988.
- Kracht, W., Gomez, C.O., Finch, J.A., “Controlling bubble size using a frit and sleeve sparger”, Minerals Engineering, 21, pp. 660-663, 2008.
- Lin, T. J., Reese, J., Hong, T. and Fan, L.S., “Quantitative analysis and computation of two-dimensional bubble columns”, AIChE J., 42, pp. 301-318, 1996.
- MacNamara, L., Traczyk, F., Foreman, D., “Flotation cell selection – Choosing the right cell for the job”, SAIMM, Flotation Technology Conference, Mistry Hills, South Africa, paper No.6, 2007.
- Massey, B., “Mechanics of Fluids”, seventh edition, Stanley Thornes (Publishers) Ltd., pp. 131, 1998.
- Montgomery, D.C. and Runger, G.C., “Applied statistics and probability for engineers”, John Wiley & Sons Inc., Third Edition, pp. 240, 2003.
- Nagata, S. “Mixing: Principles and applications”, Halsted Press, pp. 335 – 367, 1975.
- Neset, J.E., Hernandez-Aguilar, J.R., Acuña, C., Gomez, C.O., Finch, J.A., “Some gas dispersion characteristics of mechanical flotation machines”, Minerals Engineering, 19, pp. 807-815, 2006.
- Outotec, “Flotation technologies ”, brochure, www.outotec.com, 2009.
- Rudolphy, L., Grau, R.A., Heiskanen, K., “On-line sensor for measuring gas velocities in laboratory-scale flotation cells”, Centenary of Flotation Symposium, Ed. G.J. Jameson, Brisbane, Qld, June 6-9, pp. 573-580, 2005.

- Sanwani, E., Zhu, Y., Franzidis, J.P., Manlapig, E.V., Wu, J., "Comparison of gas hold-up distribution measurement in a flotation cell using capturing and conductivity techniques", Minerals Engineering, 19, pp. 1362-1372, 2006.
- Schetz, J. and Fuhs, A.E., "Fundamentals of Fluid Mechanics", John Wiley and Sons, INC., pp. 13, 1999.
- Schwarz, S., Alexander, D., "Gas dispersion measurements in industrial flotation machines", Minerals Engineering, 19, pp. 554-560, 2006.
- Shergold, H.L., "Flotation in mineral processing", The Scientific Basis of Flotation, Ed. Kenneth J. Ives, pp. 229 – 287, 1984.
- Tatterson, G.B., "Fluid mixing and gas dispersion in agitated tanks", McGraw-Hill Inc., pp. 1-16; 417-528, 1991.
- Torrealba-Vargas, J.A., "Design of novel gas velocity sensor for flotation systems", Phd. Thesis, McGill University, Montreal, Quebec, Canada, 2004.
- Torrealba-Vargas, J.A., Gomez, C.O., Finch, J.A., "Continuous air rate measurement in flotation cells: A step towards gas distribution management", Minerals Engineering, 17, pp. 761-765, 2004.
- Tzeng, J. W., Chen, R.C., and Fan, L.S., "Visualization of flow characteristics in a 2-d bubble column and three phase fluidized bed", AIChE J., 39, pp. 733-744, 1993.
- Weber, A., MacNamara, L., Schreiber, H., "Design, installation and testing of the no. 250 Wemco Smartcell® flotation machine at mineral Los Pelambres", SAIMM, Flotation Technology Conference, Mistry Hills, South Africa, paper No.5, 2007.

- Wills, B.A., “Mineral processing technology”, Sixth Edition, Butter-Heinemann, Oxford, England, 1997, pp. 258 – 341.
- White, F.M., “Fluid mechanics”, McGraw Hill, Fourth Edition, pp. 71, 143, 144, 341 and 342, 2006.
- Wyslouzil, H.E., “The use of column flotation for the recovery of ultra-fine phosphates”, Canadian Process Technologies, Inc., en-ca.eriez.com\products\ columncell0, 2009.
- Xstrata Technology, “About Jameson cell”, brochure, www.jamesoncell.com, 2009.
- Xu, M., Finch, J.A., Huls, B.J., “Measurement of radial gas holdup profiles in a flotation column”, Int. J. Miner. Process, 36, pp. 229-244, 1992.
- Yañez, A.C., “Superficial gas velocity measurement in flotation cells by the McGill J_g sensor, evaluation of on-off and continuous versions”, Bachelor Engineering Thesis, Universidad de Concepción, Chile, 2006.
- Yianatos, J., Bergh, L., Condori, P. and Aguilera, J., “Hydrodynamic and metallurgical characterization of industrial flotation banks for control purposes”, Minerals Engineering, Vol. 14, No. 9, pp 1033-1046, 2001.
- Yianatos, J., Bucarey, R., Larenas, J., Henriquez, F., Torres, L., “Collection zone kinetic model for industrial flotation columns”, Minerals Engineering, 18, pp. 1373-1377, 2005.
- Yianatos, J.B., Larenas, J.M., Moys, M.H., Diaz, F.J., “Short time mixing response in a big flotation cell”, International Journal of Mineral Processing, 89, pp. 1-8, 2008.

APPENDIX A: CALIBRATION DATA

Table A. 1 Mass flow meter calibration data

Ref. Qg (LPM)	P_{ini} (atm)	T_{ini} (K)	V_{ini} air (L)	M_{ini} air (g)	Pfinal (atm)	Tfinal (K)	Volume H2O displaced (L)	Vfinal air (L)	M_{final} air (g)	Diff. Mair (g)	Vair @ 0C 1 atm	Time (s)	Measured Qg (LPM)	St. Dev (%)	Replicates
5 LPM mass flow meter calibration															
1.00	0.99	294.68	3.13	3.69	1.00	294.70	1.07	4.20	4.99	1.30	1.01	59.44	1.02	1.21	5
2.00	0.99	294.93	3.13	3.69	1.00	294.94	2.17	5.30	6.32	2.63	2.05	59.79	2.06	0.55	5
3.00	0.99	295.15	3.13	3.69	1.01	295.14	3.18	6.31	7.54	3.86	3.00	58.47	3.08	0.35	5
4.00	0.99	295.43	3.13	3.68	1.01	295.48	3.91	7.04	8.45	4.76	3.71	54.53	4.08	0.18	5
5.00	0.99	295.59	3.13	3.68	1.02	295.59	5.04	8.17	9.85	6.17	4.80	56.22	5.12	0.15	5
20 LPM mass flow meter calibration															
1.00	1.00	294.40	3.13	3.72	1.01	294.41	1.96	5.09	6.11	2.39	1.86	57.88	1.93	0.22	5
2.00	1.00	294.59	3.13	3.72	1.02	294.59	4.01	7.14	8.65	4.93	3.84	59.02	3.90	0.22	5
3.00	1.00	294.68	3.13	3.72	1.03	294.68	5.90	9.03	11.05	7.33	5.71	57.85	5.92	0.18	5
4.00	1.00	294.78	3.13	3.72	1.04	294.75	7.95	11.07	13.68	9.96	7.75	58.76	7.92	0.28	5
30 LPM mass flow meter calibration															
2.00	0.99	294.98	3.13	3.69	1.00	295.04	1.70	4.83	5.75	2.06	1.60	56.59	1.70	1.01	5
4.00	0.99	295.13	3.13	3.69	1.01	295.13	3.49	6.62	7.94	4.25	3.31	56.14	3.54	0.26	5
6.00	0.99	295.15	3.13	3.69	1.02	295.18	5.22	8.35	10.10	6.41	4.99	54.80	5.47	0.25	5
8.00	0.99	295.28	3.13	3.69	1.03	295.28	7.21	10.34	12.63	8.94	6.96	55.84	7.48	0.15	5
400 LPM mass flow meter calibration															
40.00	1.01	295.15	3.13	3.76	1.20	295.15	27.74	30.87	44.18	40.43	31.46	58.71	32.16	0.66	3
50.00	1.01	295.09	3.13	3.76	1.24	295.09	35.07	38.20	56.47	52.71	41.03	59.08	41.69	2.85	3
60.00	1.01	295.19	3.13	3.76	1.28	295.15	42.07	45.20	68.86	65.10	50.67	58.94	51.59	1.04	3
Linear trend line															
						Mass flow meter			**Equation**		**R^2**				
						0 to 5 LPM			y = 1.024 x		0.99996				
						0 to 20 LPM			y = 0.986 x		0.9998				
						0 to 30 LPM			y = 0.918 x		0.997				
						0 to 400 LPM			y = 0.840 x		0.981				

Table A. 2 Pressure transmitter calibration data

Hydrostatic pressure (cmH2O)	Wika S-10 range 0-127(cmH2O)	Wika S-10 range 0-1054(cmH2O)
0	-0.52	0.15
10	9.46	10.70
20	19.44	20.74
30	29.42	30.52
40	39.40	40.56
50	49.38	50.60
60	59.36	60.60
70	69.34	70.80
80	79.32	80.78
90	89.30	90.82
100	99.29	100.93

Linear trendline		
Range	**Equation**	**R^2**
0-127 cmH2O	y = 0.9906 x	0.9999
0-1054 cmH2O	y = 1.0107 x	0.9999

Table A. 3 Orifices calibration data

Temperature (K)	P1 (kPa)	P2 (kPa)	DP (kPa)	ρ_a (kg/m³)	SQRT ($\Delta P/\rho_a$) (m/s)	Air flow rate (cm³/s)
0.8 mm						
297.84	104.19	103.90	0.59	1.21	0.70	8.34
297.84	105.42	104.51	1.82	1.22	1.22	16.84
297.83	109.59	106.59	5.99	1.24	2.20	34.17
297.80	115.97	109.79	12.37	1.28	3.11	51.18
1 mm						
297.71	103.83	103.72	0.23	1.21	0.44	8.34
297.97	104.28	103.94	0.68	1.21	0.75	16.84
297.85	105.73	104.67	2.13	1.22	1.32	34.01
297.65	114.71	109.15	11.11	1.27	2.96	85.52
1.2 mm						
293.31	101.90	101.70	0.40	1.20	0.82	25.45
293.08	102.81	102.16	1.31	1.21	1.47	41.29
293.05	104.09	102.80	2.59	1.22	2.06	55.97
293.12	105.75	103.63	4.25	1.22	2.63	69.43
1.4 mm						
297.92	104.20	103.90	0.60	1.21	0.70	27.51
297.84	105.65	104.62	2.05	1.22	1.30	59.85
297.83	108.16	105.88	4.56	1.23	1.93	92.02
297.75	116.13	109.87	12.53	1.28	3.13	151.36
Linear trend line						
Orifice diameter			Equation		R^2	
0.8 mm			$y = 17.808 x - 4.571$		0.9995	
1.0 mm			$y = 30.845 x - 6.013$		0.9996	
1.2 mm			$y = 24.246 x - 5.676$		0.9999	
1.4 mm			$y = 50.804 x - 6.942$		0.9995	

APPENDIX B: ORIFICE THEORY

In this appendix, theory of the flow measurement using orifices is presented. Figure B. 1 shows an illustration of the classical application of orifice plate (Dodge, 1944; Fox and McDonald, 1998; Gerhardt and Gross, 1992; Janna, 1993; John, 1988; Massey, 1998; Schetz and Fush, 1999). The flow of liquids and gases through orifices is derived by applying Bernoulli's theorem given by,

$$\left(\frac{P_1}{\rho g}+\frac{v_1^2}{2g}+z_1\right)-\left(\frac{P_2}{\rho g}+\frac{v_2^2}{2g}+z_2\right)=0 \qquad \text{(B. 1)}$$

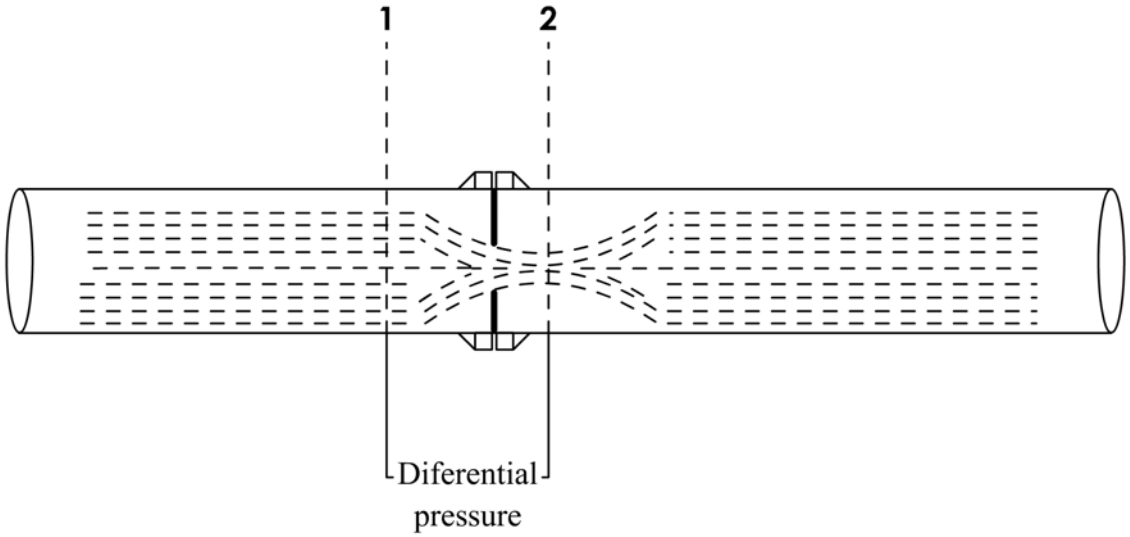

Figure B. 1 Illustration of an orifice meter

which involves only mechanical terms. In a horizontal application $z_1 = z_2$. Re-arranging terms,

$$\left(\frac{P_1 - P_2}{\rho g}\right)=\frac{v_2^2 - v_1^2}{2g} \qquad \text{(B. 2)}$$

Considering incompressible flow and continuity,

$$v_1 A_1 = v_2 A_2 \qquad \text{(B. 3)}$$

Or

$$v_1 = \frac{A_2}{A_1} \cdot v_2 = \left(\frac{D_2}{D_1} \right)^2 \cdot v_2 \tag{B. 4}$$

It is convenient to define a new variable β,

$$\beta = \frac{D_2}{D_1} \tag{B. 5}$$

Substituting Equation (B. 4) and Equation (B. 5) into Equation (B. 2), and re-arranging,

$$v_2 = \sqrt{\frac{2\Delta P}{\rho(1-\beta^4)}} \tag{B. 6}$$

The volumetric flow (Q) through the orifice is determined by applying continuity,

$$Q_2 = \frac{\pi \cdot D_1}{4} \sqrt{\frac{2\Delta P}{\rho(1-\beta^4)}} \tag{B. 7}$$

This derivation of Equation (B. 7) is ideal because it does not take into account the tube roughness and other not measurable variables. More over, if the fluid is compressible, then the density is not constant, therefore it is necessary to introduce empiric correction factors experimentally obtained. Introducing the correction factors and re-arranging gives,

$$Q_2 = a \cdot \sqrt{\frac{\Delta P}{\rho}} + b \tag{B. 8}$$

Where a and b are empiric constants.

APPENDIX C: EXPERIMENTAL DATA

Table C. 1 Comparison between on-off and continuous method

(no collection of bubbles)

Item	Jg reference (cm/s)	Jg on-off (cm/s)	Jg continuous (cm/s)
1	0.47	0.48	0.42
2	0.47	0.48	0.43
3	0.47	0.48	0.43
4	0.47	0.48	0.43
5	0.47	0.48	0.42
6	0.93	0.94	0.92
7	0.93	0.94	0.91
8	0.93	0.94	0.91
9	0.93	0.92	0.91
10	0.93	0.92	0.92
11	1.43	1.41	1.44
12	1.43	1.41	1.44
13	1.43	1.41	1.44
14	1.43	1.38	1.44
15	1.43	1.41	1.44
16	1.93	1.89	1.97
17	1.93	1.87	1.97
18	1.93	1.90	1.97
19	1.93	1.85	1.97
20	1.93	1.90	1.97
21	2.39	2.24	2.45
22	2.39	2.30	2.45
23	2.39	2.31	2.45
24	2.39	2.30	2.45
25	2.39	2.47	2.46
Average per reference			
1	0.00	0.00	0.00
2	0.47	0.48	0.43
3	0.93	0.93	0.91
4	1.43	1.40	1.44
5	1.93	1.88	1.97
6	2.39	2.32	2.45

Table C. 2 Comparison between on-off and continuous method (collection of bubbles)

Item	Jg reference (cm/s)	Jg on-off (cm/s)	Jg continuous (cm/s)
1	0.48	0.48	0.47
2	0.48	0.48	0.46
3	0.48	0.48	0.46
4	0.48	0.50	0.45
5	0.48	0.48	0.46
6	1.09	1.13	1.19
7	1.09	1.14	1.19
8	1.09	1.13	1.18
9	1.09	1.14	1.18
10	1.09	1.14	1.18
11	1.68	1.80	1.84
12	1.68	1.85	1.82
13	1.68	1.77	1.83
14	1.68	1.80	1.85
15	1.68	1.81	1.84
16	2.27	2.39	2.45
17	2.27	2.50	2.46
18	2.27	2.37	2.45
19	2.27	2.46	2.45
20	2.27	2.51	2.45
Average per reference			
1	0.48	0.48	0.46
2	1.09	1.13	1.18
3	1.68	1.80	1.84
5	2.27	2.45	2.45

Table C. 3 Comparison between on-off and continuous method performed at Troilus (Canada)

Item	Jg on-off (cm/s) Equation 3. 19	Jg on-off (cm/s) Equation 3. 36	Jg (cm/s) Continuous
1	1.52	1.73	1.73
2	1.47	1.67	1.73
3	1.35	1.53	1.75
4	1.55	1.75	1.74
5	1.50	1.70	1.69
6	1.50	1.71	1.72
7	1.45	1.65	1.74
8	1.46	1.66	1.73
9	1.48	1.68	1.67
10	1.59	1.80	1.70
11	1.49	1.70	1.71
12	1.43	1.62	1.69
13	1.54	1.76	1.67
14	1.30	1.48	1.67
15	1.42	1.62	1.70
16	1.53	1.74	1.70
17	1.62	1.78	1.73
18	1.54	1.69	1.72
19	1.48	1.63	1.74
20	1.32	1.45	1.70
21	1.58	1.73	1.71
22	1.33	1.46	1.67
23	1.36	1.50	1.69
24	1.43	1.57	1.70
25	1.54	1.70	1.71
26	1.47	1.62	1.69
27	1.47	1.61	1.72
Error % (on-off/continuous)	**16**	**4**	**NA**
Average (cm/s)	**1.47**	**1.65**	**1.71**
st.dev (cm/s)	**0.08**	**0.10**	**0.02**

Table C. 4 Comparison between on-off/continuous method performed at CODELCO, Salvador (Chile)

Item	Jg on-off (cm/s) Equation 3. 19	Jg on-off (cm/s) Equation 3. 36	Jg (cm/s) Continuous
1	1.15	1.38	1.47
2	1.12	1.35	1.47
3	1.08	1.30	1.48
4	1.05	1.26	1.45
5	1.17	1.41	1.49
6	1.05	1.26	1.49
Error % (on-off/continuous)	25.15	10.10	NA
Average (cm/s)	1.10	1.33	1.47
st.dev (cm/s)	0.05	0.06	0.01

Table C. 5 Gas velocity profiles obtained from laboratory tests

	Relative radial distance r / R				
Condition	-0.27 Jg (cm/s)	-0.45 Jg (cm/s)	0.69 Jg (cm/s)	0.62 Jg (cm/s)	0.80 Jg (cm/s)
718 RPM 13 m³/h	0.60	0.49	0.19	0.32	0.20
	0.67	0.51	0.18	0.33	0.22
	0.60	0.48	0.17	0.30	0.21
	0.64	0.47	0.18	0.31	0.20
	0.64	0.49	0.18	0.32	0.21
	0.65	0.49		0.28	
	0.62	0.46		0.30	
	0.65	0.49		0.30	
	0.67	0.45			
	0.65	0.49			
	0.62	0.48			
	0.64				
	0.62				
Average per location					
	0.64	0.48	0.18	0.31	0.21

	Relative radial distance r / R				
Condition	-0.27 Jg (cm/s)	-0.45 Jg (cm/s)	0.69 Jg (cm/s)	0.62 Jg (cm/s)	0.80 Jg (cm/s)
718 RPM 25 m³/h	1.17	0.34	0.15	0.25	0.13
	0.92	0.34	0.16	0.27	0.12
	0.92	0.36	0.15	0.25	0.13
	1.01	0.39	0.16	0.26	0.14
	1.04	0.34	0.15	0.25	0.12
	1.06	0.37		0.29	
	0.92	0.36		0.23	
	0.88	0.38		0.26	
	0.88	0.39		0.25	
	0.98	0.38		0.24	
	1.15	0.38			
	0.94	0.34			
	1.28	0.36			

Table C. 5…Continuation

	1.19				
	1.16				
	1.04				
	1.08				
	1.18				
	1.04				
	1.04				
	0.94				
	0.92				
	0.92				
Average per location					
	1.03	0.36	0.15	0.25	0.13

	Relative radial distance r / R				
	-0.27	-0.45	0.69	0.62	0.80
Condition	Jg (cm/s)	Jg (cm/s)	Jg (cm/s)	Jg (cm/s)	Jg (cm/s)
	0.51	0.43	0.49	0.49	0.52
	0.51	0.42	0.48	0.50	0.51
1786 RPM	0.51	0.43	0.49	0.49	0.51
13 m³/h	0.51	0.44	0.49	0.50	0.53
	0.51	0.42	0.48	0.50	0.53
Average per location					
	0.51	0.43	0.49	0.50	0.52

	Relative radial distance r / R				
	-0.27	-0.45	0.69	0.62	0.80
Condition	Jg (cm/s)	Jg (cm/s)	Jg (cm/s)	Jg (cm/s)	Jg (cm/s)
	0.96	0.85	0.99	1.01	1.05
	0.97	0.88	0.99	1.01	1.12
1786 RPM	0.94	0.91	1.02	0.99	1.09
25 m³/h	0.95	0.90	0.97	0.99	0.94
	0.95	0.94	1.01	1.06	1.08
Average per location					
	0.95	0.90	0.99	1.01	1.06

Table C. 6 Parameters of parabolic model from laboratory tests

Impeller speed = 718 RPM / Air flow rate = 13 m³/h				
x	y	x^2	x^4	x^2 y
-0.27	0.64	0.0753	0.0057	0.0478
-0.45	0.48	0.2037	0.0415	0.0980
-0.69	0.18	0.4765	0.2270	0.0865
0.62	0.31	0.3837	0.1473	0.1179
0.80	0.21	0.6343	0.4024	0.1324
0.0000	**1.8142**	**1.7735**	**0.8238**	**0.4827**

System of equations

$$-0.8238 \cdot \alpha + 1.7735 \cdot \beta = 0.4827$$
$$-1.7735 \cdot \alpha + 5 \cdot \beta = 1.8142$$

$$\alpha = 0.83$$
$$\beta = 0.66$$

Table C. 7 Parameters distribution from tests: Effect of frother concentration Salvador

Frother concentration: 0 ppm				
x	y	x^2	x^4	x^2 y
-0.59	1.38	0.3481	0.1212	0.4797
-0.67	1.25	0.4489	0.2015	0.5624
-0.89	0.92	0.7921	0.6274	0.7292
-2.1500	**3.5517**	**1.5891**	**0.9501**	**1.7714**

System of equations

$$-0.9501 \cdot \alpha + 1.5891 \cdot \beta = 1.7714$$
$$-1.5891 \cdot \alpha + 5 \cdot \beta = 3.5517$$

$$\alpha = 1.01$$
$$\beta = 1.72$$

Frother concentration: 12 ppm				
x	y	x^2	x^4	x^2 y
-0.59	1.96	0.3481	0.1212	0.6814
-0.67	1.74	0.4489	0.2015	0.7825
-0.89	1.71	0.7921	0.6274	1.3527
-2.1500	**5.4083**	**1.5891**	**0.9501**	**2.8166**

System of equations

$$-0.9501 \cdot \alpha + 1.5891 \cdot \beta = 2.8166$$
$$-1.5891 \cdot \alpha + 5 \cdot \beta = 5.4083$$

$$\alpha = 0.44$$
$$\beta = 2.03$$

Frother concentration: 20 ppm				
x	y	x^2	x^4	x^2 y
-0.59	1.42	0.3481	0.1212	0.4947
-0.67	1.45	0.4489	0.2015	0.6495
-0.89	1.26	0.7921	0.6274	0.9983
-2.1500	**4.1283**	**1.5891**	**0.9501**	**2.1425**

System of equations

$$-0.9501 \cdot \alpha + 1.5891 \cdot \beta = 2.1425$$
$$-1.5891 \cdot \alpha + 5 \cdot \beta = 4.1283$$

$$\alpha = 0.41$$
$$\beta = 1.59$$

Table C. 8 Effect of frother concentration Chuquicamata

Frother concentration: 14 ppm				
x	y	x^2	x^4	x^2 y
-0.88	0.94	0.7744	0.5997	0.7268
-0.69	1.00	0.4761	0.2267	0.4755
0.33	1.10	0.1089	0.0119	0.1200
0.77	0.99	0.5929	0.3515	0.5845
0.88	0.94	0.7744	0.5997	0.7255
0.4100	**4.9617**	**2.7267**	**1.7895**	**2.6322**

System of equations

$$-1.7895 \cdot \alpha + 2.7267 \cdot \beta = 2.6322$$
$$-2.7267 \cdot \alpha + 5 \cdot \beta = 4.9617$$

$$\alpha = 0.24$$
$$\beta = 1.12$$

Frother concentration: 16 ppm				
x	y	x^2	x^4	x^2 y
-0.88	0.97	0.7744	0.5997	0.7525
-0.69	1.03	0.4761	0.2267	0.4923
0.33	1.13	0.1089	0.0119	0.1235
0.77	1.05	0.5929	0.3515	0.6203
0.88	1.03	0.7744	0.5997	0.7980
0.4100	**5.2168**	**2.7267**	**1.7895**	**2.7866**

System of equations

$$-1.7895 \cdot \alpha + 2.7267 \cdot \beta = 2.7866$$
$$-2.7267 \cdot \alpha + 5 \cdot \beta = 5.2168$$

$$\alpha = 0.19$$
$$\beta = 1.15$$

Table C. 8…Continuation

Frother concentration: 19 ppm				
x	y	x^2	x^4	x^2 y
-0.88	0.94	0.7744	0.5997	0.7303
-0.69	1.00	0.4761	0.2267	0.4782
0.33	1.10	0.1089	0.0119	0.1195
0.77	1.02	0.5929	0.3515	0.6036
0.88	1.00	0.7744	0.5997	0.7758
0.4100	**5.0648**	**2.7267**	**1.7895**	**2.7074**

System of equations

$-1.7895 \cdot \alpha + 2.7267 \cdot \beta = 2.7074$

$-2.7267 \cdot \alpha + 5 \cdot \beta = 5.0648$

$\alpha = 0.18$

$\beta = 1.11$

Frother concentration: 25 ppm				
x	y	x^2	x^4	x^2 y
-0.88	0.90	0.7744	0.5997	0.6976
-0.69	0.97	0.4761	0.2267	0.4639
0.33	1.06	0.1089	0.0119	0.1155
0.77	0.97	0.5929	0.3515	0.5727
0.88	0.96	0.7744	0.5997	0.7459
0.4100	**4.8648**	**2.7267**	**1.7895**	**2.5955**

System of equations

$-1.7895 \cdot \alpha + 2.7267 \cdot \beta = 2.5955$

$-2.7267 \cdot \alpha + 5 \cdot \beta = 4.8648$

$\alpha = 0.19$

$\beta = 1.08$

Table C. 8 … Continuation

Frother concentration: 35 ppm				
x	y	x^2	x^4	x^2 y
-0.88	0.90	0.7744	0.5997	0.6982
-0.69	0.96	0.4761	0.2267	0.4574
0.33	1.04	0.1089	0.0119	0.1131
0.77	0.97	0.5929	0.3515	0.5730
0.88	0.97	0.7744	0.5997	0.7487
0.4100	**4.8337**	**2.7267**	**1.7895**	**2.5904**

System of equations

$$-1.7895 \cdot \alpha + 2.7267 \cdot \beta = 2.5904$$
$$-2.7267 \cdot \alpha + 5 \cdot \beta = 4.8337$$

$$\alpha = 0.15$$
$$\beta = 1.05$$

Table C. 9 Effect of air flow rate, Chuquicamata

Air flow rate: 10 m^3/h				
x	y	x^2	x^4	x^2 y
-0.88	0.61	0.7744	0.5997	0.4717
-0.69	0.59	0.4761	0.2267	0.2828
0.33	0.69	0.1089	0.0119	0.0750
0.77	0.62	0.5929	0.3515	0.3659
0.88	0.63	0.7744	0.5997	0.4868
0.4100	**3.1379**	**2.7267**	**1.7895**	**1.6823**

System of equations

$$-1.7895 \cdot \alpha + 2.7267 \cdot \beta = 1.6823$$
$$-2.7267 \cdot \alpha + 5 \cdot \beta = 3.1379$$

$$\alpha = 0.10$$
$$\beta = 0.68$$

Air flow rate: 20 m^3/h				
x	y	x^2	x^4	x^2 y
-0.88	0.94	0.7744	0.5997	0.7268
-0.69	1.00	0.4761	0.2267	0.4755
0.33	1.10	0.1089	0.0119	0.1200
0.77	0.99	0.5929	0.3515	0.5845
0.88	0.94	0.7744	0.5997	0.7255
0.4100	**4.9617**	**2.7267**	**1.7895**	**2.6322**

System of equations

$$-1.7895 \cdot \alpha + 2.7267 \cdot \beta = 2.6322$$
$$-2.7267 \cdot \alpha + 5 \cdot \beta = 4.9617$$

$$\alpha = 0.24$$
$$\beta = 1.12$$

Table C. 9 … Continuation

Air flow rate: 30 m^3/h				
x	y	x^2	x^4	x^2 y
-0.88	1.29	0.7744	0.5997	1.0011
-0.69	1.39	0.4761	0.2267	0.6631
0.33	1.53	0.1089	0.0119	0.1664
0.77	1.40	0.5929	0.3515	0.8304
0.88	1.36	0.7744	0.5997	1.0513
0.4100	**6.9719**	**2.7267**	**1.7895**	**3.7123**

System of equations

$$-1.7895 \cdot \alpha + 2.7267 \cdot \beta = 3.7123$$
$$-2.7267 \cdot \alpha + 5 \cdot \beta = 6.9719$$

$$\alpha = 0.30$$
$$\beta = 1.56$$

APPENDIX D: LEAST SQUARES METHOD

This appendix presents the theory of the least squared method used in this thesis to obtain the gas distribution model parameters. The objective of this method consists of adjusting the parameters of a model function so as to best fit a data set. According to the method of least squares, the best fitting curve has the property that,

$$\Pi = \sum_{1}^{n} \left[y_i - f(x_i) \right]^2 = \text{minimum} \tag{D. 1}$$

Where y_i and x_i are the dependent and independent variables, respectively; n is the number of observations. In the case of a parabolic curve, $f(x_i)$ has the form,

$$\Pi = \sum_{1}^{n} \left[y_i - (\beta - \alpha \cdot x_i^2) \right]^2 = \text{minimum} \tag{D. 2}$$

Where α and β are the model parameters. Calculation of the model parameters requires equaling to zero the partial derivative of Π with respect to α,

$$\frac{\partial \Pi}{\partial \alpha} = \Sigma \left\{ 2 \cdot \left[y_i - (\beta - \alpha \cdot x_i^2) \right] \cdot x^2 \right\} = 0 \tag{D. 3}$$

re-arranging gives,

$$\Sigma x_i^2 \, y_i = -\alpha \cdot \Sigma x_i^4 + \beta \cdot \Sigma x_i^2 \tag{D. 4}$$

and equaling to zero the partial derivative of Π with respect to β,

$$\frac{\partial \Pi}{\partial \beta} = \Sigma \left\{ 2 \cdot \left[y_i - (\beta - \alpha \cdot x) \right] \cdot -1 \right\} = 0 \tag{D. 5}$$

re-rranging gives,

$$\Sigma y_i = -\alpha \Sigma x^2 + n \cdot \beta \tag{D. 6}$$

The unknown coefficients α and β can hence be obtained by solving simultaneously Equation (D. 4) and Equation (D. 6).